Nuclear and Cytoskeletal Prestress Govern the Anisotropic Mechanical Properties of the Nucleus

Joan Karla Macadangdang

A thesis submitted to

The Faculty of Graduate and Postdoctoral Studies

in partial fulfillment of the

requirements for the degree of

Master of Science in Physics

Department of Physics

Faculty of Science

University of Ottawa

Table of Contents

List of Figures

Abbreviation Legend

AFM	atomic force microscope/microscopy
ATP	adenosine triphosphate
CSK	cytoskeleton
CW	continuous wave
CytD	cytochalasin D
CytD-Noco	cytochalasin D + nocodazole
DMEM	Dulbecco's Modified Eagle's Medium
DMSO	dimethyl sulfoxide
DNA	deoxyribonucleic acid
ECM	extracellular matrix
ER	endoplasmic reticulum
FA	focal adhesion
FRAP	fluorescence recovery after photobleaching
FBS	fetal bovine serum
GFP	green fluorescent protein
GTP	guanine triphosphate
IF	intermediate filament
INM	inner nuclear membrane
KASH	Klarsicht, ANC-1, Syne Homology
LINC	linkers of the nucleoskeleton to the cytoskeleton
LSCM	laser scanning confocal microscope/microscopy
µm	micrometer
µM	micromole/micromolar
MT	microtubule
mW	milliwatt
NA	numerical aperture
nm	nanometer
NPC	nuclear pore complex
NSK	nucleoskeleton
ONM	outer nuclear membrane
PBS	phosphate-buffer saline
PEEK	polyetheretherketone
PSF	point spread function
SEM	standard error of the mean
SUN	Sad1 and UNC-84
STED	stimulated emission depletion
STM	scanning tunneling microscope
TEM	transmission electron microscopy

Abstract

Physical forces in the cellular microenvironment play an important role in governing cell function. Forces transmitted through the cell cause distinct deformation of the nucleus, and possibly play a role in force-mediated gene expression. The work presented in this thesis drew upon innovative strategies employing simultaneous atomic force and laser-scanning confocal microscopy, as well as parallel optical stretching experiments, to gain unique insights into the response of eukaryotic cell nuclei to external force. Non-destructive approaches confirmed the existence of a clear anisotropy in nuclear mechanical properties, and showed that the nucleus' mechanical response to extracellular forces is differentially governed by both nuclear and cytoskeletal prestress: nuclear prestress regulates shape and anisotropic deformation, whereas cytoskeletal prestress modulates the magnitude and degree of deformation. Importantly, the anisotropic mechanical response was conserved among diverse differentiated cell types from multiple species, suggesting that nuclear mechanical anisotropy plays an important role in cell function.

Acknowledgments

It's hard to list and thank each and every person who contributed something to make this thesis come together. Writing it all up is one thing, but there's also everything that came before that – two and a half years (error bars not shown!) of experiments, processing, and analyses, of building (and breaking) and testing and coding. But I'm going to try anyway, because I couldn't have done this alone, and I would be remiss if I didn't give a shout out to the wonderful people who helped me along the way.

Truth be told, before I started at the University of Ottawa I did not have a very strong Biophysics background at all. I'd worked in a Photonics lab during the last two years of my undergraduate studies in Manila, and the lasers I was familiar with were the bright blue ones that you couldn't turn on without first spending three hours checking and realigning the 50-odd lenses and splitters on the table. I didn't know the first thing about cell culture and transfection; my last formal Biology class had been in high school, because when given the choice between a third-year free elective in Biology or Colonial Art, I inexplicably chose the latter. What I'm trying to say is, in light of all that, I am deeply grateful to have been given the opportunity to work in this fascinating field. To my supervisor, Dr. Andrew Pelling: I cannot thank you enough for taking a chance on me, for teaching me so much, and for letting me work with wonderful labmates. I've really learned a lot since the day I started working in your group, not all of which will be contained in this thesis. Thank you for all of it.

I also want to thank all the (amazing, terrific, spectacular) members of the Pelling Lab. Tina, thank you for showing me the ropes and commiserating with me during marking marathons and certain 22-hour homework problems. Zeinab, thank you for your help with a couple of difficult courses I've had to take (you know which ones) and for all the times you force-fed me with dates and cashews. Pam, our sushi runs will always be dear to my heart, as will that one time we both channeled our inner Whitney Houston while working. Nicky, thanks for being cool with it. Dom and Charles, thank you for all the nuggets of wisdom you provided, and no I don't just mean the technical advice. Sebastian (“I made it through the wilderness...”) and Corinne (“Shorty fire burnin' on the dance floor!”) – thanks for the laughs. Alex, thanks for being nice to me even while staining; I feel special. Dan, I believe in you like I believe in Sherlock. But above it all, thank you guys (and J,

Justin, and Louise as well) for being my labmates. Working with you all has been an absolute privilege.

Outside the lab, I would like to express my appreciation for the Physics department as a whole for providing an intellectually stimulating environment, and in general just being filled with brilliant and kind people. I would especially like to thank Dr. Harden and his student Mehran for helping me whenever I came to them struggling with a particularly abstract concept, even if they were clearly in the middle of something when I walked in. Eric and Jason, thank you for the assistance you provided with my microfluidic setup. Helene and Madeleine, you were always so sweet and accommodating every time I swung by – thank you kindly.

Last but not least, I especially want to thank my friends and family who have offered support, given much-needed encouragement, and all in all just kept me sane during the past couple of years. To my Mom and Dad and Jody, thank you for the long-distance phone calls (many of them at ungodly hours) and for always convincing me to keep strong and strive on. To my fellow choir members at the locale of Ottawa, thank you for all the times we sang together, cried together, and shuttled over to the nearest Tim Horton's for caffeine between performances together. Lynn, Carina, Anita – if I tried to list here all the reasons I'm thankful to have 'met' you, my thesis proper wouldn't start until maybe twenty more pages in.

Thank you all for everything, from the very bottom of my heart. They say everyone feels a little pang of *something* at the completion of a work, but I find it to my liking. Here's to those who helped make it happen.

Contribution Statement

Conception

Experimental ideas, methodologies and conception of the research plan were developed in collaboration with my supervisor, Dr. Andrew Pelling.

Experiments and Analysis

I performed all experiments and data analyses. The optical stretcher was built with guidance from Dr. Jochen Guck and his group at the Cavendish Laboratory in the University of Cambridge. I developed all macros and routines used to analyze image data and facilitate a user interface for the optical stretcher. Data interpretation and conclusions were developed through discussions with Dr. Andrew Pelling and Dr. James Harden.

Thesis

This thesis is my own work. I thank Dr. Andrew Pelling for providing editorial assistance.

Statement of Originality

This thesis describes work carried out in the Department of Physics at the University of Ottawa between 2009 and 2012. The material in Sections 4.2.1 and the entirety of Chapter 5 are the subject of a paper submitted for publication to Integrative Biology (Manuscript ID IB-ART-03-2012-020065: "*Nuclear and Cytoskeletal Prestress Govern the Anisotropic Mechanical Properties of the Nucleus*" by J.K.L. Macadangdang, J.L. Harden and A.E. Pelling; submitted 21 March 2012).

Except where acknowledged otherwise, the work presented in this thesis is my own. To the best of my knowledge, this thesis does not infringe upon anyone's copyright nor violate any proprietary rights, and any ideas, techniques, quotations, or other material from the work of other people included in my thesis are fully acknowledged in accordance with standard referencing practices.

"*In our every cell, furled at the nucleus, there is a ribbon two yards long and just ten atoms wide. Over a hundred million miles of DNA in very human individual, enough to wrap five million times around our world and make the Midgard serpent blush for shame, make even the Ourobouros worm swallow hard in disbelief.*"

- **Alan Moore, *Snakes and Ladders***

Chapter 1

Introduction

Overview

Sometime in 1682, the Royal Society of London received a curious letter from a cloth merchant in Delft, Holland. The letter contained, among other things, the following excerpt:

"*…I came to observe the blood of a cod and of a salmon, which I also found to consist of hardly anything but oval figures, and however closely I tried to observe these, I could not make out what parts these oval particles consisted, for it seemed to me that some of them enclosed in a small space a little round body or globule…*"

The letter was addressed to Robert Hooke, the leading authority on microscopy at the time (Jardine 2003). The aforementioned cloth merchant, Antonie van Leeuwenhoek, had been inspired by Hooke's work and was studying the composition of cells. His findings suggested that cells were not, in fact, empty as Hooke had previously predicted. It is widely believed that Leeuwenhoek's report of globules in the cell was in fact one of the first sightings of cell nuclei (Harris 2001). His letter, however, regrettably went unanswered, which left Leeuwenhoek's issue unresolved and any prospective advances in studying cell nuclei at the time nipped in the bud. It took another 150 years before Robert Brown, having observed opaque areas in the cells of orchid flowers, offered a detailed description and finally gave the nucleus its name.

Since then, we have come a long way from 'Leeuwenhoek's globules' in terms of our understanding of the nucleus. Over the past few decades, the cell nucleus has been described, dissected, and deconstructed in order to fully understand its inner workings, which I describe in Section 1.1. Scientists have been able to characterize sub-nuclear components, their structures and functions, how they interact within the nucleus and with other components of the cell (Newport & Forbes 1987; Lamond & Earnshaw 1998). More recently, however, ever-increasing importance has been placed on the mechanical and physical properties of the nucleus: protecting and sequestering the cell's genetic material, arguably its most important role, is an inherently mechanical function, with all processes within the nucleus mediated one way or another by structural, load-bearing components (Lammerding, Dahl et al. 2007). In fact, mechanical properties of the cell nucleus are now recognized as important biological indicators (Bissell, Weaver et al. 1999; Bonne, di Barletta et al. 1999; Eriksson, Brown et al. 2003; Rowat,

Lammerding et al. 2006), and also feature heavily in regulating force-induced changes in gene expression (Dahl, Ribeiro et al. 2008; Dahl and Kalinowski 2011). Forces imposed onto the cell surface, such as during flow, have been shown to result in the reorganization of nuclear structures away from the region of applied force (Maniotis, Chen et al. 1997). Forces can also come from within the cell, generated by the cytoskeleton (Engler, Sen et al. 2006; Pajerowski, Dahl et al. 2007), and result in nuclear remodelling. All of these observations lend themselves to the continuing motivation to explore mechanical properties of the nucleus. An in-depth discussion of the importance of studying nuclear mechanics, from its role in human disease to the mechanism of force transfer from the cell to the nucleus, is provided in Section 1.3.

With this motivation, in this thesis I will describe my research which employs laser-scanning confocal microscopy to study the mechanical response of the nucleus to an applied force with the atomic force microscope (AFM; both techniques discussed in Section 2.1). The integration of these two microscopy techniques, in addition to the use of DNA-labelling fluorescent dyes, allowed for direct visualization of the effects of applied force on the cell nucleus, over both long (minute) and short (millisecond) timescales. Considering that this response may depend on the cell's microenvironment, as well as the nature and magnitude of applied force, I also observed the response of the nucleus to pulling, non-contact forces two orders of magnitude smaller within a microfluidic optical stretcher (discussed in Section 2.2). These mechanical responses of the nucleus were quantified and explored in detail in Sections 4.1 and 4.2, where they were indeed found to be different from one another.

Another important aspect to take into account is that in its native state, the nucleus is not mechanically isolated from the rest of the cell; rather, it is intimately linked to the cell's cytoskeleton (CSK), which is described thoroughly in Section 1.2. Through the CSK, external forces can be transmitted to the nucleus. Consequently I employed specific drug treatments (outlined in Section 2.3) in order to disrupt one or more of the structural components of the CSK. How the nuclei of such cells responded to force under the AFM is discussed in Chapter 5. Furthermore, in Chapter 6 I discuss the mechanical behaviour of the nucleus under *cyclic* force application, showing that certain cytoskeletal drug treatments greatly affect this response to repeated, periodic force.

Lastly, throughout Chapters 4, 5 and 6 I will demonstrate that the nucleus exhibits *mechanical anisotropy*: it does not expand uniformly under applied force (static or cyclic) under the AFM, but rather displays a more pronounced expansion along its lateral axis. This response seems to be characteristic of nuclei *in vivo*, as isolated nuclei taken from cells of the same type have been observed to behave as axisymmetric, uniform materials under indentation (Vaziri, Lee et al. 2006). To the best of my knowledge, this is the first instance in which **(1)** nuclear expansion in an optical stretcher, **(2)** nuclear response to cyclic force application, and **(3)** mechanical anisotropy in nuclear expansion, as well as its dependence on the cytoskeleton, are investigated.

1.1 The Eukaryotic Cell Nucleus

The structural biology of the cell and its components has been well characterized in the past (Porter, Claude et al. 1945; Alberts, Johnson et al. 2002; Lodish, Berk et al. 2004). Universally accepted as the basic functional unit of life, cells can be classified into two types: prokaryotes, to which archaea and bacteria belong; and eukaryotes, of which plants, animals, and fungi are made. The major difference between the two types is that eukaryotes contain a well-defined nucleus, a membrane-bound compartment housing the cell's genetic material. For the remainder of this thesis, we shall concern ourselves only with eukaryotic cells, of which a schematic representation is provided in Figure 1.1.

Even among eukaryotes there is a wide variation of cell morphologies, depending largely on which function the cells perform, and on which organism they compose. Still, there are a number of structures common to all cells. One is the cell membrane, consisting of a phospholipid bilayer with embedded proteins, which separates the interior of the cell from the outside environment. In addition, all cells contain an elaborate protein 'scaffolding' called the cytoskeleton (to be explored further in Section 1.2) which provides the cell with shape and structure. Permeating the cytoskeleton is the cytosol, a mixture of ions and macromolecules dissolved in water that form the intercellular fluid. In addition, the cell interior also contains a variety of internal membrane-bound structures called organelles, which are specialized subunits within the cell that perform a variety of functions, from energy production (mitochondria) to protein synthesis (endoplasmic reticulum, ER) and sorting (Golgi apparatus).

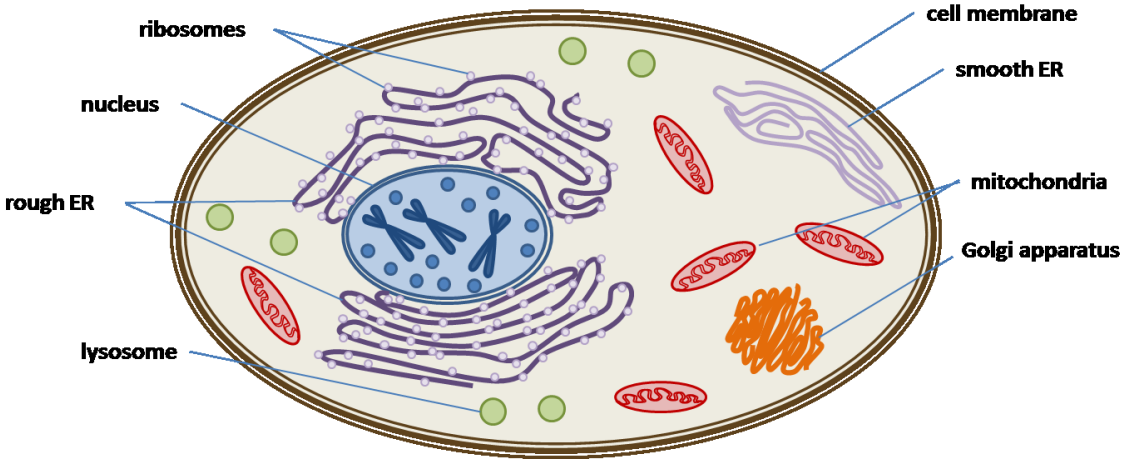

Figure 1.1: Schematic representation of a typical eukaryotic cell. The major components found in the eukaryotic cell are shown above. Mitochondria generate most of the cell's supply of adenosine triphosphate (ATP), which is used as its primary source of chemical energy (Henze & Martin 2003). The endoplasmic reticulum (ER) serves a number of general functions involving protein synthesis and transport, and is characterized by its lacey membrane structure (Porter, Claude et al. 1945). It can be classified as either smooth ER (Maxfield & Wüstner 2002) or rough ER, so named because of the protein-manufacturing ribosomes studded on its surface (Lodish, Berk et al. 2004). Materials synthesized by the cell are then processed by the Golgi apparatus, which is integral in modifying, sorting, and packaging said materials for use within the cell, or for secretion: in the latter case, lysosomes, also created by the Golgi apparatus, break down these waste materials and cellular debris (Alberts, Johnson et al. 2002). Lastly, the nucleus stores genetic information, enclosing DNA to separate it from cytoplasmic activities, and is the eukaryotic cell's defining organelle.

Among the largest and most ubiquitous of these organelles is the nucleus. It contains the cell's genetic material in the form of chromosomes, composed of multiple linear DNA molecules in complex with various proteins. Gene expression, the synthesis of proteins and functional RNA necessary for the cell's structure and survival, is regulated by the nucleus, hence why the nucleus is commonly perceived as the control center of the cell.

1.1.1 Nuclear Structure and the Nucleoskeleton

The nucleus is enclosed by the nuclear envelope, a structure composed of two lipid bilayers arranged parallel to one another. The envelope surrounds the nucleus completely and functions as a physical barrier in order to prevent macromolecules from diffusing freely between the nucleus and the rest of the cell. The outer membrane is contiguous with the endoplasmic reticulum and studded with ribosomes, which are organelles involved in protein

synthesis (Cooper & Hausman 2009). The region between the inner and outer membranes, roughly 10 to 50 nm in thickness, characterizes the perinuclear space (Paine, Moore et al. 1975; Spector 1993).

Crossing the nuclear envelope are large protein complexes called nuclear pores, shown in Figure 1.2. A typical eukaryotic cell nucleus will have 2,000 to 4,000 of these pores (Gerace & Burke 1988), although this number varies depending on cell type and stage in the life cycle. Nuclear pore complexes (NPCs) facilitate the transfer of water-soluble molecules to and from the nucleus, and are made up of proteins known as nucleoporins. Each NPC is composed of two coaxial rings, one facing the cytoplasm and one facing the nucleoplasm. Between these rings, eight radial spokes extend and contact a centrally located plug (Spector 1993). The eight peripheral channels allow the exchange of smaller particles through passive diffusion, while the central channel enables active transport required for the efficient transfer of larger molecules (Hinshaw, Carragher et al. 1992).

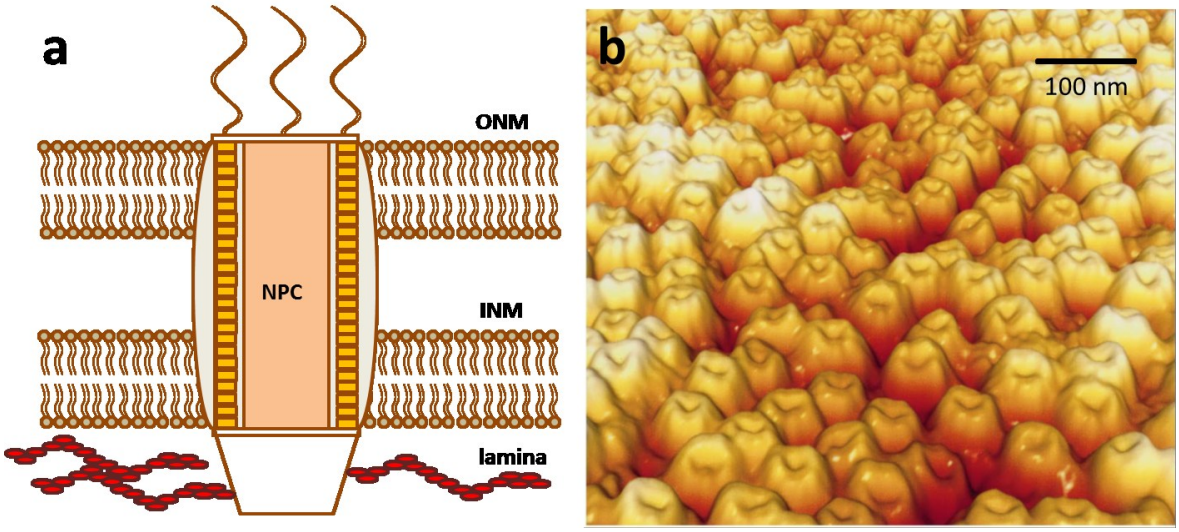

Figure 1.2. Nucleoskeletal structures. (a) A nuclear pore complex (NPC), characterized by filaments on the cytoplasmic side and a basket-like structure on the nucleoplasmic side, contacts both the inner nuclear membrane (INM) and outer nuclear membrane (ONM). (b) An AFM image taken of the surface of a *Xenopus laevis* oocyte nucleus shows the density of NPCs on the nuclear envelope (image reproduced, with permission, from Danker & Oberleithner 2000).

Anchoring the NPCs embedded in the nuclear envelope is a dense fibrillar network called the nuclear lamina (Fig. 1.2a). It is located internal and adjacent to the inner membrane of the nuclear envelope, measuring about 30 to 100 nm in thickness. The nuclear lamina is composed of membrane-associated proteins and nuclear lamins, fibrous proteins that comprise a class of intermediate filaments (IFs) exclusive to the cell nucleus. There are two main types of lamins: A-type lamins (primarily lamins A and C) and B-type lamins (B1 and B2) comprising the lamina, and they are generally present in equal amounts in the nucleus during interphase, the stage of the cell's life cycle prior to undergoing cell division (Gerace & Blobel 1980; Gruenbaum et al. 2005). While B-type lamins are essential to cell survival (Harborth, Elbashir et al. 2001; Tang et al. 2008) A-type lamins are thought to contribute more significantly to nuclear mechanics (Schape et al. 2005; Lammerding et al. 2006). Cells are able to survive without A-type lamins, but mutations in the gene encoding these lamins have been implicated in a significant number of human diseases, which will be explored in detail in Section 1.3.2.

The nuclear lamina is anchored to the inner nuclear membrane by an extensive array of membrane proteins such as LAP1/2 (lamina-associated polypeptides 1 and 2; Foisner & Gerace 2003), emerin (Bione et al. 1994), and MAN1 (Lin et al. 2000), which form the LEM-domain family of proteins (Wagner & Krohne 2007; Mejat & Misteli 2010). Other important proteins associated with the nuclear envelope, such as nesprins, can also be found on the outer nuclear membrane. Most notably, nesprin-2, which binds to the F-actin cytoskeleton, is an important scaffold protein that is involved with maintenance of the nuclear envelope architecture (Zhang, Skepper et al. 2001); various proteins that link the nuclear envelope to the CSK will be discussed more thoroughly in Section 1.1.3. Short actin structures have also been found at the nuclear envelope, but their small size relative to cytoskeletal F-actin makes it impossible for them to offer a similar degree of mechanical strength. Instead, it has been proposed that nuclear actin filaments provide 'struts' or binding sites for the stabilization of lamin filaments and other larger complexes (Dahl & Kalinowski 2011).

All together, these elements constitute the nucleoskeleton (NSK), a collective structure that is necessary for maintaining nuclear shape and structure. It prevents rupture of the nucleus under force and has also been suggested to assist in force transduction (Wang, Tytell et al. 2009). Although mainly tasked with providing mechanical support to the cell nucleus, it is also

involved in regulating DNA replication and cell division. To wit, the NSK provides the structural basis for intranuclear order (Philimonenko, Flechon et al. 2001), offering a mechanical framework for the various processes within the cell nucleus.

1.1.2 Chromatin Architecture

During most of the cell cycle, the cell's genetic material is organized within the interior of the nucleus in a DNA-protein complex known as chromatin. One of the primary functions of chromatin is to package DNA into smaller volumes. This is not a trivial task, considering that the total length of cellular DNA in animals can be up to a hundred thousand times the length of the cell itself (Adams, Celniker et al. 2000; Venter, Adams et al. 2001; Wurm, Wang et al. 2011). In this section we discuss the different levels of chromatin organization, and how chromatin structure changes throughout various stages of the cell cycle.

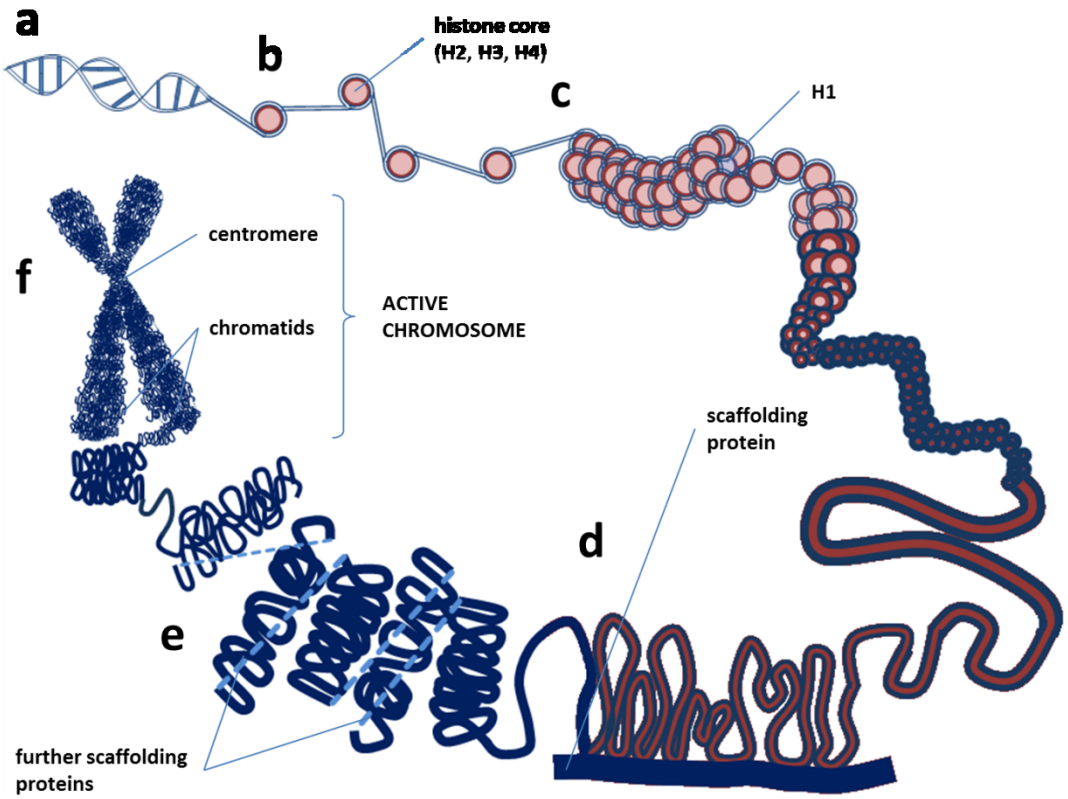

Figure 1.3. The various levels of chromatin architecture, at a glance. DNA (a) wraps around histone proteins (b) to form nucleosomes. These nucleosomes, resembling beads on a string, wind around the histone H1 to form 30-nm fibers (c), nucleosome arrays in their most compact form. Non-histone proteins provide scaffolds (d,e) to which these fibers attach, forming complexes that make up active chromosomes (f).

The most abundant proteins associated with DNA are called histones. These are small proteins present in all cell nuclei, of which there are five major types: H1, H2A, H2B, H3, and H4. All histones are rich in positively-charged, basic amino acids, which interact with the negatively-charged phosphate groups found in DNA. The fact that the amino acid sequences of most histones are remarkably similar among all eukaryotes seems to suggest that that they fold into very similar three-dimensional conformations, which were functionally optimized early in evolution (Lodish, Berk et al. 2004).

These histones are central to the primary step in DNA packaging which results in the basic unit of chromatin organization, called a nucleosome. Each nucleosome core particle is comprised of around 150 DNA base pairs wrapped slightly less than two turns around an octamer containing two copies each of the core histones H2A, H2B, H3 and H4 (Luger, Mäder et al. 1997). These core particles are then connected by stretches of free DNA called 'linker' DNA, which can range in length from around 10 to 80 base pairs long, depending on species and cell type (Felsenfeld & Groudine 2003).

Repeating nucleosomes with 'linker' DNA then form a linear structure descriptively called 'beads on a string' (Fig. 1.3b) enabling a packing ratio of around 5 to 10 (Chakravarthy, Park et al. 2005). These 'beads on a string' can be further packaged when nucleosomes associate with H1 histones, giving rise to a '30-nm fiber' (Fig. 1.3c) with a packing ratio of about 50. It has been suggested that the structure of the 30-nm fiber follows that of an irregular spiral or solenoid arrangement, with approximately six nucleosomes per turn, and H1 bound to the DNA on the inside of the spiral or solenoid (Lodish, Berk et al. 2004). Further organization of chromatin is required to achieve the degree of DNA compaction observed within the nucleus, however; it has been shown that non-histone proteins are also involved in chromatin organization by forming a scaffold, to which long loops of the 30-nm fiber are anchored (Fig. 1.3d; Paulson & Laemmli 1977).

It is important to remember that nuclear structure itself is dynamic, and as such the organization of chromatin actually depends on several factors. One of these is the stage of the life cycle (i.e. mitosis) in which the cell is currently found. The levels of organization discussed thus far are associated with the chromosome in its extended form as observed during

interphase; as previously mentioned, this is the stage of the cycle in which the cell spends the majority of its time prior to, and in preparation for, cell division. During metaphase, when the chromosomes align in the middle of the cell before being separated into the two daughter cells, chromatin is even more tightly compacted (Fig. 1.3e) to assume a more condensed, transportable form. In this form, most of the genetic material found in chromatin ceases to be accessible, and transcription stops. This structure is optimized for physical strength, which is necessary to prevent shear damage to the DNA as daughter chromosomes are separated. This is also the only form in which individual chromosomes are visible in their natural environment under an optical microscope, exhibiting the classic four-arm structure with two sister chromatids attached to one another at the centromere (Fig. 1.3f). It has been proposed that this highly-condensed structure of the metaphase chromosome is produced by further folding of the scaffold; however, the precise geometry of this folding has yet to be determined (Lodish, Berk et al. 2004).

Local chromatin structure during interphase is also affected by the genes present on the DNA strand. DNA coding genes that are actively transcribed are more loosely packaged, and found associated with RNA polymerases. These complexes are collectively referred to as euchromatin, with dynamic 30-nm fibers unfolding into the more open 'beads-on-a-string' structure when traversed by an RNA polymerase engaged in transcription. On the other hand, DNA coding inactive genes are more tightly packaged in regions collectively known as heterochromatin. Heterochromatin is a load-bearing structure within the nucleus, and mostly localized to the NSK at the nuclear envelope (Dahl & Kalinowski 2011). However, heterochromatic regions within the nuclear interior do exist, as do pockets of euchromatin at the nuclear envelope (Fedorova & Zink 2008), leading to regions of heterogeneous fluidity within an otherwise stiff nucleus. This only confirms that even in an isolated state, the cell nucleus is not a uniform mechanical structure.

1.1.3 Biochemical Links to the Cytoskeleton

But the nucleus is not, in fact, naturally isolated from the rest of the cell at all. There is a functional connection between the nucleoskeleton and the cytoskeleton, a structure that, analogous to the NSK, provides shape and support to the cell body. The CSK is highly dynamic and consists of three distinct elements: actin microfilaments, microtubules, and intermediate

filaments (to be further discussed in Section 1.2). Forces from the CSK are transferred across the nuclear envelope to the nuclear lamina, where they have been shown to affect chromatin structure, nuclear compartmentalization and other regulatory factors (Dahl, Engler et al. 2005; Starr & Fridolfsson 2010).

As mentioned in Section 1.1.1, the nuclear envelope is made up of two lipid bilayers, the inner and outer nuclear membranes, which are connected at the nuclear pores. The nuclear envelope is supported by lamins, membrane proteins, and chromatin-associated proteins (Gruenbaum et al. 2005) underlying the inner nuclear membrane (INM). In turn, the outer nuclear membrane (ONM) is continuous with the endoplasmic reticulum. However, since both of these membranes are fluid, any connections that serve to facilitate force transfer between the CSK and the nuclear interior must necessarily be physical, structural elements that bridge the nuclear envelope (Starr, 2005). The currently accepted model posits that elements of the CSK are linked to the NSK by a family of macromolecular assemblies that span the nuclear envelope, called LINC (linkers of the nucleoskeleton to the cytoskeleton) complexes (Crisp et al. 2005; Razafsky & Hodzic 2009; Mejat & Misteli 2010).

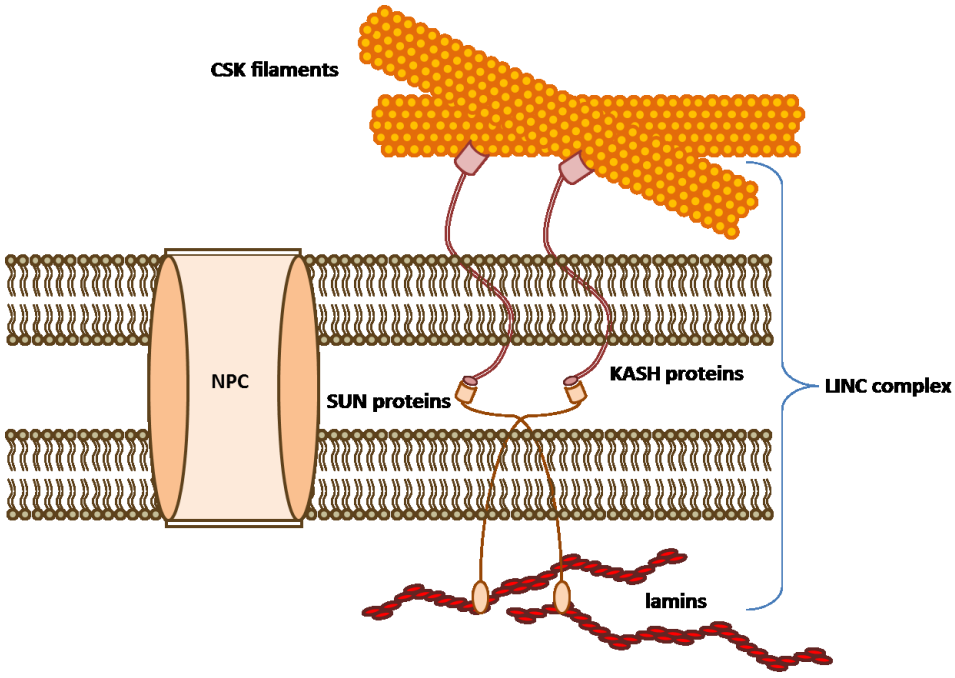

Figure 1.4 Representation of a typical LINC complex. SUN- and KASH-proteins, located at the INM and ONM respectively, interact in the perinuclear space, while simultaneously contacting either NSK or CSK-associated proteins.

A typical LINC complex is shown schematically (together with an NPC) in Figure 1.4. In general, a LINC complex consists of four main parts. At its core, a SUN- (Sad1 and UNC-84; Worman & Gunderson 2006) and KASH- (Klarsicht, ANC-1, Syne Homology; Starr & Fischer 2005) domain protein interact with one another in the perinuclear space between the INM and the ONM. On the nucleoplasmic side of the INM, the other end of the SUN protein interacts with either the lamina or any of several INM-associated proteins, such as the LEM-domain proteins (Wagner & Krohne 2007; Mejat & Misteli 2010). Conversely, the outer end of the KASH protein on the cytoplasmic side contacts an ONM protein that interacts with a component of the CSK, completing the bridge across the nuclear envelope (Razafsky & Hodzic 2009).

There is quite a large number of protein isoforms and variants of both INM and ONM components of LINC complexes across organisms, which seems to suggest that tissue- or developmentally-specific interactions can take place (Mejat & Misteli 2010). In mammals, for example, the ONM proteins are generally members of the nesprin family (Zhang, Skepper et al. 2001), with nesprin-1 and -2 binding to actin filaments. Nesprin-3 binds to plectin, a large protein that in turn binds to intermediate filaments (IFs). Lastly, nesprin-4 binds to kinesins, the motor proteins that 'walk' along microtubules (MTs; Wilhelmsen, Litjens et al. 2005; Roux, Crisp et al. 2009). LINC complexes connecting the actin and plectin-IF networks to the nucleus facilitate nuclear positioning and anchorage, whereas those contacting MTs facilitate nuclear migration and centrosome association (Mejat & Misteli 2010). Nonetheless, it has been shown that these connections are indeed mechanical in nature (Maniotis, Chen et al. 1997), and facilitate direct force transfer between the nucleus and the cytoskeleton.

1.2 Review of the Eukaryotic Cytoskeleton

Often likened to a ‘scaffold’ within the cell, the cytoskeleton (CSK) provides the cell with structure and support. It is not, however, a passive and rigid structure as the comparison would suggest, but rather highly dynamic. It is actively involved in many cellular processes, and constantly in a state of remodelling, usually on the order of seconds (Wu, Kuhn et al. 1998) in

response to both environmental cues and signals from within the cell and the external environment.

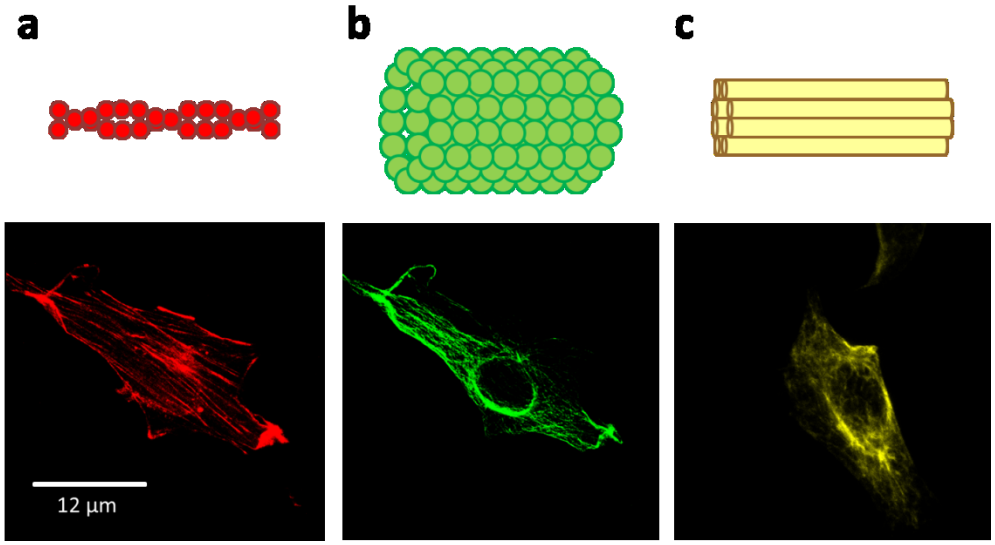

Figure 1.5 Individual components of the CSK. Visual representations of single (a) actin microfilaments, (b) microtubules, and (c) intermediate filaments are shown, with images showing their respective morphologies and distributions in cells presented below. Images in the bottom row were obtained using confocal microscopy (Section 2.1.2) performed on cells that were either transfected (Section 3.2) or stained (Section 3.3) for each particular component.

As shown in Figure 1.5, the CSK consists of three distinct classes of protein structures. Actin filaments, also called microfilaments, are the thinnest of these with an average diameter of 7 nm. Naturally a globular protein (G-actin), these individual subunits assemble into long filaments called F-actin. Two parallel F-actin strands layer on top of one another to form the double-helix structure of microfilaments in the CSK (Fig. 1.5a). When combined with crosslinking proteins and the motor protein myosin II (Vicente-Manzanares, Xuefei et al. 2009) microfilaments organize into stress fibers. Specifically, alternating bands of α-actinin (an actin-binding protein) and myosin II connect bundles of microfilaments together to form a stress fiber (Pellegrin & Mellor 2007); the myosin motors in the stress fiber can move ('walk' along the fiber), enabling the fiber to contract. In addition to providing mechanical support, the actin network is involved in cell motility, cell division, organelle movement, cell signalling, and maintaining cell shape. Many of these processes are mediated by extensive interactions of actin with cellular membranes (Doherty & McMahon 2008). In particular, actin filaments in

fibroblasts tend to align along the long axis of the cell, and so it has been proposed that any anisotropy in global cellular deformation is dominated by the actin fibers (Heggeness, Wang et al. 1977).

Microtubules (MTs), the largest of the CSK filaments at 25 nm in diameter, are made up of two types of proteins called α-tubulin and β-tubulin. These two subunits form heterodimers in complex with GTP (an energy molecule similar in function to ATP), which then polymerize end to end forming protofilaments. The protofilaments then bundle into hollow cylindrical filaments by arranging themselves in an imperfect helix, with each turn of the helix containing dimers from thirteen different protofilaments (Fig. 1.5b). MTs are also polar filaments: because tubulin polymerizes with the α subunit of one dimer contacting the β subunit of the next, one end of the microtubule will have all α subunits exposed, while the other will have all β subunits exposed. These ends are designated the (−) and (+) ends, respectively. Like microfilaments, MTs are also important for maintaining cell structure and imparting mechanical support. They also provide platforms for intracellular transport and are critically involved in cell division, where they form the mitotic spindle which separates the chromosomes during mitosis (Desai & Mitchison 1997).

Lastly, intermediate filaments (IFs) are named for their size: their average diameter of 10 nm lies between those of smaller actin microfilaments and larger MTs (Fig. 1.5c). They are considered highly deformable since they are able to undergo significant stress without breaking, as well as return to their original form upon stress removal. IFs can be categorized into six main types based on similarities in protein structure. Of these, only one (Type V – lamins, discussed in Section 1.1.1) can be found in the nucleus; the rest are generally cytoplasmic. In particular, vimentins (a subset of Type III IFs), the most widely distributed of all IF proteins, can be found in fibroblasts, supporting the cell membrane. Vimentins also serve to anchor organelles within the cytosol, attaching to the nucleus, ER, and mitochondria (Katsumoto, Mitshushima et al. 1990).

Although the CSK can be thought of as being composed of three distinct filament networks, it is also important to recognize the interconnections between each of these networks to each other, to the organelles, and to the external environment. Aside from the

LINC complexes discussed earlier, there also exist extensive actin-binding and microtubule-binding proteins, whose cross-linking significantly alters the composition of each individual network. MTs are often found in complex with kinesins and dyneins, transporter molecules which 'walk' along the microtubule and bring necessary materials to where they are needed within the cell. Similarly, actin is often found in complex with other proteins of the myosin family, with myosin V 'walking' along microfilaments in order to transport cargo molecules in a similar manner. Previous studies also seem to suggest intimate interactions between MTs and vimentins (Gyoeva & Gelfand, 1991; Maniotis, Chen et al. 1997). Results of a study involving transgenic mice that lacked vimentin but turned out to be functionally normal (Goldman, Khuon et al. 1996), seem to suggest that the MT network may compensate for the absence of the IF network. On the other hand, when MTs were depolymerized, vimentin reorganization occurred (Goldman, Khuon et al. 1996), a phenomenon that will be revisited in Chapter 4.

As mentioned earlier, the CSK is able to respond to stimuli from the cell's external environment. It does through its attachments to focal adhesion (FA) complexes, large macromolecular assemblies which form at the basal surface of the cell, at which the cell membrane closes to within 15 nm of the substrate (Zeidel-Bar, Cohen et al. 2004). FAs may be composed of up to 100 different proteins (Zamir & Geiger 2001), of which proteins called integrins (Hynes 1987) are key: these are the transmembrane proteins that connect the cellular interior with the extracellular matrix (ECM), a gel-like network of collagen and polysaccharides providing an external scaffolding to the cell. Integrins binds to proteins of the ECM via short amino acid sequences, while its intracellular domain binds directly to the actin network via adapter proteins such as talin (Burridge & Connell 1983), α-actinin (Reinhard, Zumbrunn et al. 1999), and vinculin (Ezzell, Goldmann et al. 1997). Links between integrins and microtubules have also been established, with focal adhesion kinase and lipid rafts mediating integrin signalling to MTs (Palazzo, Eng et al. 2004). Dynamitin, a component of the dynein motor complex that 'walks' along MTs, has also been found to localize at focal contacts (Garces, Clark et al. 1999).

Taking these connections between the CSK and the environment together with the nuclear-CSK links that were described in Section 1.1.3, we see that the nucleus is actually physically connected to the microenvironment of the cell. Indeed, 'harpooning' experiments

with micropipettes and intact endothelial cells (Maniotis, Chen et al. 1997) show that pulling on integrins on the cell surface resulted in reorientation of CSK filaments, distorted nuclei, and spatial redistribution of subnuclear structures. These results confirmed that molecular connections between integrins, CSK filaments, LINC complexes and NSK scaffolds could provide a discrete path for mechanical signal transfer.

1.3 Importance of Studying Nuclear Mechanics

The nucleus is generally the largest, stiffest organelle of a eukaryotic cell, and is literally its defining feature. Naturally, this means that the nucleus and nuclear structure have a great effect on the overall cellular mechanical properties (Lammerding, Dahl et al. 2007). However, they also play a critical role in many cellular functions, as nuclear organization directly affects accessibility of chromatin (discussed in Section 2.1.2) to transcriptional regulators. The transmission of mechanical forces to the interior of the nucleus, as well as the induced nuclear deformations, also depends on the mechanical properties of the nucleus (Dahl, Ribeiro et al. 2008).

It comes as no surprise, then, that nuclear mechanics have been the focus of rigorous study over the past few decades. Researchers have employed a variety of techniques to probe and understand nuclear mechanics, studying nuclear shape as well as the nucleus' response to applied stress and strain. While the wide variety of techniques has led to some disparity in values reported of mechanical properties such as nuclear stiffness (Dahl, Ribeiro et al. 2008), nevertheless these techniques have yielded important knowledge and shed light on several key aspects of nuclear mechanics. Studies on isolated nuclei (Caille, Thoumine et al. 2002; Dahl, Engler et al. 2005) have been used to clarify nuclear localization of proteins that are sometimes masked by strong cytoplasmic signals (Lammerding, Dahl et al. 2007). Micropipette aspiration, in which isolated nuclei are drawn up into the tube of a micropipette using a pressure differential, has been a key technique in measuring nuclear stress versus strain behavior; different nuclei exhibit both viscoelastic and plastic-like behavior, although this depends on phenotype as well as cell type. Micropipette aspiration has also enabled the observation of

lamina rearrangement, and characterization of the roles of subnuclear structures in nuclear mechanics (Dahl, Engler et al. 2005; Rowat, Foster et al. 2005). Micropipette aspiration works in the regime wherein the scale of deformation is on the order of the whole nucleus. At that particular scale, the nucleus can then be treated as a generally isotropic, homogenous material (Lammerding, Dahl et al. 2007).

But the exploration of nuclear mechanics is certainly not just limited to isolated nuclei. Studies have also been done in which cells were cultured on elastic membranes, and their nuclei strained as the substrate (and cells) were stretched (Barbee, Macarak et al. 1994; Caille, Tardy et al. 1998). This allows for comparison of effective nuclear strains to cytoskeletal strains, from which properties such as nuclear stiffness may be inferred. These substrate-strain studies and compression experiments (Guilak 1995; Thoumine, Ott et al. 1997; Caille, Thoumine et al. 2002) on whole cells were among the earliest attempts at studying the nucleus' response to external force, an approach also taken and appropriate to local forces applied with the AFM (Hategan, Law et al. 2003; Dahl, Engler et al. 2005; Lammerding, Dahl et al. 2007). The question of how force affects the nucleus is not a trivial one; the nucleus has been shown to adapt and reorder following an external applied force (Deguchi, Maeda et al. 2005), and extracellular forces and strain result in clearly detectable nuclear deformations (Guilak, Tedrow et al. 2000). In this section we discuss the main motivations for studying nuclear mechanics, particularly how the nucleus behaves in response to force.

1.3.1 Overview of Nuclear Mechanical Properties

Measurements made of nuclear stiffness span over two orders of magnitude, since they depend both on the cell type and the experimental method chosen to carry out the said measurements (Dahl, Ribeiro et al. 2008). These values range from 0.1 to 10 kPa, but the general consensus is that the nucleus of the cell is significantly stiffer than its surrounding cytoplasm (Caille, Thoumine et al. 2002; Kha, Chan et al. 2004; Guilak, Tedrow et al. 2000; Vaziri & Mofrad 2007). Still, extracellular forces and strain have been shown to bring about clearly detectable nuclear deformations (Guilak 1995; Maniotis, Chen et al. 1997) in addition to CSK and cell membrane reorganization.

As a mechanical system, the nucleus is typically modeled as a viscoelastic solid (Guilak, Tedrow et al. 2000; Rowat, Foster et al. 2005; Dahl & Kalinowski 2011). Viscoelastic materials are characterized by two kinds of mechanical response: an initial deformation, such as elastic stretch typically modeled by a spring, is combined with a fluid-like viscous flow which is modeled by a dashpot (Crawford 1998; Meyers & Chawla 1999). For elastic (spring) components, one can write the stress-strain relationship as:

$$\sigma_S = \xi \varepsilon_S \quad [1]$$

where σ is the stress, ξ is the elastic modulus of the material, and ε is the strain that occurs due to the applied stress. Similarly, for the viscous (dashpot) components, we can write:

$$\sigma_D = \eta \frac{d\varepsilon_D}{dt} \quad [2]$$

The subscripts *S* and *D* denote quantities corresponding to the spring and dashpot, respectively. Here, σ is still the stress applied, η is the material's viscosity, and dε/dt represents the time derivative of the resulting strain (Meyers & Chawla 1999).

Viscoelastic models (illustrated in Figure 1.6) are formed from linear combinations of these components, and are used to predict such a material's response under various mechanical loading conditions. The simplest of these, called the Maxwell model (Fig. 1.6c) consists of a spring and a dashpot connected to one another in series. Under such an arrangement, the applied stress σ is equal for both of the elements, whereas the total strain is the sum of the individual strains (Crawford 1998):

$$\sigma(\text{Maxwell}) = \sigma_S = \sigma_D \quad [3]$$

$$\varepsilon(\text{Maxwell}) = \varepsilon_S + \varepsilon_D \quad [4]$$

Combining equations 1, 2, 3, and 4, we arrive at the governing equation of the Maxwell model:

$$\frac{d\varepsilon}{dt} = \frac{1}{\xi}\left(\frac{d\sigma}{dt}\right) + \frac{\sigma}{\eta} \quad [5]$$

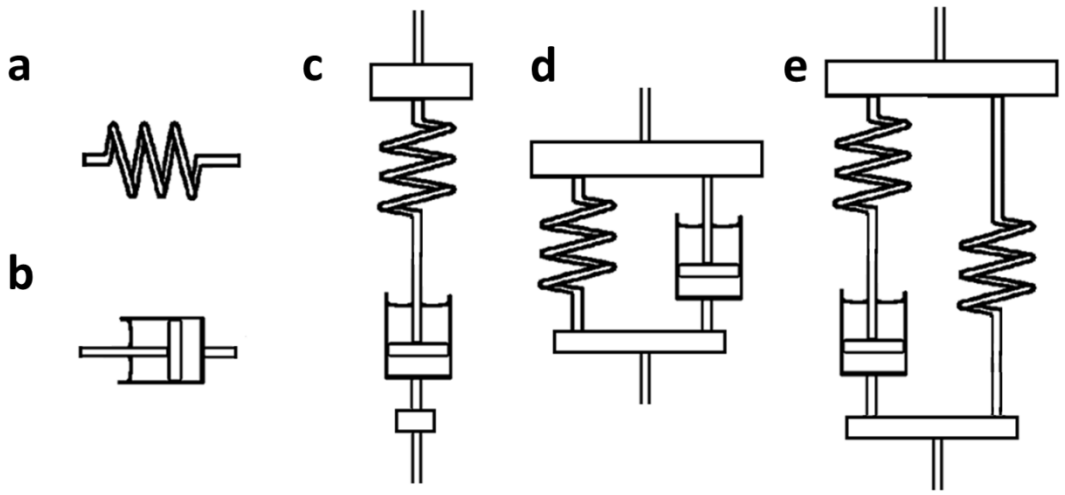

Figure 1.6 Common viscoelastic models. Elastic springs (a) and motion-damping dashpots (b) are combined in various ways to form the different viscoelastic models (c-e), which are in many ways analogous to electrical circuits. The Maxwell model (c) has a spring and dashpot connected in series. The Kelvin-Voigt model (d) has these two components in parallel. Finally, the Standard Linear model or Zener model (e) combines the Maxwell model and an additional spring in parallel, and is generally more accurate than either the Maxwell or Kelvin-Voigt model at predicting material responses.

If we assume that the applied stress σ is constant ($\sigma = \sigma_0$), then Equation 5 above can be solved to obtain an expression for the time-dependent strain ε(t):

$$\varepsilon(t) = \frac{\sigma_0}{\xi} + \frac{\sigma_0}{\eta} t \quad [6]$$

It can be seen from Equation 6 that when a Maxwell material is put under constant stress, the time-dependent strain has an instantaneous, elastic component (represented by the first term) that corresponds to the spring. The other component (represented by the second term) grows with time so long as the constant stress is maintained.

In addition, we can also solve for the creep compliance J(t), which is defined as the ratio of the time-dependent strain to the applied stress (Ting 1966; Tweedie & van Vliet 2006; Lakers 2009). Creep compliance of viscoelastic materials has come to be the established metric of rate at which the strain increases for a constant applied stress (Tweedie & van Vliet 2006). Based on the result of Equation 6, the creep compliance for a Maxwell material can then be written as:

$$J(t) = \frac{\varepsilon(t)}{\sigma_0} = \frac{\eta + \xi t}{\xi \eta} \quad [7]$$

Under a constant-stress condition outlined above, the Maxwell model predicts that strain will increase linearly with time. This can be seen from the form of Equation 6, as well as in Figure 1.7a. This does not prove to be a very accurate prediction, however, as most polymers exhibit a strain rate that is decreasing with time (McCrum, Buckley et al. 1997). A more accurate model for predicting constant-stress viscoelastic behavior is the Kelvin-Voigt model (Meyers & Chawla 1999). Using this model, the viscoelastic material is represented by a spring and a dashpot connected in parallel, shown in Figure 1.6d.

For the Kelvin-Voigt model, the total stresses and strains are now defined as follows (Crawford 1998):

$$\sigma(\text{Kelvin-Voigt}) = \sigma_S + \sigma_D \quad [8]$$

$$\varepsilon(\text{Kelvin-Voigt}) = \varepsilon_S = \varepsilon_D \quad [9]$$

The applied load is supported by both the spring and the dashpot, and thus the total stress is the sum of the two individual components. On the other hand, the total strain is equal to the strain in each of the elements. The governing equation for the Kelvin-Voigt model, obtained using the combined results of Equations 1, 2, 8, and 9, can be written as (Crawford 1998):

$$\sigma_0 = \xi \varepsilon + \eta \frac{d\varepsilon}{dt} \quad [10]$$

Equation 10 can then be solved for the total strain, ε(t):

$$\varepsilon(t) = \frac{\sigma_0}{\xi}\left[1 - e^{-\frac{\xi}{\eta}t}\right] \quad [11]$$

The creep compliance for a Kelvin-Voigt Material can also be obtained, leading to:

$$J(t) = \frac{\varepsilon(t)}{\sigma_0} = \frac{1}{\xi}\left[1 - e^{-\frac{\xi}{\eta}t}\right] \quad [12]$$

Under application of a constant stress, a Kelvin-Voigt material deforms at a decreasing rate, asymptotically approaching the steady-state strain. This type of behavior is illustrated in Figure 1.7b.

Both the Maxwell and the Kelvin-Voigt models have their respective limitations when it comes to predicting the behavior of viscoelastic materials. These predictions can be improved, to a certain extent, by considering more complex models composed of several springs and dashpots in parallel and/or series. For example, the Standard Linear Solid model, shown in Figure 1.6e, consists of the Maxwell model in parallel with a single spring. This model predicts that under constant stress conditions, the material instantaneously deforms to some (elastic) strain, after which it will continually deform and asymptotically approach a steady-state (viscous) strain (Crawford 1998, McCrum, Buckley et al. 1997). The behavior of the time-dependent strain function under constant stress for each of the three models is summarized in Figure 1.7.

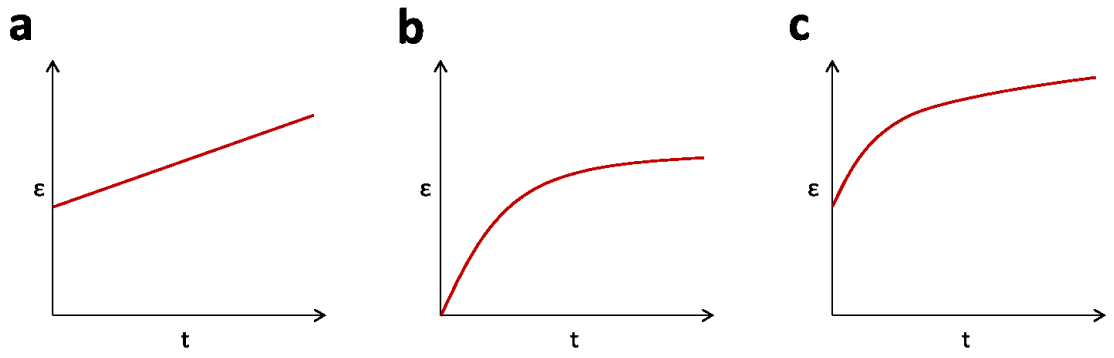

Figure 1.7 Constant-stress responses predicted by viscoelastic models. (a) After an instantaneous elastic strain, the Maxwell model predicts a linear increase of strain with time. (b) The Kelvin-Voigt model predicts an exponential increase in strain to a certain asymptotic value, corresponding to the value of ε that the material would have reached had the dashpot not been present. Lastly, the Standard Linear Solid model (c) predicts an instantaneous initial strain upon stress application, in addition to a subsequent, exponential increase in strain.

For isolated nuclei, the lamin meshwork supporting the nuclear membrane is treated as the elastic component, stretching under force, while the nuclear interior itself also deforms viscoelastically (Rowat, Foster et al. 2005; Pajerowski, Dahl et al. 2007). This suggests that the simplest approximation would require the Standard Linear model, shown in Figure 1.6e).

Previous measurements on chondrocyte nuclei, performed with micropipette aspiration, yielded elastic moduli on the order of 1-5 kPa, with data best fit by the Standard Linear model (Guilak, Tedrow et al. 2000). However, the presence of higher-order chromatin organization within the nucleus seems to suggest the existence of several time and length scales of deformation (Fabry, Maksym et al. 2001; Stamenovic 2008). Furthermore, mechanical responses have been found to be highly dependent on cell type, with some epithelial cells found to have a more complex rheology than these viscoelastic models could accurately predict. One such response (Dahl, Engler et al. 2005) is summarized in Figure 1.8 below.

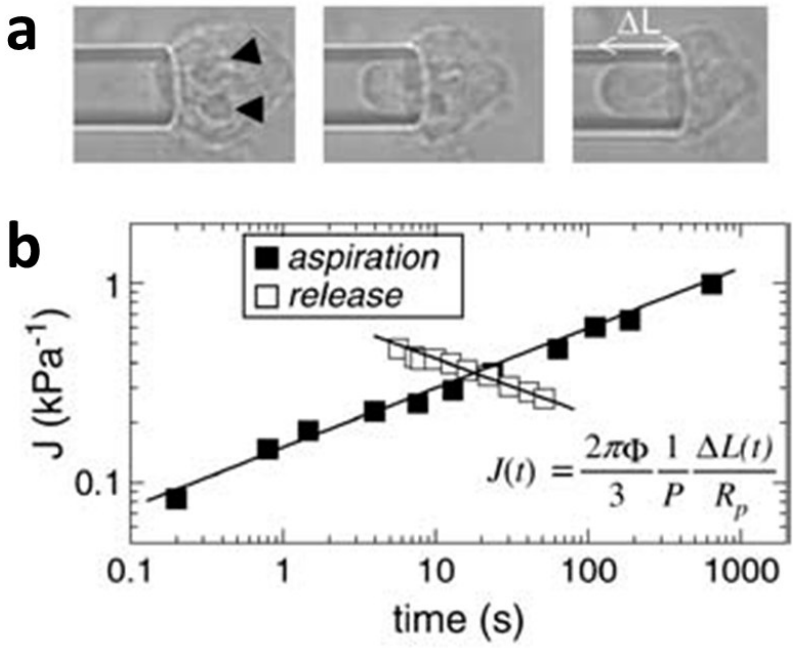

Figure 1.8. Results of micropipette aspiration experiments on TC7 (African green monkey kidney epithelium) cells. (a) A single, isolated nucleus is aspirated into a micropipette (inner diameter 6μm) at a constant applied pressure of 15 kPa. Deformation is observed both of the nucleus as a whole as well as of sub-nuclear structures (shown by the arrowheads). (b) The equation (inset) for creep compliance J(t) is expressed as a variation of the solution for aspiration of an infinite half-space (Theret, Levesque et al. 1988). J(t) is found to exhibit power-law behavior with an exponent $\alpha = 0.3$ over a timescale of 40 years; when the pressure is released, the projection length decreases with the same exponent (image reproduced, with permission, from Dahl, Engler et al. 2005).

Because of the surface roughness, the region of the nucleus outside of the micropipette could not be reliably measured by the 2D projection, and so it was treated as an infinite half-

space. Using this, Dahl et al. were able to define the creep compliance J(t) in terms of the parameters of the micropipette aspiration experiment:

$$J(t) = \frac{2\pi\Phi}{3P}\left(\frac{\Delta L(t)}{R_P}\right) \quad [13]$$

Here, P is the constant pressure applied, ΔL is the aspirated length normalized to the pipette before aspiration, R_P is the pipette radius, and Φ is a constant that depends on the micropipette thickness (Theret, Levesque et al. 1988). These micropipette aspiration experiments performed on nuclei isolated from monkey kidney epithelial cells resulted in a power-law behavior of the time-dependent creep compliance J(t). Variance in the observed behaviors of nuclei from different cell types is likely due to differences in the organization of nuclear structures, with mechanical properties being affected by factors such as lamin distribution at the nuclear envelope, or the level of chromatin organization (Dahl, Ribeiro et al. 2008).

1.3.2 Demonstrations of mechanical forces altering gene expression

It is known that forces exerted on the cell can alter gene expression indirectly through the activation of chemical cues, as in the phosphorylation of cellular signalling pathways (Chen, 2008). But since elements of the NSK serve as load-bearing structures in addition to influencing gene expression, it has been suggested that force may play a more direct role in gene regulation than was initially thought (Dahl & Kalinowski 2011).

On a single-molecule level, studies investigating the mechanics of purified DNA, chromatin, and chromosomes have shown that external force can induce remodelling and disassembly, which may be required for transcription (Zlatanova, Leuba et al. 2002; Marko, Poirier et al. 2003). Forces can also induce conformational changes within the nuclear interior, which in turn could alter the accessibility of chromatin and genes to transcription factors. In addition, force-induced changes in nuclear shape could also result in a large-scale reorganization of genes within the nucleus, although it is not yet clear exactly how these genes would be reordered, or how an external force would affect the localization of heterochromatin pockets (Dahl, Ribeiro et al. 2008).

Nevertheless, nuclear lamins have been shown to modulate chromatin organization (Stuurman, Heins et al. 1998), with B-type lamins in particular affecting chromosome positions

(Malhas, Lee et al. 2007). The fact that every important aspect of nuclear function is influenced by these nucleoskeletal proteins, which are also actively involved in nuclear mechanics and DNA processing, suggests that structural and biological roles are very likely integrated within the cell nucleus (Dahl & Kalinowski 2011).

1.3.3 Nuclear mechanics in disease

Mechanical properties of the nucleus are also intimately tied to a wide spectrum of human diseases. Mutations in nuclear lamins and associated nuclear envelope proteins have been discovered to cause pathophysiological changes that are associated with over 12 genetic disorders (Worman & Bonne 2007), collectively known as laminopathies. Most of the currently known laminopathies are summarized in Table 1.1 below.

Table 1.1: Laminopathies and Related Diseases

Structure Affected	Disease	Symptoms	References
Lamin A/C	Emery-Dreifuss muscular dystrophy *(autosomal)*	skeletal and cardiac muscular dystrophy	Bonne, di Barletta et al. 1999
	Limb-girdle muscular dystrophy	muscular dystrophy and cardiomyopathy	Muchir, Bonne et al. 2000
	Charcot-Marie-Tooth disease	neuropathy	De Sandre-Giovannoli, Chaouch et al. 2002
	Dilated cardiomyopathy	cardiomyopathy	Charniot, Pascal et al. 2003
	Werner syndrome *(atypical)*	progeria (premature aging)	Chen, Lee et al. 2003
	Hutchinson-Gilford progeria syndrome	progeria (premature aging)	Eriksson, Brown et al. 2003
Lamin B and Lamin B receptors	Pelger-Huet anomaly	myelodysplasia (defective neutrophils)	Hoffman, Dreger et al. 2002
	Greenberg dysplasia	skeletal dysplasia	Waterham, Koster et al. 2003
	Pelizaeus-Merzbacher disease *(adult-onset)*	leukodystrophy (abnormalities in white matter growth)	Padiath, Saigoh et al. 2006
	Barraquer-Simons syndrome	lipodystrophy (abnormalities in fat distribution)	Hegele, Cao et al. 2006

Lamin-binding proteins	Emery-Dreifuss muscular dystrophy *(X-linked)*	skeletal and cardiac muscular dystrophy	Manilal, Nguyen et al. 1996; Clements, Manilal et al. 2000
	Buschke-Ollendorff syndrome	skeletal dysplasia and skin lesions	Hellemans, Preobrazhenska et al. 2004

It was discovered that cells derived from laminopathy patients often have abnormally-shaped nuclei and changes in chromatin organization. For example, muscle cells from patients with Emery-Dreifuss muscular dystrophy have been shown to exhibit decreased nuclear stiffness, increased nuclear fragility, and increased sensitivity to mechanical strain (Broers, Bronnenberg et al. 2002; Lammerding, Schulz et al. 2004). On the other hand, cells from patients with Hutchinson-Gilford progeria syndrome, which is typified by increased lamin A at the nuclear envelope (Scaffidi & Misteli 2006) exhibited stiffer nuclei (Dahl, Scaffidi et al. 2006).

There are currently two propositions that have been offered to explain some of the pathologies associated with laminopathies (Dahl, Ribeiro et al. 2008). One of these is called the 'structural hypothesis,' which suggests that functional loss of A-type lamins could increase nuclear fragility, which in turn causes an increase in cell death in mechanically stressed tissue (such as muscle). The other proposition, known as the 'gene regulation hypothesis,' posits that the diseases are caused by altered interactions of transcriptional regulators, which lead to DNA damage and altered chromatin organization that in turn cause the genetic changes. Interestingly enough, these two hypotheses are not necessarily mutually exclusive; it has been suggested that they might, in fact, be interrelated (Dahl, Ribeiro et al. 2008), through nuclear mechanotransduction.

1.3.4 Force transmission and nuclear-CSK connectivity

The nucleus is not isolated from the mechanical environment of the rest of the cell. Extracellular forces can be transmitted across the CSK to the nucleus, resulting in intranuclear deformations (Pajerowski, Dahl et al. 2007). But while it has been acknowledged that the organization of the CSK is crucial in the ability of cell nuclei to sense and respond to external mechanical stresses, the question of how it does so largely remains open. Previous studies point

to an actomyosin filament sliding mechanism (Sims, Karp et al. 1992) instrumental in generating tension within the cell, which in turn drives CSK re-organization and leads to nuclear rounding. Others have stressed the importance of microtubules, citing their role in causing mechanical tension to instigate nuclear envelope breakdown (Beaudouin, Gerlich et al. 2002). Still others model the cell as a structure exhibiting tensegrity architecture. Here, actin filaments and MTs together provide a framework resisting tension and compression, mechanically coupled to a pre-stressed nucleus that itself also acts as a tensegrity structure (Ingber 2003a,b).

Despite the uncertainty with regards to its exact role, it is clear that considering the connections between the CSK and the nucleus is crucial to studying nuclear mechanics. Compression experiments on mouse embryonic fibroblasts using LSCM integrated with a single-cell loading device similar in principle to the AFM (Peeters, Bouten et al. 2003) have shown that the loss of physical interactions between nuclear structures and the CSK (i.e. in lamin A/C knockouts) led to significant loss of nuclear stiffness (Broers, Peeters et al. 2004). But the question of how exactly each of the CSK's components affects the nucleus' mechanical properties, particularly its behavior in response to external force, is more difficult and largely remains open. For these reasons, I chose to explore the mechanical response of the cell nucleus to nanonewton- and non-contact piconewton-scale forces with an atomic force microscope (AFM) and an optical stretcher, respectively. Tracking the response with simultaneous fluorescence microscopy enabled direct visualization of the nucleus throughout force application, and the use of anti-cytoskeletal drugs shed light into how this response is affected by the CSK and its components.

1.4 Methods and Scope of the Study

A descendant of the scanning tunnelling microscope (Binnig 1982), the atomic force microscope (AFM) was invented in the late 1980s, primarily for its use in measuring topography of non-conducting and semi-conducting surfaces at atomic resolution (Binnig, Quate et al. 1986). But it was its ability to apply a controlled, precise force onto an extremely specific location that made the AFM a valuable tool in cell biology and biophysics (Radmacher, Tillamnn

et al. 1992). Indeed, since its adoption into biomedical research the AFM has been successfully used to confirm previous cellular rheological measurements (Henderson, Haydon et al. 1992), quantify forces involved in protein interactions (Florin, Moy et al. 1994; Lee, Kidwell et al. 1994; Lehenkari & Horton 1999) and measure mechanical properties such as cellular stiffness, plasticity and viscoelasticity (Radmacher, Fritz et al. 1996; Haupt, Pelling et al. 2006). A key advancement in the use of AFM in biological studies was its subsequent integration with optical microscopes (Charras, Lehenkari et al. 2001; Haupt, Pelling et al. 2006). In particular, the popularization of fluorescent tags and dyes in the late 1990s allowed researchers to directly visualize the effects of applied force on the inner structures of the cell (Heidemann, Kaech et al. 1999). Simultaneously employing AFM with fluorescence and laser scanning confocal microscopy (LSCM) has further enabled direct correlation of mechanical properties measured with the AFM to specific cellular structures and dynamics (Silberberg, Pelling et al. 2008; Pelling, Veraitch et al. 2009).

It is important to note, though, that taking the specifics of the experiment performed is critical to properly interpreting the results obtained. The nature of cellular and cytoskeletal response to force depends on factors such as cell type, the stage of the cell in its life cycle, and the time scale of the measurement. But it is also important to consider the conditions in which the cells are being studied: in particular, even with all other factors held constant, the internal structure of an adherent cell is greatly different from that of a detached, suspended one, which suggests that the structural response to applied force may not necessarily be the same as well (Lodish, Berk et al. 2004; Ananthakrishnan, Guck et al. 2005; Guck, Schinkinger et al. 2005). An innovative tool recently developed to micromanipulate such non-adherent cells is the optical stretcher (Guck, Ananthakrishnan et al. 2001; Guck, Ananthakrishnan et al. 2002; Schinkinger, Wottawah et al. 2004; Ananthakrishnan, Guck et al. 2005; Guck, Schinkinger et al. 2005). Based on a double-beam laser trap (Constable, Kim et al. 1993), the device is composed of two identical, counter-propagating and slightly divergent laser beams trapping a cell suspended within a flow chamber in between them. Due to the symmetry of the trap, the total force acting on the cell is zero, but the surface forces are additive and stretch the cell along the beam axis (Guck, Ananthakrishnan et al. 2001). The device can be mounted onto a microscope stage, enabling real-time observation of optical deformation. Despite the fact that the optical

stretcher operates within a range of force two orders of magnitude lower than that of the AFM (Neuman & Nagy 2008), it has successfully been used to deform eukaryotic cells, and tracking optical deformation has yielded well-defined differences in the elastic response of cells across various cell types and pathologies (Guck, Ananthakrishnan et al. 2001; Guck, Schinkinger et al. 2005).

Studies on whole-cell mechanics using these and a variety of other experimental devices are extensive and well-documented (Pelling & Horton 2008). The effects of physical forces on isolated cell nuclei have also been rigorously studied (Guilak, Tedrow et al. 2000; Lammerding, Schulz et al. 2004; Dahl, Engler et al. 2005; Rowat, Foster et al. 2005) and modeled (Vaziri, Lee et al. 2006; Pajerowski, Dahl et al. 2007). However, as mentioned earlier, the precise effect the CSK has on the mechanical properties of the nucleus, particularly its response to applied force, is much less clear. In this thesis, I demonstrate force-induced nuclear deformation in cells which had specific components of the CSK targeted and disrupted with anti-cytoskeletal drugs. For each drug treatment I considered not only the particular component disturbed, but also how this affected the remaining components, and how these together affected the nucleus' response to force. Simultaneous imaging of the cell with LSCM while an AFM was used to apply a force directly over the nucleus allowed us to understand how an external force could bring about mechanical deformation in cell nuclei.

Importantly, it was observed that the nucleus does not expand uniformly under an applied force, but rather displays a mechanical anisotropy that is present regardless of the time scale in which the deformation is being observed. Results of anti-cytoskeletal drug treatments also showed that nuclear deformation is intimately affected by each of these elements, affirming that the CSK plays a role in force transmission to the nucleus. In addition, cells of the same type suspended in a microfluidic optical stretcher, in which the morphology of the CSK is drastically different from that of adherent cells, do not exhibit any significant deformation as a response to applied force. These results suggest that force transmission to the nucleus is not dependent only on the mechanics of the nucleoskeleton and chromatin structures, but also on the state of the cell's microenvironment and the structure of its CSK as well. These results also have several important implications in understanding gene regulation: since the mechanical and biological functions of the nucleus' structural components are so intimately coupled, it is crucial

to recognize that the mechanical properties of the nucleus directly impact cell biology, as we will see in Section 2.4. It is reasonable to propose that the way the nucleus deforms – particularly, the mechanical anisotropy it displays in its expansion under applied force – may play a role in gene regulation, especially when induced by mechanical stimuli.

1.5 References

Adams, M.D., Celniker, S.E. et al. (2000). "The genome sequence of *Drosophila melanogaster*." Science **287**(5461): 2185-2195.

Alberts, B., A. Johnson, J. Lewis, M. Raff, K. Roberts, P. Walter (2002). Molecular Biology of the Cell. New York, Garland Science.

Ananthakrishnan, R., J. Guck et al. (2005). "Modelling the structural response of an eukaryotic cell in the optical stretcher." Current Science **88**(9): 1434-1440.

Barbee, K.A., E.J. Macarak et al. (1994). "Strain measurements in cultured vascular smooth muscle cells subjected to mechanical deformation." Ann Biomed Eng **22**(1): 14-22.

Beaudouin, J., D, Gerlich et al. (2002). "Nuclear envelope breakdown proceeds by microtubule-induced tearing of the lamina." Cell **108**: 83-96.

Binnig, G., H. Rohrer et al. (1982). "Surface Studies by Scanning Tunneling Microscopy." Phys Rev Lett **49**(1): 57-61.

Binnig, G., C. F. Quate et al. (1986). "Atomic force microscope." Phys Rev Lett **56**(9): 930-933.

Bione, S., E. Maestrini at al (1994). "Identification of a novel X-linked gene responsible for Emery-Dreifuss muscular dystrophy." Nat Genet **8**:323-327.

Bissell, M.J., V.M. Weaver, et al. (1999). "Tissue structure, nuclear organization, and gene expression in normal and malignant breast." Cancer Res **59**: 1757s-1764s.

Bonne, G., M.R. di Barletta et al. (1999). "Mutations in the gene encoding lamin A/C cause autosomal dominant Emery–Dreifuss muscular dystrophy." Nature Genet **21**(3): 285-288.

Broers, J.L.V., E.A.G. Peeters et al. (2004). "Decreased mechanical stiffness in LMNA-/- cells is caused by defective nucleo-cytoskeletal integrity: implications for the development of laminopathies." Hum Mol Gen **13**(21): 2567-2580.

Burridge, K and L. Connell (1983). "A new protein of adhesion plaques and ruffling membranes." J Cell Biol **97**(2): 359-367.

Caille, N., Y. Tardy et al. (1998). "Assessment of strain field in endothelial cells subjected to uniaxial deformation of their substrate." Ann Biomed Eng **26**(3): 409-416.

Caille, N., O. Thoumine et al. (2002). "Contribution of the nucleus to the mechanical properties of endothelial cells." J Biomech **35**(2): 177-187.

Chakravarthy, S., Y.J. Park et al. (2005). "Structure and dynamic properties of nucleosome core particles". FEBS Lett. **579**(4): 895–898.

Charniot, J.C., C. Pascal et al. (2003). "Functional consequences of an LMNA mutation associated with a new cardiac and non-cardiac phenotype." Hum Mutat **21**(5):473-481.

Charras, G. T., P. P. Lehenkari, et al. (2001). "Atomic force microscopy can be used to mechanically stimulate osteoblasts and evaluate cellular strain distributions." Ultramicroscopy **86**: 85-95.

Chen, L., L. Lee et al. (2003). "LMNA mutations in atypical Werner's syndrome." Lancet **362**(9382): 440-445.

Clements, L., S. Manilal et al. (2000). "Direct interaction between emerin and lamin A." Biochem Biophys Res Commun **267**(3): 709-714.

Constable, A., J. Kim et al. (1993). "Demonstration of a fiber-optical light-force trap." Opt Lett **18**: 1867-1869.

Cooper, G.M. and R.E. Hausman (2009). The Cell: A Molecular Approach. Boston, Sinauer Associates Inc.

Crawford, R.J. (1998). Plastics Engineering. Butterworth-Heinemann, 87-89.

Crisp, M., Q. Liu et al. (2005). "Coupling of the nucleus and cytoplasm: role of the LINC complex." J Cell Biol **172**(1): 41-53.

Dahl, K.N., A. Engler et al. (2005). "Power law rheology of isolated nuclei with deformation mapping of nuclear sub-structures." Biophys J **89**: 2855-2864.

Dahl, K.N. and A. Kalinowski (2011). "Nucleoskeleton mechanics at a glance." J Cell Sci **124**: 675-678.

Dahl, K.N., A.J.S. Ribeiro et al. (2008). "Nuclear Shape, Mechanics, and Mechanotransduction." Circ Res **102**: 1307-1318.

Danker, T. and H. Oberleithner (2000). "Nuclear pore function viewed with atomic force microscopy." Pflügers Arch - Eur J Physiol **439**: 671-681.

De Sandre-Giovannoli, A., M. Chaouch et al. (2002). "Homozygous defects in LMNA, encoding lamin A/C nuclear-envelope proteins, cause autosomal recessive axonal neuropathy in human (Charcot-Marie-Tooth disorder type 2) and mouse." Am J Hum Genet **70**(3): 726-736.

Deguchi, S., K. Maeda et al. (2005). "Flow-induced hardening of endothelial nucleus as an intracellular stress-bearing organelle." J Biomech **38**: 1751-1759.

Desai, A. and T.J. Mitchison (1997). "Microtubule polymerization dynamics." Annu Rev Cell Dev Biol **13**: 83-117.

Doherty, G.J. and H.T. McMahon (2008). "Mediation, Modulation and Consequences of Membrane-Cytoskeleton Interactions." Ann Rev Biophys **37**: 65-95.

Engler, A.J., S. Sen et al. (2006). "Matrix elasticity directs stem cell lineage specification." Cell **126**: 677-689.

Eriksson, M., W.T. Brown et al. (2003). "Recurrent de novo point mutations in lamin A cause Hutchinson-Gilford progeria syndrome." Nature **423**: 293-298.

Ezzell, R.M., W.H. Goldmann et al. (1997). "Vinclin promotes cell spreading by mechanically coupling integrins to the cytoskeleton." Exp Cell Res **231**(1): 14-26.

Fabry, B., G.N. Maksym et al. (2001). "Scaling the microrheology of living cells." Phys Rev Lett **87**: 148102.

Fedorova, E. and D. Zink (2008). "Nuclear architecture and gene regulation." Biochim Biophys Acta **1783**: 2174-2184.

Felsenfeld, G. and M. Groudine (2003). "Controlling the double helix". Nature **421**(6921): 448–453.

Florin, E.L., V.T. Moy et al. (1994). "Adhesion forces between individual ligand-receptor pairs." Science **264**(5157):415-417.

Foisner, R., and L. Gerace (1993). "Integral membrane proteins of the nuclear envelope interact with lamins and chromosomes, and binding is modulated by mitotic phosphorylation." Cell **73**:1267-1279.

Garces, J.A., I.B. Clark et al. (1999). "Interaction of the p62 subunit of dynactin with Arp1 and the cortical actin cytoskeleton." Curr Biol **9**: 1497-1502.

Gerace, L. and G. Blobel (1980). "The nuclear envelope lamina is reversibly depolymerized during mitosis." Cell **19**: 277-288.

Gerace, L. and B. Burke (1988). "Functional organization of the nuclear envelope. " Annu. Rev. Cell BioI. **4**: 335-374.

Goldman, R.D., S. Khuon et al. (1996). "The function of intermediate filaments in cell shape and cytoskeletal integrity." J Cell Biol **134**(4): 971–983.

Gruenbaum, Y., A. Margalit et al. (2005). The nuclear lamina comes of age. Nat Rev Mol Cell Biol **6**: 21-31.

Guck, J., R. Ananthakrishnan et al. (2001). "The Optical Stretcher: A Novel Laser Tool to Micromanipulate Cells." Biophys J **81**:767-784.

Guck, J., R. Ananthakrishnan et al. (2002). "Stretching biological cells with light." J Phys Condens Matter **14**: 4843-4856.

Guck, J. S. Schinkinger et al. (2005). "Optical Deformability as an Inherent Cell Marker for Testing Malignant Transformation and Metastatic Competence." Biophys J **88**:3689-3698.

Guilak, F. (1995). "Compression-induced changes in the shape and volume of the chondrocyte nucleus." J Biomech **28**(12): 1529-1541.

Guilak, F., J.R. Tedrow et al. (2000). "Viscoelastic Properties of the Cell Nucleus." Biochem Biophys Res Commun **269**(3), 781-786.

Gyoeva, F.K. and V.I. Gelfand (1991). "Coalignment of vimentin intermediate filaments with microtubules depends on kinesin." Nature **353**: 445-448.

Harborth, J., S.M. Elbashir et al. (2001). "Identification of essential genes in cultured mammalian cells using small interfering RNAs." J Cell Sci **114**: 4557-4565.

Harris, H. (2001). The Birth of the Cell. Connecticut and London: Yale University Press.

Hategan, A., R. Law et al. (2003). "Adhesively-tensed cell membranes: Lysis kinetics and atomic force microscopy probing." Biophys J **85**(4): 2746-2759.

Haupt, B. J., A. E. Pelling, et al. (2006). "Integrated confocal and scanning probe microscopy for biomedical research." ScientificWorldJournal **6**: 1609-18.

Hegele, R.A., H. Cao et al. (2006). "Sequencing of the reannotated LMNB2 gene reveals novel mutations in patients with acquired partial lipodystrophy." Am J Hum Genet **79**(2): 383-389.

Heggeness, M. H., K. Wang et al. (1977). "Intracellular distributions of mechanochemical proteins in cultured fibroblasts." Proc Natl Acad Sci USA **74**(9): 3883-3887.

Heidemann, S. R., S. Kaech, et al. (1999). "Direct observations of the mechanical behaviors of the cytoskeleton in living fibroblasts." J Cell Biol **145**(1): 109-122.

Hellemans, J., O. Preobrazhenska et al. (2004). "Loss-of-function mutations in LEMD3 result in osteopoikilosis, Buschke-Ollendorff syndrome and melorheostosis." Nature Genet **36**(11): 1213-1218.

Henze, K. and W. Martin (2003). "Evolutionary biology: Essence of mitochondria." Nature **426**(6963): 127-128.

Hinshaw, J.E., B.O. Carragher, et al. (1992). "Architecture and design of the nuclear pore complex." Cell **69**: 1133-1141.

Hoffmann, K., C.K. Dreger et al. (2002). "Mutations in the gene encoding the lamin B receptor produce an altered nuclear morphology in granulocytes (Pelger-Huet anomaly)." Nature Genet **31**(4): 410-414.

Hynes, R.O. (1987). "Integrins: a family of cell surface receptors." Cell **48**(4): 549-554.

Ingber, D.E. (2003). "Tensegrity I. Cell structure and hierarchical systems biology." J Cell Sci **116**(7): 1157-1173.

Ingber, D.E. (2003). "Tensegrity II. How structural networks influence cellular information processing networks." J Cell Sci **116**(8): 1397-1408.

Jardine, L. (2003). The Curious Life of Robert Hooke. Great Britain, HarperCollins.

Katsumoto T., A. Mitsushima et al. (1990). "The role of the vimentin intermediate filaments in rat 3Y1 cells elucidated by immunoelectron microscopy and computer-graphic reconstruction." Biol Cell **68**(2): 139-146.

Kha, H.N., B.K. Chen et al. (2004). "Stiffness properties for nucleus standard straight and contour electrode arrays." Med Eng Phys **26**: 677-685.

Lakes, R.S. (2009). Viscoelastic Materials. Wisconsin, Cambridge University Press.

Lammerding, J., K.N. Dahl et al. (2007). "Nuclear Mechanics and Methods." Method Cell Biol **83**: 269-294.

Lammerding, J., L.G. Fong et al. (2006). "Lamins A and C but not lamin B1 regulate nuclear mechanics." J Biol Chem **281**: 25768-25780.

Lammerding, J., P.C. Schulze, et al. (2004). "Lamin A/C deficiency causes defective nuclear mechanics and mechanotransduction." J Clin Invest **113**: 370-378.

Lamond, A.I. and W.C. Earnshaw (1998). "Structure and Function in the Nucleus." Science **280**: 547-553.

Lee, G.U., D.A. Kidwell et al. (1994). "Sensing Discrete Streptavidin-Biotin Interactions with Atomic Force Microscopy." Langmuir **10**(2): 354-357.

Lehenkari, P.P. and M.A. Horton (1999). "Single integrin molecule adhesion forces in intact cells measured by atomic force microscopy." Biochem Biophys Res Commun **259**: 645-650.

Lin, F., D.L. Blake at al (2000). "MAN1, an inner nuclear membrane protein that shares the LEM domain with lamina-associated polypeptide 2 and emerin." J Biol Chem **275**: 4840-4847.

Lodish, H., A. Berk, P. Matsudaira, C.A. Kaiser, M. Krieger, M.P. Scott, S.L. Zipursky, J. Darnell (2004). Molecular Cell Biology. New York, W.H. Freeman.

Luger, K., A.W. Mäder et al. (1997). "Crystal structure of the nucleosome core particle at 2.8A resolution". Nature **389**(6648): 251–260.

Malhas, A., C.F. Lee et al. (2007). "Defects in lamin B1 expression or processing affect interphase chromosome position and gene expression." J Cell Biol **176**: 593-603.

Manilal, S., T.M. Nguyen et al. (1996). "The Emery-Dreifuss muscular dystrophy protein, emerin, is a nuclear membrane protein." Hum Mol Genet **5**(6): 801-808.

Maniotis, A.J., C.S. Chen et al. (1997). "Demonstration of mechanical connections between integrins, cytoskeletal filaments, and nucleoplasm that stabilize nuclear structure." Proc Natl Acad Sci USA **94**: 849-854.

Marko, J.F. and M.G. Poirier (2003). "Micromechanics of chromatin and chromosomes." Biochem Cell Biol **81**: 209-220.

Maxfield, F.R. and D. Wüstner (2002). "Intracellular cholesterol transport." J Clin Invest **110**(7): 891-898.

McCrum, N.G., C.P. Buckley et al. (1997). Principles of Polymer Engineering. Oxford University Press, 117-176.

Mejat, A. and T. Misteli (2010). "LINC complexes in health and disease." Nucleus **1**(1): 40-52.

Meyers, M.A. and K.K. Chawla (1999). Mechanical Behavior of Materials. Prentice Hall, Inc., 570-580.

Muchir, A., G. Bonne et al. (2000). "Identification of mutations in the gene encoding lamins A/C in autosomal dominant limb girdle muscular dystrophy with atrioventricular conduction disturbances (LGMD1B)." Hum Molec Genet **9**(9): 1453-1459.

Neuman, K.C. and A. Nagy (2008). "Single-molecule force spectroscopy: optical tweezers, magnetic tweezers and atomic force microscopy." Nat Methods **5**: 491-505.

Newport, J.W. and D.J. Forbes (1987). "The Nucleus: Structure, Function and Dynamics." Ann Rev Biochem **56**:535-565.

Padiath, Q.S., K. Saigoh et al. (2006). "Lamin B1 duplications cause autosomal dominant leukodystrophy." Nature Genet **38**(10): 1114-1123.

Paine P., L. Moore, et al. (1975). "Nuclear envelope permeability." Nature **254**(5496): 109–114.

Pajerowski, J. D., K.N. Dahl et al. (2007). "Physical plasticity of the nucleus in stem cell differentiation." Proc Natl Acad Sci USA **104**: 15619-15624.

Palazzo, A.F., C.H. Eng et al. (2004). "Localized Stabilization of Microtubules by Integrin- and FAK-Facilitated Rho Signaling." Science **303**(5659): 836-839.

Paulson, J.R. and U.K. Laemmli (1977). "The structure of histone-depleted metaphase chromosomes." Cell **12**(3): 817-828.

Peeters, E.A.G, C.V.C. Bouten et al. (2003). "Monitoring the biomechanical response of individual cells under compression: a new compression device." Med Biol Eng Comput **41**: 498-503.

Pellegrin, S. and H. Mellor (2007). "Actin stress fibres." J Cell Sci **120**: 3491-3499.

Pelling, A.E. and M.A. Horton (2008). "An historical perspective on cell mechanics." Eur J Physiol **456**: 3-12.

Pelling, A. E., F. S. Veraitch, et al. (2009). "Mechanical dynamics of single cells during early apoptosis." Cell Motil Cytoskeleton **66**(7): 409-422.

Philimonenko, V.V., J. Flechon et al. (2001). "The Nucleoskeleton: A Permanent Structure of Cell Nuclei Regardless of Their Transcriptional Activity." Exp Cell Res **264**: 201–210.

Porter, K.R., A. Claude et al. (1945). "A study of tissue culture cells by electron microscopy." J Exp Med **81**(3): 233-246.

Radmacher, M., M. Fritz at al (1996). "Measuring the viscoelastic properties of human platelets with the atomic force microscope." Biophys J **70**: 556-567.

Radmacher, M., R. W. Tillamnn, et al. (1992). "From molecules to cells: imaging soft samples with the atomic force microscope." Science **257**(5078): 1900-1905.

Razafsky, D. and D. Hodzic (2009). "Bringing KASH under the SUN: the many faces of nucleo-cytoskeletal connections." J Cell Biol **186**(4): 461-472.

Reinhard, M., J. Zumbrunn et al. (1999). "An alpha-actinin binding site of zyxin is essential for subcellular zyxin localization and alpha-actinin recruitment." J Biol Chem USA **274**(19): 13410–13418.

Roux, K.J., M.L. Crisp et al. (2009). "Nesprin 4 is an outer nuclear membrane protein that can induce kinesin-mediated cell polarization." Proc Natl Acad Sci USA **106**(7): 2194-2199.

Rowat, A.C., L.J. Foster et al. (2005). "Characterization of the elastic properties of the nuclear envelope." J R Soc Interface **2**:63-69.

Rowat, A.C., J. Lammerding et al. (2006). "Mechanical Properties of the Cell Nucleus and the Effect of Emerin Deficiency." Biophys J **91**: 4649-4664.

Schape, J., S. Prausse et al. (2009). "Influence of lamin A on the mechanical properties of amphibian oocyte nuclei measured by atomic force microscopy." Biophys J **96**: 4319-4325.

Schinkinger, S., F. Wottawah et al. (2004). "Feeling for cells with light." Proc of SPIE **5514**: 170-178.

Silberberg, Y. R., A. E. Pelling, et al. (2008). "Mitochondrial displacements in response to nanomechanical forces." J Mol Recognit **21**(1): 30-36.

Sims, J.R., S. Karp et al. (1992). "Altering the cellular mechanical force balance results in integrated changes in cell, cytoskeletal and nuclear shape." J Cell Sci **103**: 1215-1222.

Spector, D. (1993). "Macromolecular Domains within the Cell Nucleus." Annu. Rev. Cell BioI. **9**: 265-315.

Stamenovic, D. (2008). "Rheological behavior of mammalian cells." Cell Mol Life Sci **65**: 3592-3605.

Starr, D.A. (2005). "A nuclear-envelope bridge positions nuclei and moves chromosomes." J Cell Sci **122**(5): 577-586.

Starr, D.A. and J.A. Fischer (2005). "KASH 'n Karry: the KASH domain family of cargo-specific cytoskeletal adaptor proteins." Bioessays **27**(11): 1136-1146.

Starr, D.A. and H.N. Fridolfsson (2010). "Interactions between Nuclei and the Cytoskeleton are Mediated by SUN-KASH Nuclear-Envelope Bridges." Annu Rev Cell Dev Biol **26**: 9.1-9.24.

Stuurman, N., S. Heins et al. (1998). "Nuclear lamins: their structure, assembly, and interactions." J Struct Biol **122**: 42-66.

Tang, C.W., A. Maya-Mendoza et al. (2008). "The integrity of a lamin-B1-dependent nucleoskeleton is a fundamental determinant of RNA synthesis in human cells." J Cell Sci **121**: 1014-1024.

Theret, D.P., M. J. Levesque et al. (1988). "The application of a homogeneous half-space model in the analysis of endothelial cell micropipette measurements." J Biomech Eng **110**: 190-199.

Thoumine, O., A. Ott et al. (1997). "Time scale dependent viscoelastic and contractile regimes in fibroblasts probed by microplate manipulation." J Cell Sci **110**(17): 2109-2116.

Ting, T.C.T (1966). "The contact stresses between a rigid indenter and a viscoelastic half-space." J Appl Mech **88**: 845-854.

Tweedie, C.A. and K.J. van Vliet (2006). "Contact creep compliance of viscoelastic materials via nanoindentation." J Mater Res **21**(6): 1576-1589.

Vaziri, A., H. Lee et al. (2006). "Deformation of the cell nucleus under indentation: Mechanics and mechanisms." J Mater Res **21**(8), 2126-2135.

Vaziri, A. and M.R. Mofrad (2007). "Mechanics and deformation of the nucleus in micropipette aspiration experiment." J Biomech **40**: 2053-2062.

Venter, J.C., M.D. Adams et al. (2001). "The sequence of the human genome." Science **291**(5507): 1304-1351.

Vicente-Manzanares, M., M. Xuefei et al. (2009). "Non-muscle myosin II takes centre stage in cell adhesion and migration." Nat Rev Mol Cell Bio **10**: 778-790.

Wagner, N. and G. Krohne (2007). "LEM-Domain proteins: new insights into lamin-interacting proteins." Int Rev Cytol **261**:1-46.

Wang, N., J.D. Tytell et al. (2009). "Mechanotransduction at a distance: mechanically coupling the extracellular matrix with the nucleus." Nat Rev Mol Cell Biol **10**: 75-82.

Waterham, H.R., J. Koster et al. (2003). "Autosomal recessive HEM/Greenberg skeletal dysplasia is caused by 3-beta-hydroxysterol delta(14)-reductase deficiency due to mutations in the lamin B receptor gene." Am J Hum Genet **72**(4): 1013-1017.

Wilhelmsen, K., S.H. Litjens et al. (2005). "Nesprin-3, a novel outer nuclear membrane protein, associates with the cytoskeletal linker protein plectin." J Cell Biol **171**(5): 799-810.

Worman, H.J. and G. Bonne (2007). "'Laminopathies': a wide spectrum of human diseases." Exp Cell Res **313**: 2121-2133.

Worman, H.J. and G.G. Gunderson (2006). "Here come the SUNs: a nucleocytoskeletal missing link." Trends Cell Biol **16**(2): 67-69.

Wu, H.W., T. Kuhn et al. (1998). "Mechanical Properties of L929 Cells Measured by Atomic Force Microscopy: Effects of Anticytoskeletal Drugs and Membrane Crosslinking." Scanning **20**(5): 389-397.

Wurm, Y., J. Wang et al. (2011). "The genome of the fire ant *Solenopsis invicta*." Proc Natl Acad Sci USA **108**(14): 5679-5684.

Zaidel-Bar, R., M. Cohen et al. (2004). "Hierarchical assembly of cell matrix adhesion complexes." Biochem Soc T **32**(3): 416-420.

Zamir, E. and B. Geiger (2001). "Molecular complexity and dynamics of cell–matrix adhesions." J Cell Sci **114**(20): 3583-3590.

Zhang, Q., J.N. Skepper et al. (2001). "Nesprins: a novel family of spectrin-repeat-containing proteins that localize to the nuclear membrane in multiple tissues." J Cell Sci **114**: 4485-4498.

Zlatanova, J., S.H. Leuba et al. (2002). "Stretching and imaging single DNA molecules and chromatin." J Muscle Res Cell Motil **23**: 377-395.

Chapter 2

Instrumentation

2.1 Microscopy Techniques

This thesis will demonstrate the effect of an applied force on the nucleus of NIH3T3 fibroblast cells. These cells come from an established cell line originally obtained from mouse embryos, which has now become the standard fibroblast line (Todaro & Green 1963; Hsu, Barry et al. 1984). 3T3 cells were subjected to an applied force using an Atomic Force Microscope (AFM) while imaging was simultaneously carried out using a Laser-Scanning Confocal Microscope (LSCM). The nucleus was visualized in real time, so that its deformation in response to the applied force could be quantified and studied. In order to accomplish this, cells were stained with DNA-labeling fluorescent dyes in order to make them visible by confocal microscopy. In this section, I describe in detail the advanced microscopy and imaging techniques used in the experiments performed in this thesis.

2.1.1 Atomic Force Microscopy

The Atomic Force Microscope (AFM), one of the foremost tools for imaging, measuring, and manipulating matter at the nanoscale, was developed five years after its precursor, the Scanning Tunnelling Microscope (STM). Primarily used to measure topographies and surface properties of conductive materials at atomic resolution (Binnig, Rohrer et al. 1982; Baro, Miranda et al. 1985; Binnig, Frank et al. 1985; Binnig, Quate et al. 1986; Hansma, Elings et al. 1988) the STM operates by raster-scanning the surface with an extremely sharp tip to which a bias voltage has been applied.

If the sample is sufficiently conductive, a tunneling current, brought about by the quantum mechanical effect of electron tunneling through a vacuum, can be measured (Binnig, Rohrer et al. 1982). Changes in this measured current can then be related directly to changes in height between the sample and the tip in a highly sensitive manner. This current (I) exponentially decays with distance as:

$$I \propto e^{-\frac{\sqrt{2m\Phi}}{\hbar}d} \quad [14]$$

where d is the barrier distance in Å, m is the mass of an electron, Φ is the energy barrier in eV (dependent on the applied voltage) and ħ is Planck's constant divided by 2π. An increase in

barrier distance of 2-5 Å, which is a typical atomic radius, will decrease the current by upwards of 3 magnitudes, indicating that the current measured is largely coming from the single atom at the end of the STM tip.

Its ability to achieve atomic resolution made use of the STM highly attractive in imaging biological samples as well. Advances in the technique were then made to enable imaging in ambient temperature and pressure (Baro, Miranda et al. 1985; Hansma, Elings et al. 1988; Drake, Prater et al. 1989), thus allowing biological samples such as bacteriophages, lipid membranes, and DNA in complex with enzymes to be studied with the STM (Baro, Miranda et al. 1985; Smith, Bryant et al. 1987; Barris, Knipping et al. 1988). Resolution was lacking, however, due to the fact that although certain biological samples are capable of conducting electrons, the currents measured from these are much weaker than those from metallic samples, and not all regions are fully resolvable on the atomic scale (Baro, Miranda et al. 1985; Hansma, Elings et al. 1988). In order to accommodate this, biological samples were coated in a thin conducting layer prior to imaging. Alternatively, this metallic coating could be separated from the sample and then used to produce a mask, which can then be imaged as in Transmission Electron Microscopy (TEM; Hansma, Elings et al. 1988). However, coating a sample in this manner allows for atomic resolution only of the metal coating, not of the actual sample underneath. This technique also makes it impossible to image any biological sample in its natural environment. In addition, the very sharp tip required for STM can also prove highly detrimental to soft biological samples which have not been further protected (Hansma, Elings et al. 1988). Ultimately, imaging biological samples with the STM unfortunately requires too many modifications in order to achieve true atomic resolution.

In contrast, the AFM, developed as an extension of the STM, makes use of a sharp tip to profile the topographical features of a sample through direct physical contact with the surface. This eliminates the need to measure changes in tunnelling current, and thus allows for imaging of non-conducting surfaces. Moreover, the AFM allows physical interaction forces between tip and sample to be measured (Butt, Cappella et al. 2005), and may also be operated in aqueous environments, over a range of temperatures. These features make it possible to use the AFM in probing biological samples within their native environment (Radmacher, Tillamnn et al. 1992).

2.1.1.1 Schematic of an Atomic Force Microscope

Similar to the STM, the AFM operates by having a sharp, usually pyramidal tip raster scanning the surface of the sample underneath. This tip is attached to a spring-like cantilever, typically silicon or silicon nitride (Zougagh & Rios 2009). When the tip is brought close to the sample surface, forces between the tip and the sample lead to deflection of the cantilever following Hooke's law:

$$F = kx \quad [15]$$

The above equation is valid for small displacements. These deflections are detected by means of a laser spot which is reflected off the upper surface of the cantilever and onto a quadrant detector. As seen in Fig. 2.1a, four photodiodes (or quadrants) are positioned symmetrically around the center, and each quadrant is separated from its adjacent quadrants by a narrow gap. Position information can be obtained from the individual optical signals received by the quadrants, since these electrical contributions define the relative position of the light spot with respect to the gap position (Mäkynen, Ruotsalainen, et al. 2003). Displacements with respect to the gap position can then be approximated by:

$$\Delta x \approx k_{QD} \frac{(v_1 + v_2) - (v_3 + v_4)}{v_1 + v_2 + v_3 + v_4} \quad [16]$$

$$\Delta y \approx k_{QD} \frac{(v_1 + v_4) - (v_3 + v_2)}{v_1 + v_2 + v_3 + v_4} \quad [17]$$

where v_1, v_2, v_3 and v_4 are the average signal voltages of quadrants 1, 2, 3, and 4 respectively, while k_{QD} is a scale factor which converts relative displacements to absolute displacements, obtained from the geometry of the light spot. Thus, with the spring constant (k) of the cantilever known, all deflection measurements (x) can be directly converted to force (F) values (Meyer & Amer 1990; Carl & Schillers 2008).

In a typical set-up, the AFM is mounted onto a stationary stage while the scanning movement of the tip is controlled with a piezoelectric crystal. The sample is held stationary while the tip scans the surface, although sometimes the reverse is employed. The desired

magnitude of the applied force, also known as the setpoint value, is user defined, and a feedback loop corrects the piezo height in order to keep this force value constant.

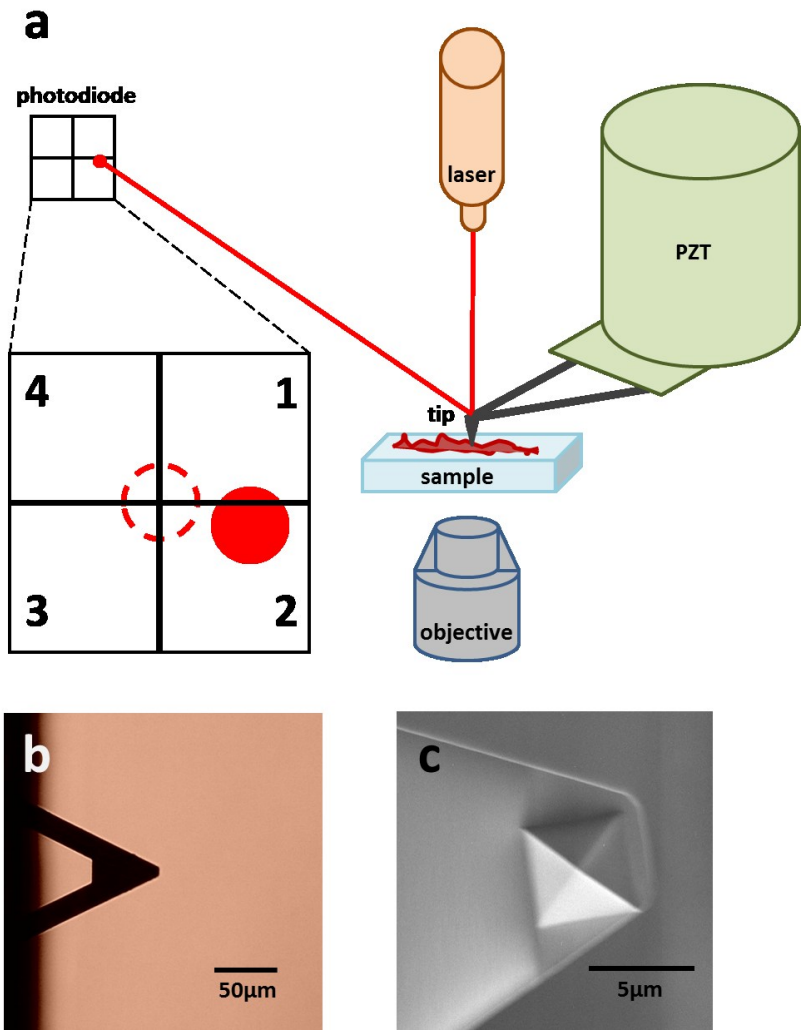

Figure 2.1 Components of the AFM. (a) Schematic representation of the AFM, with the quadrant photodetector (inset). The position of the laser spot relative to the center of the photodetector is due to the deflection of the cantilever. (b) A transmitted-light image shows a closer look at the cantilever, with its characteristic V-shape (discussed in Section 2.1.1.2). (c) Another image, taken using SEM (Scanning Electron Microscopy) shows the pyramidal tip.

Piezoelectric materials have the ability to expand and contract in response to an applied electric field due to the converse piezoelectric effect (Taylor, Gagnepain et al. 1985). In an AFM, the crystal employed expands and contracts in response to changes in voltage detected by the photodiode:

$$\Delta t_{out} = d_{ij} V_{IN} \quad [18]$$

A change in thickness of the piezo crystal (Δt_{out}) is caused by an applied voltage (V_{IN}) multiplied by the piezoelectric charge constant, d_{ij}. This constant describes the amount of strain experienced by the crystal due to an applied electric field. The subscripts i,j describe the axis of the crystal structure along which the electric field is being applied, and the axis along which the response occurs (Taylor, Gagnepain et al. 1985).

As mentioned earlier, my experiments with the AFM make use of a feedback system to quickly and accurately adjust the force applied on the sample and maintain the desired force value, corresponding to the setpoint voltage. The error signal, which is the difference between the detected voltage and the setpoint, is constantly minimized by the feedback loop. Typically operating in the 5 kHz regime, this mechanism serves to facilitate continuous and immediate force adjustments (Moheimani & Yong 2008). Specifically, my setup makes use of a closed-loop feedback system, in which strain gauges are coupled to the piezo scanner and measure the actual change in piezo height when the error signal is not zero. The strain gauge measurement is compared to the desired height change, and any necessary corrections (for instance, due to hysteresis in the piezo expansion) are made (Lapshin 1993).

The speed and accuracy of the feedback adjustments can be controlled using gains, as in the Proportional-Integral (PI) control system used in my setup. The P gain directly multiplies the error signal and proportionately affects the drive signal to expand or contract the piezo. However, in this case, the setpoint is often overshot due to hysteresis of the piezo (Lapshin 1993). In order to correct for this, the I gain dampens the response of the P gain by taking into account the changing discrepancy between the setpoint and current values. This effectively reduces the time it takes to return to the setpoint, while also eliminating the overshoot that occurs when the P gain is used alone (Barr 2002). Ideally, the P and I gains are maintained at as high a value as possible to decrease the response time, but not so high that the piezo crystal begins to resonate. With proper use of this feedback system, the force applied by the AFM tip onto the sample can be maintained at a constant value throughout the course of an experiment.

2.1.1.2 Cantilever Calibration

In order to measure the force between the AFM tip and sample during experiments using Equation 4, the spring constant of the cantilever must be experimentally determined. There have been numerous methods developed for accurately determining the spring constant of cantilevers (Cleveland, Manne et al. 1993; Lévy & Maaloum 2002; Gibson, Weeks et al. 2003; Bonaccurso & Butt 2005; Golovko, Haschke et al. 2007). Alternatively, values for spring constants which are quoted by the manufacturer can be determined mathematically from the material properties of the cantilever, in a method that has been extensively characterized (Sader 1995). The spring constant (k) for V-shaped cantilevers, as are used in this thesis, can be determined from the following:

$$k = \frac{Et^3w}{2L^3}\left(\cos\theta\left[1+\left(\frac{4w^3}{b^3}\right)(3\cos\theta-2)\right]^{-1}\right) \quad [19]$$

where E is Young's Modulus, t is the thickness of the cantilever, w is the width of a cantilever arm, L is the cantilever length, b is the total width of the cantilever base and θ is the angle between cantilever arms (Sader 1995).

Alternatively, the spring constant can also be determined mathematically in terms of the cantilever thickness (t), the surface area of the top face of the cantilever (A), the density (ρ), and the resonant frequency (ν) in air:

$$k = 4\pi^2 n\rho At(1.04\nu)^2 \quad [20]$$

Here, the factor of 1.04 is introduced in order to account for the effect of damping in air of V-shaped cantilevers, and n is a geometry-dependent correction factor which can be obtained from tables of values that have been previously calculated (Sader 1995).

Most commercial cantilevers, however, are coated with a thin layer of gold or aluminum. This changes the density and the effective Young's modulus of the cantilever, which in turn changes the resonant frequency as well. While the above calculations do not take these into account, for coatings thinner than 100 nm these changes are not significant (Gibson, Weeks et al. 2003). This allows for a simpler treatment of these equations, with an average density (ρ) of the cantilever defined as:

$$\rho = \rho_1 + \frac{\rho_c t_c}{t} \quad [21]$$

where ρ_1 is the density of the cantilever substrate, and ρ_c and t_c are the density and thickness of the coating, respectively. Incorporating this expression into equation 9 and equating the result with equation 8 provides one final, solvable equation in terms of only E, ρ_1 and t_c.

For silicon cantilevers, E and ρ do not vary significantly, and the thickness of the coating generally falls between 10 and 50 nm. This variance does not adversely affect the accuracy of k because the value is so small (Gibson, Weeks et al. 2003). However, silicon nitride cantilevers have a much larger variation in E and ρ, and there is also a significant variation in geometrical parameters even within cantilevers produced from the same batch. This increases the importance of determining spring constants experimentally.

There are a number of methods that can be used to accurately determine the value of k. The one employed to calibrate all the cantilevers used throughout the experiments in this thesis is called the thermal noise method (Hutter & Bechhoefer 1993; Lévy & Maaloum 2002). The cantilever is modeled as a harmonic oscillator with one degree of freedom that fluctuates in response to thermal energy. The Hamiltonian (H) for such an oscillator can be written as:

$$H = \frac{p^2}{2m} + \frac{1}{2} m\omega_0^2 x^2 \quad [22]$$

where x is the displacement of the oscillator, m is its mass, p its momentum and ω_0 the resonant frequency (Hutter & Bechhoefer 1993). The equipartition theorem states that the average value of each of the terms on the right-hand side of this equation is equal to $\frac{1}{2}k_BT$, where T is the temperature, and k_B is Boltzmann's constant:

$$\frac{1}{2} k_B T = \langle \frac{1}{2} m\omega_0^2 x^2 \rangle \quad [23]$$

The spring constant can be determined directly from the resonant frequency as $k = m\omega_0^2$, finally leading to:

$$k = \frac{k_B T}{\langle x^2 \rangle} \quad [24]$$

To eliminate sources of noise in the measurements, the average displacement is examined in the frequency domain (producing a power spectrum, seen in Figure 2.2), where it is easy to separate noise contributions from the peak corresponding to the resonant frequency. A Lorentzian curve is fitted to the amplitude-frequency relationship for the cantilever, modeled as a simple harmonic oscillator:

$$A(f) = \eta^2 + A_{DC}^2 \left(\frac{f_0^4}{(f^2 - f_0^2) + \frac{f^2 f_0^2}{Q^2}} \right) \quad [25]$$

where A_{DC} is the D.C. amplitude, η the background noise, Q the quality factor and f_0 the resonant frequency of the cantilever.

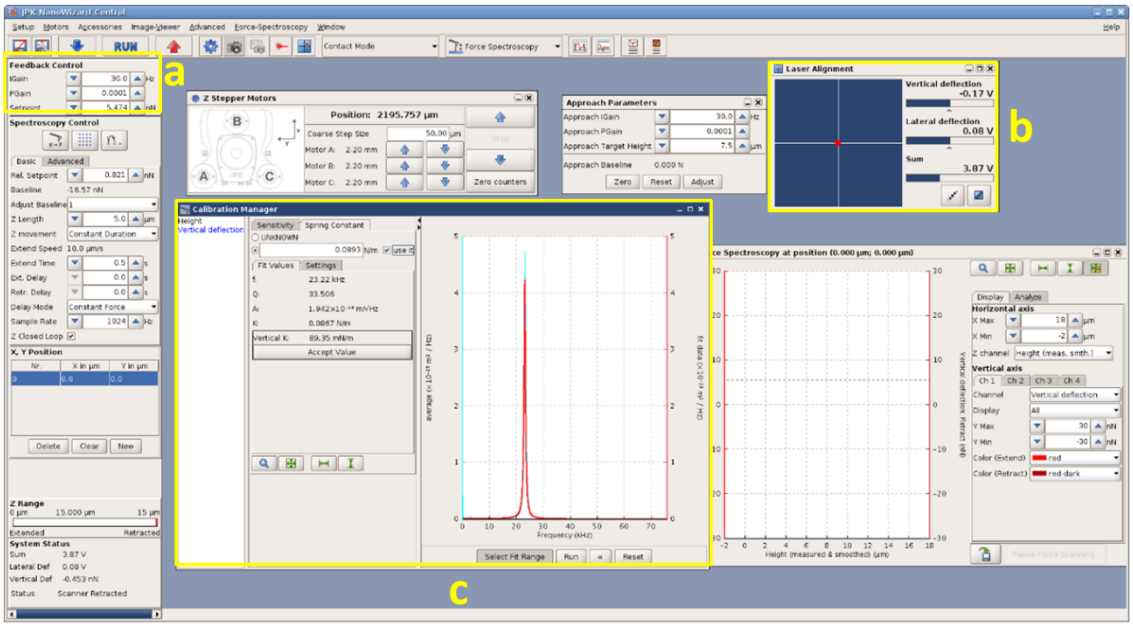

Figure 2.2 AFM user interface. The AFM used in my experiments is a NanoWizard II (JPK Instruments), controlled by JPK software. The figure above is a screen capture after spring constant calibration, with several features highlighted in yellow. (a) The feedback control window allows the user to adjust the P and I gains (discussed in Section 2.1.1.1). Also shown are (b) the laser alignment window depicting the quadrant photodetector, and (c) the cantilever power spectrum, with the fit (red) of the principal peak.

The integral of the Lorentzian fit to the resonant frequency peak in the power spectrum is equal to the mean square displacement of the cantilever in the time domain, $\langle x^2 \rangle$, allowing for a direct determination of the spring constant. Values of k obtained in this manner have been

shown to correspond extremely well to those obtained mathematically (Hutter & Bechhoefer 1993; Lévy & Maaloum 2002).

2.1.1.3 Imaging Modes

The AFM may be operated in three main imaging modes (Drake, Prater et al. 1989; Zhong, Inniss et al. 1993; Giessibl 2003): contact mode, intermittent-contact mode, and non-contact mode (shown in Figure 2.3). Contact mode involves a stationary cantilever in direct contact with the sample, with the tip deflection used as a feedback signal. Contact mode AFM is almost always done when the overall force is repulsive; the tip will then be pushed away from the surface in response to changes in topography. This is the mode in which the AFM is most often operated, and there are two sub-divisions: constant-force and constant-height mode.

In constant-height mode, the cantilever scans the surface at the same height, regardless of changes in topography of the sample. As a result, the force changes in certain areas as the cantilever is deflected. In this mode a deflection map is created, which demonstrates changes in topography rather than displaying the topography itself. Flat areas of the sample appear neutral, whereas deflections up and down will appear as bright and dark bands. In constant-force mode, a feedback system (as described earlier) is used to maintain a setpoint force; the cantilever then adjusts its height above the sample in order to maintain this force as the sample is scanned. Here, the adjustments in piezo height are used to generate the topographical image. Finer details of the image can be obtained from the error signal measured by the feedback system: this vertical deflection map is created from the absolute deflections of the cantilever as it scans the surface, independent of the adjustments in piezo height.

One of the drawbacks to contact mode AFM arises from the adhesion and lateral forces between the tip and sample (Zhong, Inniss et al. 1993). These forces can be quite strong, causing the tip to 'snap-in' to the surface when it is close enough. This can lead to significant indentation on a softer sample, giving an artificial image of the surface topography and potentially damaging the sample. Another important thing to consider is the tip geometry: the sharper the tip, the more fine detail can be observed, at the cost of higher damage done to softer samples (Radmacher 2002). These disadvantages can be bypassed by the other two

imaging modes; while neither of these was used during the experiments performed in this thesis, we discuss them here for completeness.

In non-contact mode, the tip of the cantilever does not contact the sample surface. It is instead oscillated at a frequency slightly above its resonant frequency, and far enough above the surface of the sample so that no direct contact ever occurs. The amplitude of this oscillation is typically a few nanometers. Van der Waals forces and other long range interactions which extend above the sample surface act to decrease the resonance frequency of the cantilever. This change in resonant frequency is combined with a feedback loop system to maintain a constant oscillation frequency (or amplitude) by adjusting the average tip-to-sample distance (Giessibl 2003). Measuring the tip-to-sample distance at each data point allows the scanning software to construct a topographic image of the sample surface.

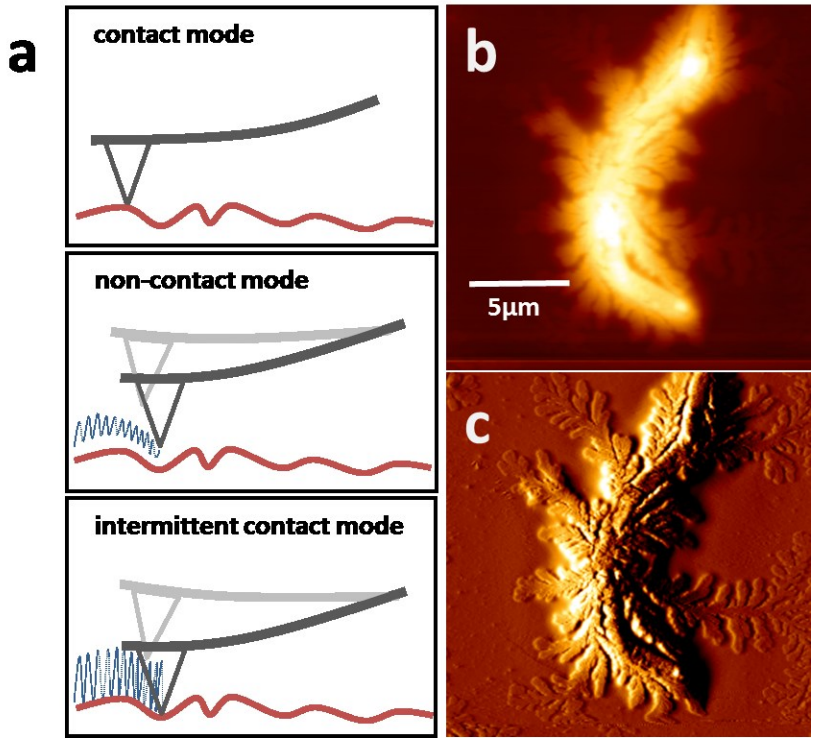

Figure 2.3 Imaging modes and AFM images. (a) Schematic representation of the AFM's three imaging modes. Within contact mode, the AFM can be used to produce (b) height images or (c) deflection images (sample: crystallized protein). Height images preserve true height information of the sample, whereas deflection images monitor the cantilever deflection from a straight line. While deflection imaging loses true height information, it is able to present finer details of the sample because the feedback loop response is faster in correcting the position of the small cantilever than for that of the piezoelectric element.

Non-contact mode is not without its own disadvantages, however. While it does not generally suffer from tip or sample degradation, many samples develop a liquid meniscus layer in ambient conditions. An AFM operating in contact mode will penetrate the liquid layer to image the underlying surface, but in non-contact mode the tip will oscillate above the fluid layer to image both the surface and the liquid as well. To combat this, intermittent contact mode was developed (Zhong, Inniss et al. 1993). The cantilever is driven to oscillate at or near its resonant frequency as in non-contact mode, but the amplitude of the oscillation is much higher (typically 100 to 200 nm). Interaction forces between the tip and the sample cause this amplitude to decrease as the tip gets closer to the sample. If the AFM feedback circuit is set to maintain constant amplitude, the topography of the sample may be determined.

It is clear that the AFM is an extremely powerful tool for use in studying and manipulating materials at the nanoscale. It has been used with great success in providing accurate, high-resolution images of biological samples and helping to demonstrate chemical interactions occurring in biological systems. Topographical AFM imaging has enabled visualization of sub-nuclear structures such as supercoiled DNA (Yoshimura, Ohniwa et al. 2000), NPCs (Danker & Oberleithner 2000), nucleosomes and higher-order chromatin (Sato, Ura et al. 1999; Hirano, Takahashi et al. 2008). The AFM has also been used to measure piconewton-scale forces arising from interactions between and within macromolecules (Baumgartner, Hinterdorfer et al. 2000; Evans, Leung et al. 2001; Hertadi & Ikai 2002). One particularly useful application of the AFM is as a tool for applying locally controlled forces to biological samples in order to investigate their mechanical response, as done in this thesis. While the AFM's various imaging modes are traditionally used to generate topographical images of both hard and soft materials, the experiments performed in this thesis employ a reliable technique not often exploited in AFM experiments on biological samples. This technique becomes even more powerful when it is used in tandem with high-powered optical microscopy techniques (Geisse 2009), such as confocal microscopy.

2.1.2 Confocal Microscopy

The confocal microscope is a variation on wide-field fluorescence microscopes. While light microscopes utilize white light to image samples through phase contrast, differences in the index of refraction, variance in transmitted light and many other techniques, fluorescence

microscopes rely on detecting emitted light from the sample itself. The sample must be illuminated with light of a wavelength which causes fluorescence in the material of interest. The light emitted by the resulting fluorescence, which in this case is at a longer wavelength than the source illumination, is then detected through a microscope objective (Spring, Davidson et al. 2008). Fluorescence microscopy normally requires the use of at least two filters: an excitation filter ensures the illumination is near monochromatic and at the correct wavelength, while a second, emission filter blocks the excitation light so that none of the source illumination reaches the detector.

A typical wide-field fluorescence microscope has the source flooding the entire sample evenly with light. All parts of the sample exposed within the optical path are excited at the same time, which means that the resulting fluorescence detected includes a large, unfocused background part. This and other limitations of traditional wide-field fluorescence microscopes motivated the conception of the confocal microscope. First patented in 1957 (Murphy 2001), the confocal microscope uses a spatial pinhole to block unfocused light in samples thicker than the focal plane (Pawley 2006). It is this elimination of all 'out-of-focus' signals reaching the detector that gives the confocal microscope its name.

2.1.2.1 Schematic of a Confocal Microscope

The key feature of the confocal microscope is its ability to optically section an image volume, acquiring light from only one plane of the sample at a time. It is designed such that the illumination, sample, and light detection system are all in focus with one another (‘confocal’). This results in all light emitted from above and below the image focal plane being blocked by the pinhole, and only light originating from the focal plane passing through.

In this thesis I use a laser-scanning confocal microscope (LSCM), in which the focal point of the excitation laser travels along each x-line in an x-y plane and quickly returns to the beginning of each line before imaging recommences, in a raster-scanning method. The beam is scanned across the sample in the x-y plane by using servo or piezo controlled mirrors. This way, as the laser scans over the focal plane of interest, a complete image of that plane is obtained pixel-by-pixel and line-by-line. One can also adjust the scan speed, with slower scans providing better signal-to-noise ratio and thus providing better contrast. Images of different focal planes

can be collected by raising or lowering the objective. By assembling a 'stack' of these 2D images from successive focal planes, a computer can generate a full three-dimensional image of the sample (Pawley 2006).

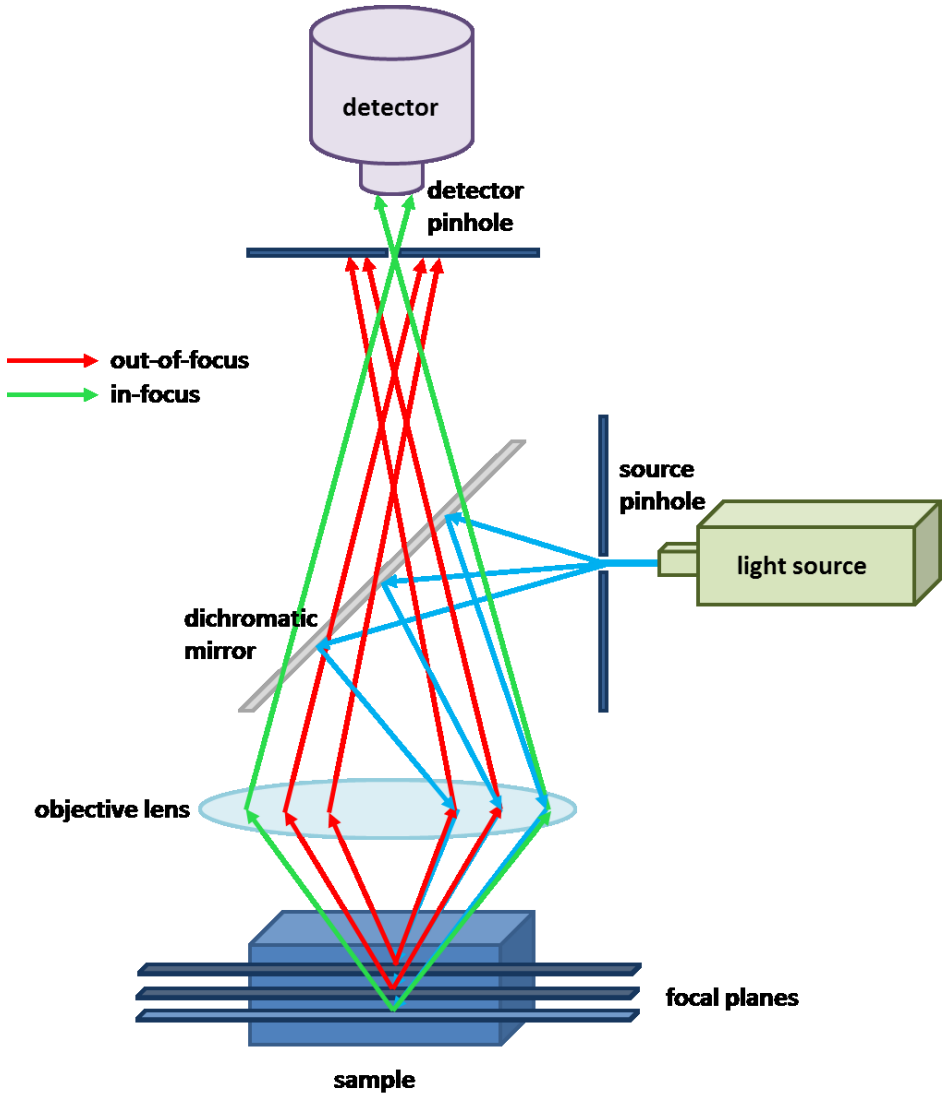

Figure 2.4 Schematic of a confocal microscope. Light of the excitation wavelength is reflected off the dichromatic mirror, through the objective and onto the sample, which then fluoresces. All of the light emitted from the sample, whether in-focus or otherwise, travels back up through the dichroic mirror, but only the in-focus light is able to pass through the detector pinhole.

Confocal microscopy has been used in tandem with other forms of microscopy. In this thesis, it has been combined with the AFM (as discussed in Section 1.4), in order to enable high-resolution imaging with simultaneous local force application.

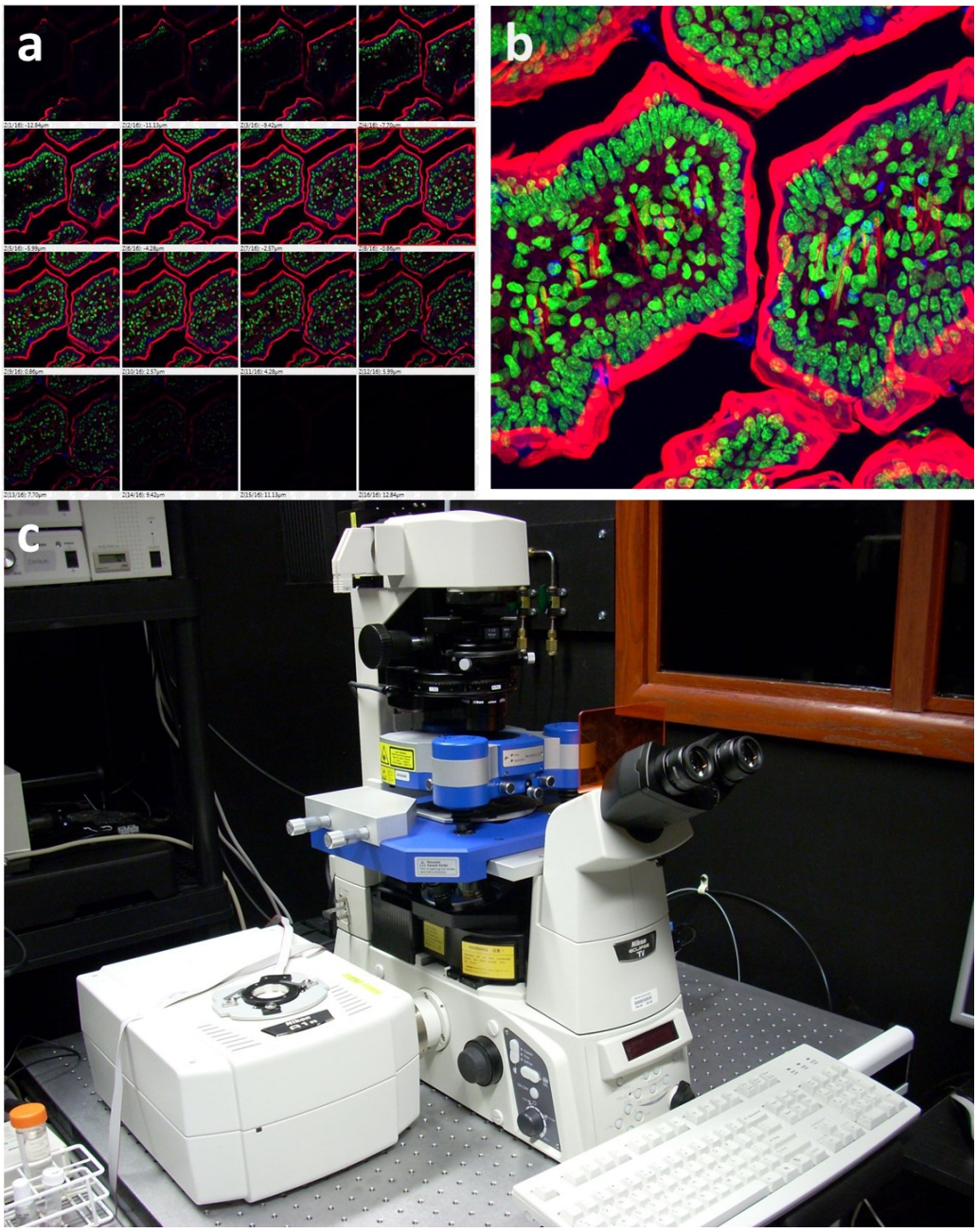

Figure 2.5 Imaging with the confocal microscope. (a) Individual, successive x-y slices are combined to form a full 3D stack (b). These images (sample: section of a mouse intestine) feature actin, nuclei and wheat germ agglutinin stained in red, green and blue, respectively. (c) This picture shows the Nikon Inverted TiE optical microscope connected to the Nikon A1R resonant scanning confocal microscope used in my setup, together with the NanoWizard II AFM unit (in blue).

2.1.2.2 Advantages of Confocal Microscopy

Confocal microscopy offers many advantages over other types of optical microscopy. For example, transmission electron microscopes regularly produce images with nanometer resolution, but they require extensive sample preparation and fixation and thus are not useful for live biological imaging. On the other hand, while conventional light and fluorescence microscopes allow imaging of living cells in their native environment, the fine details of sub-cellular structures still cannot be resolved past the diffraction limit.

The limit of diffraction (d) defines a radius at which two points of illumination are resolvable for a given microscope objective (Spring, Fellers et al. 2009):

$$d = \frac{0.61\lambda}{n \sin\theta} \quad [26]$$

where λ is the wavelength of the light used to image with, n is the refractive index of the objective, and θ is half the angle at which light beams converge from the objective to image the source. The denominator of this equation also defines the Numeral Aperture (NA) of the lens. Typical values for the NA of a lens range from 1.0-1.4, depending on whether the lens is used in air (n=1.00), water (n=1.33), or oil (n=1.51). As a typical light source used is 400-500 nm in wavelength, this means that the diffraction limit is approximately 200 nm for a conventional microscope, which is much larger than the distance between most structures within a cell.

The origin of the factor of 0.61 in equation 26 is the Rayleigh criterion, which states that for two Airy disks to be resolvable, the first minimum of an adjacent point-spread function (PSF) must coincide with the peak of the original PSF (Spring, Fellers et al. 2009). The advantage of using a confocal microscope is that the Airy disks are much thinner, owing to its unique pinhole design, and so the distance required to resolve them is smaller. This changes the factor in the numerator, leading to a smaller lateral resolution:

$$d_{lat} = \frac{0.41\lambda}{n \sin\theta} \quad [27]$$

The resolution is still highly dependent on the wavelength and numerical aperture, but the same degree of contrast can be achieved with a confocal microscope, at a smaller separation distance, with comparable wavelength and lenses as with conventional wide-field

fluorescence microscopes. Similarly, the axial resolution of a confocal microscope is also improved, due to the tightening of the Airy disks in the axial direction as described above. The axial resolution (d_{axial}) is dependent on the refractive index of the specimen medium (n_{med}), the wavelength (λ), and the square of the numerical aperture (NA):

$$d_{axial} = \frac{1.4\lambda n_{med}}{NA^2} \quad [28]$$

In addition, confocal microscopy is primarily distinguished by its ability to perform optical sectioning, where light is gathered for an image from only one plane of a sample volume at a time (Murphy 2001). This technique significantly improves axial resolution compared to wide-field fluorescence microscopy as light above and below the current plane are eliminated by the pinhole apparatus.

2.1.2.3 Variations and Enhancements to Confocal Microscopy

Traditional laser-scanning confocal microscopes (LSCM) have recently been adapted to image at video rate, also known as imaging in 'resonant mode' (Sanderson & Parker 2003; Borlinghaus 2006). Instead of using servo-controlled galvanometer mirrors to raster-scan the surface, as in 'galvano mode', the mirrors are mounted on piezo-scanning galvanometers which vibrate at a fixed frequency, moving the mirror in a rotational sinusoid. This increases the image acquisition rate (of full frame images, 512 x 512 pixels) from about 4 frames/second for typical galvano mode to upwards of 30 frames/sec in resonant mode (Larson, Schwartz et al. 2010). While there is some loss in resolution in resonant mode due to a decrease in the signal to noise ratio, this can be accommodated for with some loss in frame rate.

An alternative technique to LSCM is spinning-disk confocal microscopy (Egger & Petran 1967), where the aforementioned disk is a Nipkow disk containing a pattern of equally-distanced, identical pinholes. The sample can thus be scanned line-by-line by spinning the disk. Multiple points are imaged simultaneously as light passes through each pinhole, but due to their placement on the disk these pinholes are rapidly moved away from their initial positions as the disk spins (Ichihara 1996). This greatly increases the rate at which images can be obtained (up to 1000 frames/sec) and also reduces the light exposure, which is particularly useful for live imaging of biological samples (Nakano 2002), or for observing fast dynamics at

video rate. Spinning-disk confocal microscopy has been successfully used to study dynamic chromatin changes in mouse embryonic stem cells (Meshorer 2008).

In addition, several techniques have also been developed in recent years to surmount the diffraction limit (discussed in the previous section) even further. For example, Stimulated Emission Depletion (STED) microscopy makes use of nonlinear fluorescence de-excitation in order to overcome the resolution limit of standard LSCM (Hell & Kroug 1995; Rittweger, Han et al. 2009). Since LSCM involves the detector picking up light from the small region excited by the laser beam, the resolution is limited to the spot size to which the excitation spot can be focused, and adjacent structures in the same focal plane within a distance smaller than this spot cannot be resolved (Hell & Kroug 1995). In contrast, in a STED microscope the excited molecules in the outer rim of the excitation spot are additionally switched off by stimulated emission: if an excited fluorescent molecule is further irradiated with light of a wavelength similar to that of the fluorescence light, it can immediately return to the ground state while emitting a photon of the same wavelength and momentum as that of the light used (Saleh & Teich 1991). Thus fluorescent dyes can be switched off by additional irradiation of a 'de-excitation' beam with a higher wavelength. This 'de-excitation' beam is focused onto the sample, altering its wavefront in order to produce a ring-like intensity profile. This causes almost all of the excited molecules within this ring-shaped region to return to the ground state, leaving only the part of the sample very close to the center of the excitation spot excited, with this remaining fluorescence detected by the microscope. Using this technique, resolutions of up to 6 nm can be achieved (Rittweger, Han et al. 2009).

2.2 The Optical Stretcher

In my thesis I will also explore the effect of non-contact forces on the nuclei of non-adherent 3T3 fibroblasts. In contrast with the simultaneous AFM/LSCM experiments, which were performed with cells that had adhered onto a glass surface, experiments with the optical stretcher involved cells suspended in solution. These cells were then run through a microfluidic

channel, where a stretching force was provided by two identical laser beams from either side, as opposed to a directly applied normal force from an AFM tip.

The concept of utilizing light to manipulate and interact with biological materials is one that is well-established. Researchers first demonstrated successful optical 'trapping' of dielectric particles in the early 1970s (Ashkin 1970), by showing that forces arising due to radiation pressure from laser light were sufficient to enable levitation of small transparent glass spheres (Ashkin & Dziedzic 1971). Later, using a tightly focused beam of light that would come to be known as optical tweezers, they were able to hold microscopic particles such as glass, silica, and polystyrene latex beads stable in three dimensions (Ashkin, Dziedzic et al. 1986). Before the end of the decade they were able to successfully apply this technology to the biological sciences as well, using optical tweezers to trap an individual tobacco mosaic virus and *Escherichia coli* bacterium (Ashkin & Dziedzic 1987).

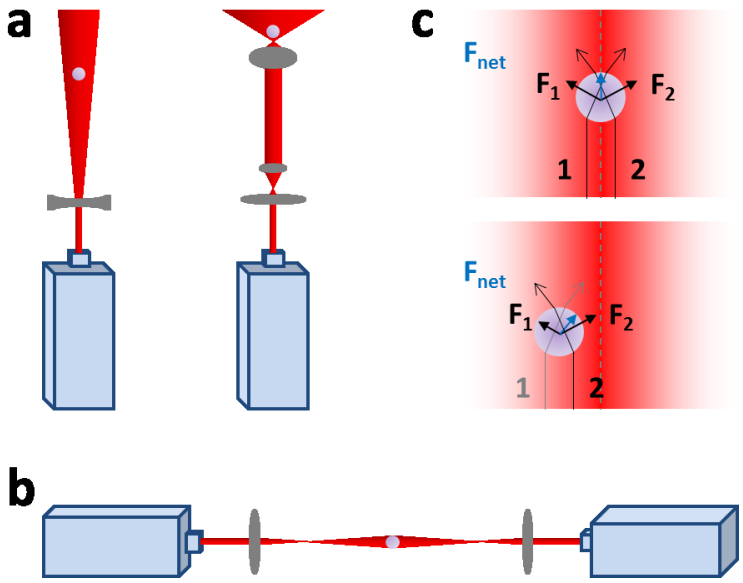

Figure 2.6 Common optical trap geometries. (a) Single-beam traps include the optical fountain (left) in which optical scattering forces are balanced by gravity, and optical tweezers (right) in which tightly focused laser light affords precise 3D manipulation of the trapped particle. (b) Counter-propagating laser beams produce a point where the scattering forces produced by the two laser beams cancel; this is the setup upon which the optical stretcher is based. (c) In an unfocused laser, the more intense rays impart a larger momentum change onto the particle, causing a net force to be applied back toward the center of the laser. A focused beam involves an additional intensity gradient that allows the particle to be suspended in a fixed axial position, thus `trapping` it.

While basic optical tweezers allow for non-invasive manipulation of small objects, adding the capacity to detect those objects (for example, with a light microscope) permits the simultaneous measurement of displacement and force. It is this capability that is exploited in optical force spectroscopy (Neuman & Nagy 2008). Interaction assays performed with optical tweezers have been used to determine the force and displacement generated by the individual kinesin molecules walking along microtubules (Block & Goldstein 1990; Svoboda, Schmidt et al. 1993). Similar assays also enabled measurement of the binding forces between single integrin-ligand (Litvinov, Shuman et al. 2002) and virus-erythrocyte pairs (Mammen, Helmerson et al. 1996).

One of the issues to consider with optical tweezers, as with most devices based on similar principles such as optical spanners (Simpson, Dholakia et al. 1997; Padgett & Allen, 1999), is the fact that they require focused laser beams in order to achieve their desired effects. This results in very high intensities at the focus of the trapping laser, typically on the order of 10^9-10^{12} W/cm^2. These intensities give rise to local heating, which can change the viscosity of the medium, affect enzymatic activity, and give rise to convection currents that affect the measurements (Neuman & Nagy 2008). But the greatest drawback is the risk of excessive radiation damage on the material exposed to the laser light. In the case of biological samples, the chance of opticution – that is, of damaging these biological samples beyond viability – is greatly increased.

There are certainly ways to make use of focused light without necessarily bringing about significant damage (Liang, Vu et al. 1996; Neuman, Chadd et al. 1999; Seol, Carpenter et al. 2006), but such techniques often demand conditions that limit the laser wavelength or maximum power used. This concern is bypassed by the optical stretcher, a device that provides an effective means of inducing controlled deformations on microscopic, elastic materials (such as cells) using unfocused laser beams. This minimizes the light flux through the cells and prevents unwanted radiation damage without imposing any limitations on the laser power used. Having this restriction lifted affords greater control over the experimental parameters, which in turn allows for more variety and flexibility in experimentation as a whole.

2.2.1 General Description

If we consider a ray of monochromatic light propagating in a medium with refractive index n, the momentum carried by this ray is expressed as:

$$p = \frac{En}{c} \quad [29]$$

where c is the speed of light in vacuum (Ashkin & Dziedzic 1973; Brevik 1979). The energy E can also be expressed as E = hf, where f is the frequency and h represents Planck's constant (h = 6.626 x 10^{-34}Js. Thus, even with very high frequencies (extreme ultraviolet light, for example, typically goes at above 10^{16}Hz) the momentum carried by a ray of light is usually of a magnitude too small to have any appreciable effect on a macroscopic scale. However, this is not true for objects whose sizes typically range from atomic to micron-level scales: due to their small masses, they are clearly affected by momenta of even these magnitudes. Optical tweezers rely on this in order to operate, and it is by a similar principle that the optical stretcher functions.

To illustrate how the optical stretcher works, I invoke a thought experiment outlined in previous literature (Guck, Ananthakrishnan et al. 1999), and shown in Figure 2.7. Consider a transparent dielectric cube of refractive index n_2 greater than that of the surrounding medium, n_1. If a ray of light strikes one face of the cube, normal to its surface, a fraction of it (around 0.1%) is reflected back. We make the assumption that the cube's absorption is negligible, so that all the remaining light enters the cube and is transmitted through it. At this point, due to the change in refractive index, the light experiences a corresponding change in momentum; since $n_2 > n_1$, the result is a momentum gain. On the other hand, once the light exits the cube it goes from media of higher to lower refractive index, and thus experiences a loss in momentum. At the surface, a similar fraction of the ray is reflected back into the cube, whereas the rest is free to exit it completely.

Thus the light ray experiences a change in momentum twice: once upon entering the cube, and once more upon leaving it. Conservation of momentum demands that these differences be accounted for, and they are in fact imparted unto the cube itself. It is then possible to express a change in momentum on each of the surfaces over an arbitrary small time period. Furthermore, if one is interested in approximating the instantaneous response of the

cube, shrinking the time interval to near zero changes the expression from Δp/Δt to dp/dt, which is equivalent to a force.

It appears then that the successive changes in momentum experienced by the light ray result in forces exerted on the affected surfaces of the cube. To obtain expressions for these forces, we first define the light power contained in the ray: P = ΔE/Δt. We can combine this with our previous definitions of force and momentum to set up an expression showing how the forces on the front and back surfaces (where the light enters and leaves, respectively) depend on light power and refractive index (Guck, Ananthakrishnan et al. 2002):

$$F = \frac{Pn}{c} \quad [30]$$

Equation 30 above assumes perfect transmission (all light is transmitted, with zero reflection and absorption) and a single refractive index. However, since the refractive index changes throughout the ray's journey in and out of the cube, and because not all of the light is transmitted through both surfaces, it becomes necessary to examine just how much of the light goes through (and how much is reflected) at every relevant point. If we represent the ratio of reflected light at any point as R, and consider only first-order reflections, we arrive at the results summarized in Figure 2.7 below:

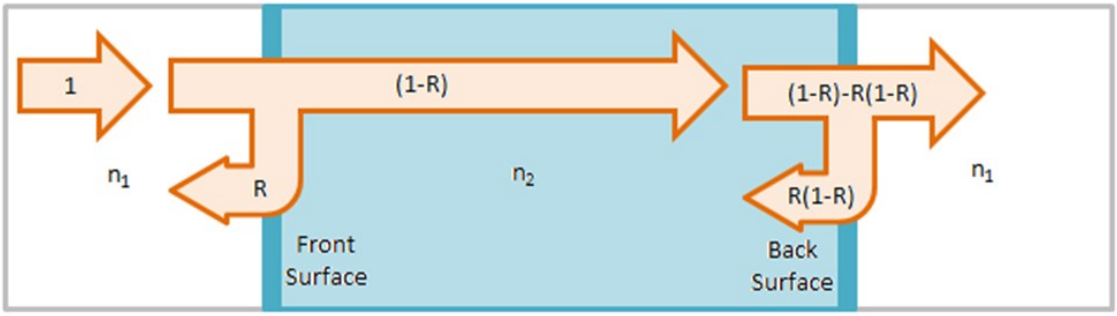

Figure 2.7 Light transmission and reflection from one ray incident from the front of a transparent dielectric cube. We ignore absorption and consider first-order reflections, taking the initial amount of light incident onto the front surface and normalizing it to 1. Upon striking the surface, an amount R << 1 is reflected back, whereas the remaining light (1-R) is transmitted through the cube of refractive index n_2. When this light hits the back surface, an additional fraction R x (1-R) is reflected back, while the rest of the light exits the cube.

As seen in Figure 2.7, the fraction of the incident light that finally exits the cube is (1-R) – R(1-R), or $(1-R)^2$. Since R is a very small number, we can disregard the higher-order reflections, whose ratios would be on the order of R^2, R^3, etc. Combining the above results with equation 30, we then obtain the desired expressions for the forces on the front and back surfaces of the cube (Guck, Ananthakrishnan et al. 1999):

$$F_{front} = \frac{P}{c}[n_1 - (1-R)n_2 + Rn_1] \quad [31]$$

$$F_{back} = \frac{P}{c}(1-R)[n_2 - (1-R)n_1 + Rn_2] \quad [32]$$

These two forces have opposite directions and both point away from the center of the cube. The cube then experiences an overall stretching force:

$$F_{stretch}(\text{one beam}) = \frac{1}{2}\left(|F_{front}| + |F_{back}|\right) \quad [33]$$

It is immediately clear from equations 31 and 32, however, that the magnitudes of the forces F_{front} and F_{back} are generally unequal. This implies the existence of a net force with magnitude (F_{back} - F_{front}) which has the added, unwanted effect of accelerating the cube along the direction of light propagation. An effective way to remedy this is to introduce another beam, identical to the first one but traveling in the opposite direction. If this second beam is propagating from the other side of the cube and made to strike its back surface, the two forces accelerating the cube cancel each other out completely, but the individual stretching forces add up (see Figure 2.8). Thus the net stretching force, from two counter-propagating light beams, is now double the initial value for only one beam.

If we now replace this hypothetical dielectric cube with a material which is sufficiently elastic, it can be deformed. Specifically, it is stretched along the beam axis by a net force with magnitude:

$$F_{stretch}(\text{two beams}) = |F_{front}| + |F_{back}| \quad [34]$$

To illustrate, Guck et al. performed stretching of erythrocytes, or red blood cells: they trapped red blood cells in solution and used a stretching power of P = 110 mW. Using n_1 = 1.33,

n_2 = 1.43 and R ≈ 10^{-3} in equations 31 and 32 gives rise to a total stretching force (equation 34) of 3.90 pN. The shear modulus (G_h) of a single typical erythrocyte is reported to be on the order of 8 x 10^{-6} N/m from micropipette aspiration experiments (Hochmuth 1993). One would then expect deformation on the order of $F_{stretch}/G_h$, or 0.48 µm. The actual deformation they measured was approximately 0.44 µm along the axis of the laser beams (Guck, Ananthakrishnan et al. 2001).

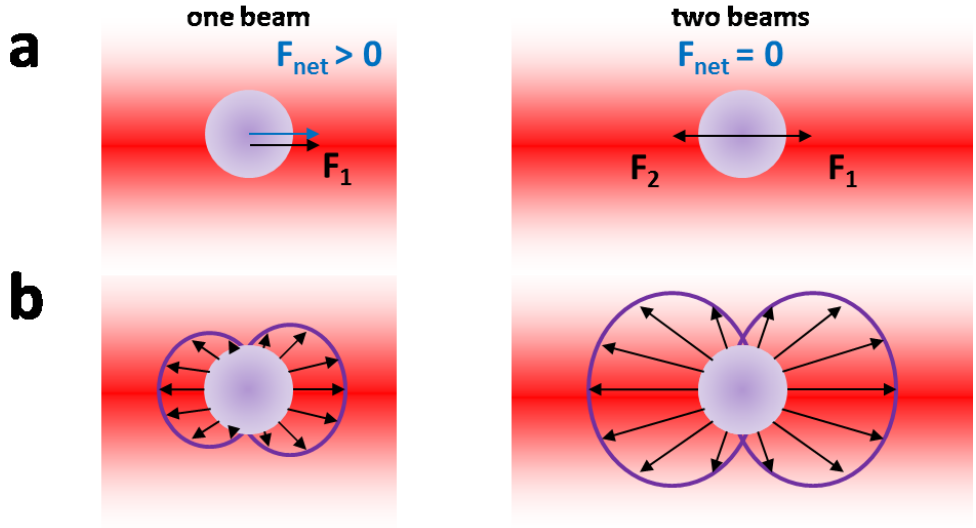

Figure 2.8 Forces experienced by the cell in single- and dual-beam optical traps. While net accelerating forces (a) due to asymmetry in the surface forces cancel out in the two-beam configuration, the surface forces themselves (b) add up. These surface forces yield a net stretching force that is exploited in the optical stretcher.

2.2.2 Schematic of an Optical Stretcher

The basic requirements are two axially-aligned, counter-propagating laser beams emanating from optical fibers aligned with a trapping region (Wang & Discher 2007). In the simplest, or open setup, the optical fibers are aligned against a straight-edged backstop (Constable, Kim et al. 1993; Guck, Ananthakrishnan et al. 2001). The fibers are usually mounted onto miniature three-axis translation stages. Cells suspended in solution are then pipetted onto the space between the fibers, which can then be translated along the backstop to move the trap into the path of cells of interest. This setup is sufficient for light cells (such as human red blood cells) that sink slowly enough to be trapped out of a cell suspension. However, it is difficult to maintain sterile conditions, and any debris attaching to the end of either fiber would

necessitate removing, cleaning, and realigning the fibers against the backstop once more (Wang & Dischер 2007). A slightly more involved setup, and the one used in this thesis, involves implementing some microfluidic control (Lincoln, Schinkinger et al. 2007). A square glass capillary serves as a flow channel, through which cells such as 3T3 fibroblasts suspended in solution can be streamed through. The laser beams are sent through the capillary walls in order to trap and stretch the cells inside.

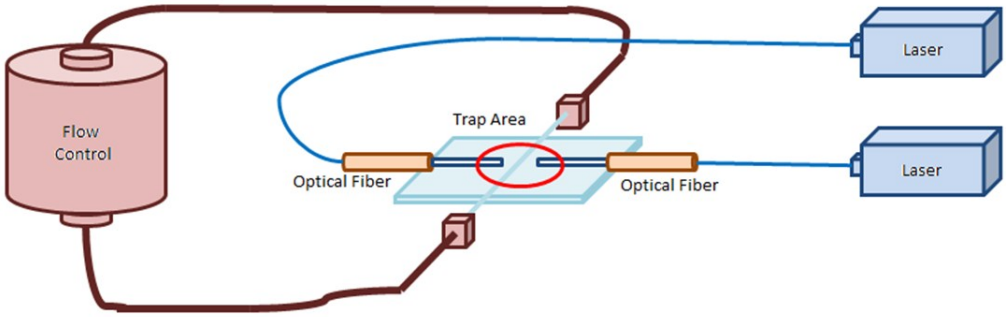

Figure 2.9 Schematic representation of a microfluidic optical stretcher. Optical trapping and stretching are performed by two identical, counter-propagating laser beams guided through optical fibers. Cells are suspended in medium and run through a glass capillary in the center of the trap.

The stability of the dual-beam optical trap is afforded by two key requirements: the size of the beams must be larger than the object being trapped, and the object itself must have a higher refractive index than its surrounding medium (Guck, Ananthakrishnan et al. 2001). Due to cylindrical symmetry of the laser's intensity profile, the accelerating force from each of the two beams only has a component in the direction of light propagation. If we assume the object starts out centered along the beam axis, displacing it from this axis breaks the symmetry of the system. This results in a gradient force, perpendicular to the axis, which arises due to conservation of momentum. The gradient force tends to pull the object towards the region of highest laser intensity (as seen in Figure 2.6c), which happens to be found at the center of the beam. Thus, regardless of where an object is placed between the beams, it will be pulled towards the center of the beam axis, after which it will stay there as long as both the gradient force and the external, accelerating forces sum up to zero.

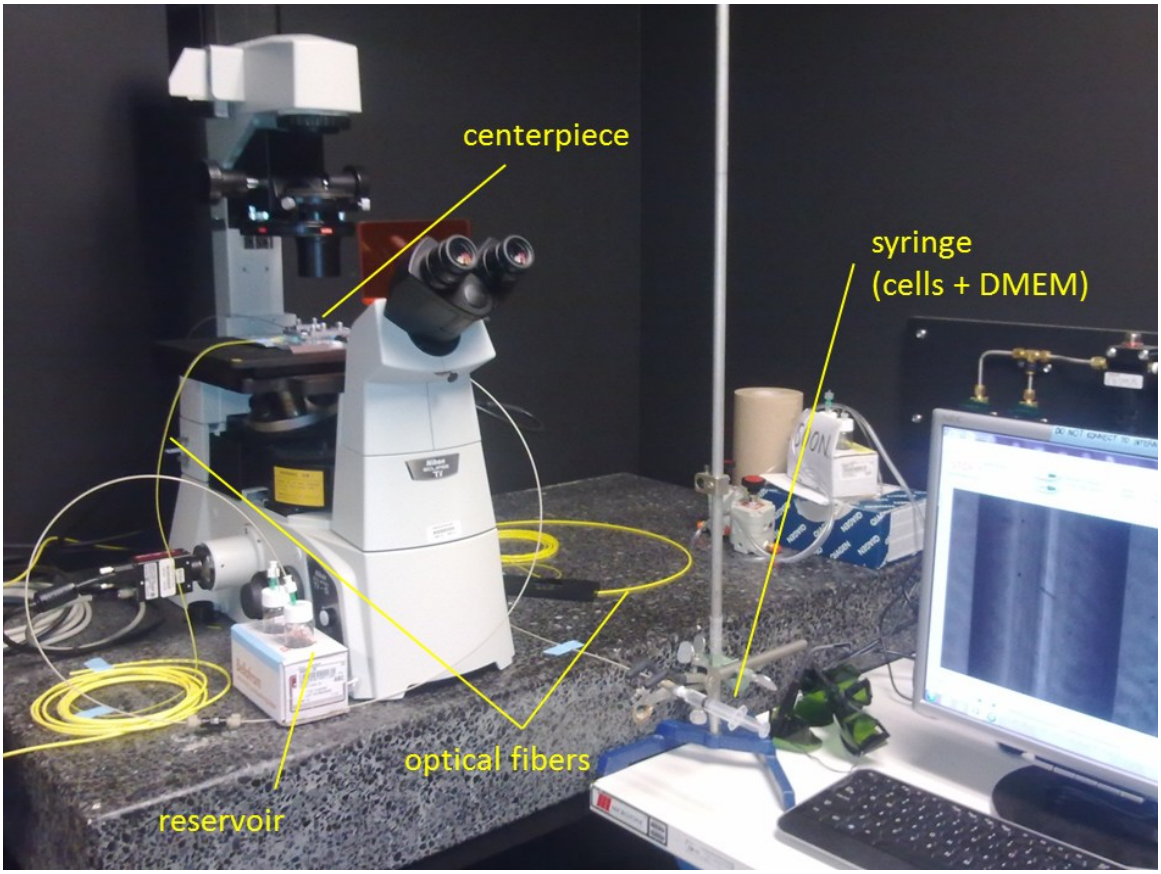

Figure 2.10 Optical stretcher. The main components of the optical stretcher used in my experiments are shown. Optical fibers coming from the light source (not shown) for the optical trap are mounted onto the centerpiece on the stage. The flow chamber is delineated by the syringe, capillary and reservoir, to be discussed further in Section 3.6.2.

2.3 Drug Treatments and Cell Techniques

Aside from studying nuclear deformation, in this thesis I also show how disrupting certain elements of the cytoskeleton (discussed in Section 1.2) affects this deformation. In particular, we targeted the actin and microtubule networks, first separately and then simultaneously, in 3T3 fibroblasts using anti-cytoskeletal drugs. Intermediate filaments, while not manipulated directly, were imaged in cells subjected to these drug treatments in order to observe how IFs, particularly vimentins, were affected by each one.

2.3.1 Anti-Cytoskeletal Drugs

A number of chemicals have been developed to take a specific action on the CSK and its associated proteins. Many have been used in experiments to selectively activate or inhibit aspects of the CSK in an effort to determine the specific role each cytoskeletal element plays in cell mechanics and other various cellular processes. Two of the most popular drugs, cytochalasin D and nocodazole (Rotsch & Radmacher 2000; Pelling, Dawson et al. 2007; Yuen, Zak et al. 2008; Pelling, Veraitch et al. 2009), are used in this thesis.

Cytochalasins are a family of mycotoxins that block polymerization and stop elongation of actin filaments. Cytochalasins bind to the plus ends of microfilaments and block both assembly and disassembly of individual actin monomers from these ends (Cooper 1987). Cytochalasin D, in particular, is a potent inhibitor of actin polymerization; concentrations as low as 0.2 μM have been found to be sufficient to disrupt actin treadmilling, the simultaneous growth and shrinking at opposite ends of dynamic filaments (Yahara, Harada et al. 1982). Nocodazole, on the other hand, is an agent that disrupts the MT network by blocking the self-assembly of tubulin subunits while also depolymerizing preformed microtubules as well (Samson, Donoso et al. 1979). Smaller concentrations of nocodazole, at the nM scale, can result in a decrease in elongation and shortening velocities of MTs, as well as an overall decrease in MT turnover after the treatment (Vasquez, Howell et al. 1997; Pelling & Dawson 2007).

Both of these drugs are extremely specific to the components they target. Treatment with nocodazole often leaves the actin network intact but destroys any inherent tubulin structure, whereas treatment with cytochalasin D generally leaves the cell with no actin fibers while MTs remain unaffected (Pelling, Dawson et al. 2007; Pelling, Veraitch et al. 2009).

2.3.2 Green Fluorescent Protein

The green fluorescent protein (GFP) was originally isolated from the jellyfish, *Aequorea victoria* (Prasher, Eckenrode et al. 1992), where it is largely responsible for the green lining on the inside of the otherwise translucent jellyfish. Fluorescence in jellyfish is produced from an energy transfer following the binding of calcium to a secondary bioluminescent protein, aequorin, which produces blue light (Prasher 1995; Misteli & Spector 1997). Its unique mechanism of generating light prompted the study of the nature of GFP, where it was

discovered that GFP may also be activated directly by an external ultraviolet light source (Chalfie, Tu et al. 1994).

Characterization of the crystal structure and sequence of GFP led to the generation of a number of genetic modifications which were designed to enhance its versatility and usefulness in molecular biology. These include, among others, a modification which brightens the emitted green signal, known as enhanced GFP (Cormack, Valdivia et al. 1996) and modifications which shift the fluorescence from green light to any number of other wavelengths, specifically those which coincide with readily available laser wavelengths (Heim & Tsien 1996). But perhaps the most important application developed from the discovery of GFP has to do with its value as a visible genetic tag, which allows for directly visualizing the localization and dynamics of proteins within biological systems. Genetic tagging is a well-known technique in molecular biology, involving the development of fusion proteins which have the GFP directly attached to each protein of interest. The mechanism by which this occurs is explained in more detail in the section below.

2.3.3 Transfection Techniques

Transfection, the process by which foreign genetic material is introduced to a eukaryotic cell, is a well-characterized technique (Watt, Sawicki et al. 1993; Felgner, Tsai et al. 1995; Bonetta 2005; Glover, Lipps et al. 2005). It is actually fairly easy to genetically modify cells to cause them to express proteins of interest once DNA has been introduced to the cell. In fact, the biggest challenge is how to get the DNA there in the first place, specifically moving it across the cell membrane without compromising the cell's integrity.

A number of techniques were developed in order to facilitate this. Initially, researchers made use of a chemical perforation technique, by which cells became temporarily permeable after incubation with calcium phosphate ions (Bonetta 2005). Viruses have also been used to facilitate transfection, by having researchers replace their DNA with the DNA of interest and let them loose to inject the DNA directly into the cell (Graham & van der Eb 1973). The last forty years have seen the development of other techniques using different carrier molecules, such as liposomes, positively-charged organic molecules, and other nanoparticles (Bonetta 2005; Han, Ghosh et al. 2007).

My experiments made use of the liposomal technique, in which plasmid DNA containing GFP-vimentin (a kind gift from Robert Goldman, Northwestern University) among other genes was amplified within E. coli cells. Bacteria are particularly suited for this purpose as they multiply at a very fast rate, and easily replicate plasmid DNA as well as their own. After amplification, the DNA was then isolated, quantified, and used for transfection. The technique also involved incubating the plasmid DNA with a solution of cationic lipids which accumulate around the negatively charged DNA, forming complexes of lipid/DNA (Lin, Slack et al. 2000). These liposomes were then placed in a dish with the 3T3 fibroblast cells. Through endocytosis, the process through which cells absorb molecules (such as liposomes) by engulfing them, the DNA can successfully cross the cytoplasm to the cellular interior.

2.4 References

Ashkin, A. (1970). "Acceleration and Trapping of Particles by Radiation Pressure." Phys Rev Lett **24**(4): 156-159.

Ashkin, A., J.M. Dziedzic et al. (1986). "Observation of a single-beam gradient force optical trap for dielectric particles." Opt Lett **11**(5): 288-290.

Ashkin, A. and J.M. Dziedzic (1971). "Optical levitation by radiation pressure." Appl Phys Lett **19**: 283-285.

Ashkin, A. and J.M. Dziedzic (1973). "Radiation pressure on a free liquid surface." Phys Rev Lett **30**: 139-142.

Ashkin, A. and J.M. Dziedzic (1987). "Optical trapping and manipulation of viruses and bacteria." Science **235**(4795): 1517-1520.

Baro, A.M., R. Miranda et al. (1985). "Determination of surface topography of biological specimens at high resolution by scanning tunnelling microscopy." Nature **315**(6016): 253-254.

Barr, M. (2002). Closed Loop Control. Embedded Systems Programming: 55-56.

Barris, B., U. Knipping et al. (1988). "Images of DNA fragments in an aqueous environment by scanning tunneling microscopy." Biopolymers **27**(10): 1691-1696.

Baumgartner, W., P. Hinterdorfer et al. (2000). "Cadherin interaction probed by atomic force microscopy." Proc Natl Acad Sci USA **97**: 4005-4010.

Binnig, G., K.H. Frank, et al. (1985). "Tunneling spectroscopy and inverse photoemission: Image and field states." Phys Rev Lett **55**(9): 991-994.

Binnig, G., H. Rohrer et al. (1982). "Surface Studies by Scanning Tunneling Microscopy." Phys Rev Lett **49**(1): 57-61.

Binnig, G., C.F. Quate, et al. (1986). "Atomic force microscope." Phys Rev Lett **56**(9): 930-933.

Block, S.M., L.S. Goldstein et al. (1990). "Bead movement by single kinesin molecules studied with optical tweezers." Nature **348**: 348-352.

Bonaccurso, E. and H.J. Butt (2005). "Microdrops on atomic force microscope cantilevers: evaporation of water and spring constant calibration." J Phys Chem B **109**(1): 253-263.

Bonetta, L. (2005). "The Inside Scoop- Evaluating Gene Delivery Methods." Nat Methods **2**(11): 875-883.

Borlinghaus, R.T. (2006). "MRT letter: high speed scanning has the potential to increase fluorescence yield and to reduce photobleaching." Microsc Res Tech **69**(9): 689-692.

Brevik, I. (1979). "Experiments in phenomenological electrodynamics and the electromagnetic energy-momentum tensor." Phys Rep **52**: 133-201.

Broers, J.L., N.M. Bronnenberg et al. (2002). "Partial cleavage of A-type lamins concurs with their total disintegration from the nuclear lamina during apoptosis." Eur J Cell Biol **81**: 677- 691.

Butt, H., B. Cappella et al. (2005). "Force measurements with the atomic force microscope: Technique, interpretation and applications." Surf Sci Rep **59**: 1-152.

Carl, P. and H. Schillers (2008). "Elasticity measurement of living cells with an atomic force microscope: data acquisition and processing." Eur J Physiol 457: 551-559.

Chalfie, M., Y. Tu et al. (1994). "Green fluorescent protein as a marker for gene expression." Science **263**(5148): 802-805.

Chen, C.S. (2008). "Mechanotransduction - a field pulling together?" J Cell Sci **121**: 3285-3292.

Cleveland, J.P., S. Manne et al. (1993). "A nondestructive method for determining the spring constant of cantilevers for scanning force microscopy." Rev Sci Instrum **64**: 403-405.

Constable, Kim et al. (1993). "Demonstration of a fiber-optical light-force trap." Opt Lett **18**(21): 1867-1869.

Cooper, J.A. (1987). "Effects of Cytochalasin and Phalloidin on Actin." J Cell Biol **105**(4): 1473-1478.

Cormack, B.P., R.H. Valdivia et al. (1996). "FACS-optimized mutants of the green fluorescent protein (GFP)." Gene **173**: 33-38.

Dahl, K.N., P. Scaffidi et al. (2006). "Distinct structural and mechanical properties of the nuclear lamina in Hutchinson-Gilford progeria syndrome." Proc Natl Acad Sci USA **103**: 10271-10276.

Danker, T. and H. Oberleithner (2000). "Nuclear pore function viewed with atomic force microscopy." Pflügers Arch - Eur J Physiol **439**: 671-681.

Drake, B., C.B. Prater et al. (1989). "Imaging crystals, polymers, and processes in water with the atomic force microscope." Science **243**(4898): 1586-1589.

Egger, M.D. and M. Petran (1967). "New reflected light microscope for viewing unstained brain and ganglion cells." Science **157**: 305-307.

Evans, E., A. Leung et al. (2001). "Chemically distinct transition states govern rapid dissociation of single L-selectin bonds under force." Proc Natl Acad Sci USA **98**: 3784-3789.

Felgner, P.L., Y.J. Tsai et al. (1995). "Improved cationic lipid formulations for in vivo gene therapy." Ann N Y Acad Sci **772**: 126-139.

Geisse, N.A. (2009). "AFM and Combined Optical Techniques." Mater Today **12**(7-8): 40-45.

Gibson, C.T., B.L. Weeks et al. (2003). "Calibration of AFM cantilever spring constants." Ultramicroscopy **97**: 113-118.

Giessibl, F.J. (2003). "Advances in Atomic Force Microscopy." Rev Mod Phys **75**: 949-983.

Glover, D.J., H.J. Lipps et al. (2005). "Towards safe, non-viral therapeutic gene expression in humans." Nat Rev Genet **6**(4): 299-310.

Golovko, D.S., T. Haschke et al. (2007). "Nondestructive and noncontact method for determining the spring constant of rectangular cantilevers." Rev Sci Instrum **78**(4): 043705.

Graham, F.L. and A.J. van der Eb (1973). "A new technique for the assay of infectivity of human adenovirus 5 DNA." Virology **52**(2): 456-467.

Guck, J., R. Ananthakrishnan et al. (1999). "Optical Deformability of Soft Biological Dielectrics." Phys Rev Lett **84**(23): 5451-5454.

Guck, J., R. Ananthakrishnan et al. (2001). "The Optical Stretcher: A Novel Laser Tool to Micromanipulate Cells." Biophys J **81**:767-784.

Guck, J., R. Ananthakrishnan et al. (2002). "Stretching biological cells with light." J Phys Condens Matter **14**: 4843-4856.

Han, G., P. Ghosh et al. (2007). "Multi-functional gold nanoparticles for drug delivery." Adv Exp Med Biol **620**: 48-56.

Hansma, P.K., V.B. Elings, et al. (1988). "Scanning tunneling microscopy and atomic force microscopy: application to biology and technology." Science **242**(4876): 209-216.

Heim, R. and R.Y. Tsien (1996). "Engineering green fluorescent protein for improved brightness, longer wavelengths and fluorescence resonance energy transfer." Curr Biol **6**(2): 178-182.

Hell, S.W. and M. Kroug (1995). "Ground-state depletion fluorescence microscopy, a concept for breaking the diffraction resolution limit." Appl Phys B **60**(5): 495-497.

Hertadi, R. and A. Ikai (2002). "Unfolding mechanics of holo- and apocalmodulin studied by the atomic force microscope." Protein Sci **11**: 1532-1538.

Hirano, Y., H. Takahashi et al. (2008). "Nuclear architecture and chromatin dynamics revealed by atomic force microscopy in combination with biochemistry and cell biology." Pflugers Arch - Eur J Physiol **456**: 139-153.

Hochmuth, R.M. (1993). "Measuring the mechanical properties of individual human blood cells." J Biomech Eng **115**: 515-519.

Hsu, Y., J.M. Barry et al. (1984). "Growth control in cultured 3T3 fibroblasts: Neutralization and identification of a growth-inhibitory factor by a monoclonal antibody." Proc Natl Acad Sci USA **81**: 2107-2111.

Hutter, J.L. and J. Bechhoefer (1993). "Calibration of atomic force microscope tips." Rev Sci Instrum **64**(7): 1868-1873.

Lammerding, J., P.C. Schulze et al. (2004). "Lamin A/C deficiency causes defective nuclear mechanics and mechanotransduction." J Clin Invest **113**: 370-378.

Lapshin, R.V. (1995). "Analytical model for the approximation of hysteresis loop and its application to the scanning tunneling microscope." Rev Sci Instrum **66**(9): 4718-4730.

Larson, J.M., S.A. Schwartz et al. (2010). Resonant Scanning in Laser Confocal Microscopy. Microscopy U (online), Nikon Instruments, Inc.

Lévy, R. and M. Maaloum (2002). "Measuring the spring constant of atomic force microscope cantilevers: thermal fluctuations and other methods." Nanotechnology **13**: 33-37.

Liang, H., K.T. Vu et al. (1996). "Wavelength dependence of cell cloning efficiency after optical trapping." Biophys J **70**: 1529-1533.

Lin, A.J., N.L. Slack et al. (2000). "Structure and structure-function studies of lipid/plasmid DNA complexes." J Drug Target **8**(1): 13-27.

Lincoln, B., S. Schinkinger et al. (2007). "Reconfigurable microfluidic integration of a dual-beam laser trap with biomedical applications." Biomed Microdev **9**(5): 703-710.

Litvinov, R.I., H. Shuman et al. "Binding strength and activation state of single fibrinogen-integrin pairs on living cells." Proc Natl Acad Sci USA **99**: 7426-7431.

Mäkynen, A., T. Ruotsalainen, et al. (2003). "CMOS-compatible position-sensitive devices (PSDs) based on photodetector arrays." Sens Actuators A **105**: 261-270.

Malhas, A., C.F. Lee et al. (2007). "Defects in lamin B1 expression or processing affect interphase chromosome position and gene expression." J Cell Biol **176**: 593-603.

Mammen, M., K. Helmerson et al. "Optically controlled collisions of biological objects to evaluate potent polyvalent inhibitors of virus-cell adhesion." Chem Biol **3**: 757-763 (1996).

Meshorer, E. (2008). Imaging chromatin in embryonic stem cells. StemBook (online). Harvard Stem Cell Institute, Cambridge, Massachusetts.

Meyer, G. and N.M. Amer (1990). "Optical-beam-deflection atomic force microscopy: The NaCl (001) Surface." Appl Phys Lett **56**: 2100.

Misteli, T. and D.L. Spector (1997). "Applications of the green fluorescent protein in cell biology and biotechnology." Nat Biotechnol **15**(10): 961-964.

Moheimani, S.O. and Y.K. Yong (2008). "Simultaneous Sensing and Actuation with a Piezoelectric Tube Scanner." Rev Sci Instrum **79**: 073702.

Murphy, D. M. (2001). Confocal Laser Scanning Microscopy. Fundamentals of Light Microscopy and Electronic Imaging, Wiley-Liss.

Nakano, A. (2002). "Spinning-disk Confocal Microscopy- A Cutting Edge Tool for Imaging of Membrane Traffic." Cell Struct Func **27**: 349-355.

Neuman, K.C., E.H. Chadd et al. (1999). "Characterization of photodamage to Escherichia coli in optical traps." Biophys J **77**: 2856-2863.

Neuman, K.C. and A. Nagy (2008). "Single-molecule force spectroscopy: optical tweezers, magnetic tweezers and atomic force microscopy." Nat Methods **5**: 491-505.

Padgett, M. and L. Allen. "The Angular Momentum of Light: Optical Spanners and the Rotational Frequency Shift." Opt Quantum Electron **31**: 1-12.

Pawley, J.B. (2006). Handbook of Biological Confocal Microscopy. Berlin, Springer.

Pelling, A.E., D.W. Dawson et al. (2007). "Distinct contributions of microtubule subtypes to cell membrane shape and stability." Nanomedicine **3**(1), 43-52.

Pelling, A.E., F.S. Veraitch et al. (2009). "Mechanical Dynamics of Single Cells During Early Apoptosis." Cell Motil Cytoskeleton **66**, 409-422.

Prasher, D.C. (1995). "Using GFP to see the light." Trends Genet **11**(8): 320-323.

Prasher, D.C., V.K. Eckenrode et al. (1992). "Primary structure of the Aequorea victoria green-fluorescent protein." Gene **111**(2): 229-233.

Radmacher, M. (2002). "Measuring the Elastic Properties of Living cells by the Atomic Force Microscope." Methods Cell Biol **68**: 67-90.

Radmacher, M., R.W. Tillamnn et al. (1992). "From molecules to cells: imaging soft samples with the atomic force microscope." Science **257**(5078): 1900-1905.

Rittweger, E., K.Y. Han et al. (2009). "STED microscopy reveals crystal colour centres with nanometric Resolution." Nat Photonics **3**(3): 144-147.

Rotsch, C. and M. Radmacher (2000). "Drug-Induced Changes of Cytoskeletal Structure and Mechanics in Fibroblasts: An Atomic Force Microscopy Study." Biophys J **78**(1): 520-535.

Rowat, A.C., J. Lammerding et al. (2006). "Mechanical Properties of the Cell Nucleus and the Effect of Emerin Deficiency. " Biophys J **91**: 4649-4664.

Sader, J.E. (1995). "Parallel beam approximation for V-shaped atomic force microscope cantilevers." Rev Sci Instrum **66**(9): 4583-4587.

Saleh, B.E.A. and M.C. Teich (1991). Fundamentals of Photonics. New York, John Wiley & Sons.

Samson, F., J.A. Donoso et al. (1979). "Nocodazole action on tubulin assembly, axonal ultrastructure and fast axoplasmic transport." J Pharmacol Exp Ther **208**(3): 411-417.

Sanderson, M.J. and I. Parker (2003). "Video-rate confocal microscopy." Methods Enzymol **360**: 447-481.

Sato, M.H., K. Ura et al. (1999). "Atomic force microscopy sees nucleosome positioning and histone H1-induced compaction in reconstituted chromatin." FEBS Lett **452**: 267-271.

Scaffidi, P. and T. Misteli (2006). "Lamin A-dependent nuclear defects in human aging." Science **312**: 1059-1063.

Seol, Y., A.E. Carpenter et al. (2006). "Gold nanoparticles: enhanced optical trapping and sensitivity coupled with significant heating." Opt Lett **31**: 2429-2431.

Simpson, N.B., K. Dholakia et al. (1997). "Mechanical equivalence of spin and orbital angular momentum of light: An optical spanner." Opt Lett **22**(1): 52-54.

Smith, D.P., A. Bryant et al. (1987). "Images of a lipid bilayer at molecular resolution by scanning tunneling microscopy." Proc Natl Acad Sci USA **84**(4): 969-972.

Spring, K.R., M.W. Davidson et al. (2008). Introduction to Fluorescence Microscopy. Microscopy U (online), Nikon Instruments, Inc.

Spring, K.R., T.J. Fellers et al. (2009). Resolution and Contrast in Confocal Microscopy. Theory of Confocal Microscopy, Olympus Corporation.

Svoboda, K., C.F. Schmidt et al. (1993). "Direct observation of kinesin stepping by optical trapping interferometry." Nature **365**: 721-727.

Taylor, G.W., J.J. Gagnepain, T.R. Meeker, T. Nakamura, and L.A. Shuvalov (1985). Piezoelectricity. New York, Gordon and Breach Science Publishers.

Todaro, G.J. and H. Green (1963). "Quantitative studies of the growth of mouse embryo cells in culture and their development into established lines." J Cell Biol **17**: 299-313.

Vasquez, R.J., B. Howell et al. (1997). "Nanomolar concentrations of nocodazole alter microtubule dynamic instability in vivo and in vitro." Mol Biol Cell **8**(6): 973-985.

Wang, Y. and D.E. Discher (2007). Cell Mechanics. Academic Press.

Watanabe-Nakayama, T., S. Machida et al. (2011). "Direct Detection of Cellular Adaptation to Local Cyclic Stretching at the Single Cell Level by Atomic Force Microscopy." Biophys J **100**: 564-572.

Watt, P.C., M.P. Sawicki et al. (1993). "A review of gene transfer techniques." Am J Surg **165**(3): 350-354.

Yahara, I., F. Harada et al. (1982). "Correlation Between Effects of 24 Different Cytochalasins on Cellular Structures and Cellular Events and Those on Actin In Vitro." J Cell Biol **92**(1): 69-78.

Yoshimura, S.H., R.L. Ohniwa et al. (2000). "DNA phase transition promoted by replication initiator." Biochemistry **39**: 9139-9145.

Yuen, F.L., G. Zak et al. (2008). "Morphology of fibroblasts grown on subtrates formed by dielectrophoretically aligned carbon nanotubes." Cytotechnology **56**: 9-17.

Zhong, Q., D. Inniss et al. (1993). "Fractured polymer/silica fiber surface studied by tapping mode atomic force microscopy." Surf Sci Lett **290**: L688-L692.

Zougagh, M. and A. Rios (2009). "Micro-electromechanical sensors in the analytical field." Analyst **134**(7): 1274-1290.

Chapter 3

Experimental Procedures and Analysis

3.1 Cell Culture

NIH3T3 fibroblast cells were cultured in Dulbecco's Modified Eagle's Medium (DMEM) supplemented with 10% heat-inactivated fetal bovine serum (FBS) and 1% penicillin/streptomycin (Hyclone), on 100-mm culture dishes (Corning) at 37°C and 5% CO_2. Cells were passaged twice weekly: they were rinsed using a solution of phosphate-buffer saline (PBS, Fisher Scientific), detached from the dish in which they had been cultured using trypsin-EDTA (Hyclone), isolated via centrifugation, and re-suspended in fresh DMEM.

Long-term storage of cells involved suspension of cells in a solution of FBS supplemented with 10% dimethylsulfoxide (DMSO; Sigma). The cells were then placed in a "Mr. Frosty" container (Nalgene) in a -80°C freezer, maintaining a slow freezing rate of 1°C per hour. The next day the cells were transferred to long term storage in liquid nitrogen at -176°C until needed.

3.2 Immunofluorescence

In order to add fluorescent tags for actin, microtubules and DAPI, cells were submitted to a protocol outlined in previous literature (Pelling, Veraitch et al. 2009). Samples consisted of glass-bottom dishes containing adherent cells that had been passaged at least 24 hours prior, unless stated otherwise; these exceptions are discussed at the end of this section.

Samples were first rinsed with warm PBS, and then incubated with a fixative buffer (2% sucrose and 3.5% paraformaldehyde (Fisher Scientific) in PBS) at 37°C for 2 minutes. This was done in order to kill and fix the cells into place. These samples were then permeabilized for 2 minutes with another buffer, consisting of the following: 20mM HEPES (4-(2-hydroxyethyl)-1-piperazineethanesulfonic acid; Fisher Scientific), 300mM sucrose, 50mM NaCl, 3mM $MgCl_2$, and 198mL distilled water, with 1mL of 10% sodium azide (NaN_3; Fisher Scientific) and 1mL of Triton X-100 (Fisher Scientific) dissolved in the buffer for a final concentration of 0.5%.

Each sample was then stained for actin by gently adding a 200µL solution containing 4µL phalloidin AlexaFluor-546 (Invitrogen) in wash buffer (20mL FBS (Hyclone) and 2mL of 10% sodium azide dissolved in 400mL of PBS). Samples were then incubated in the dark for 20 minutes, preceding a second 15-minute incubation with pure wash buffer.

Samples were then stained for tubulin (MTs) on ice: a 200µL solution of 1µL monoclonal mouse α-tubulin primary antibody (Abcam) dissolved in cold wash buffer was prepared for each sample to be stained. After rinsing with pure cold wash buffer, samples were incubated with the antibody solution for 15 minutes in the dark. After another rinse with cold wash buffer, they were incubated for an additional 15 minutes in the dark with a 200µL solution containing 1µL of rabbit anti-mouse secondary antibody conjugated to AlexaFluor 488 (Invitrogen) in cold wash buffer. A third, 15-minute incubation with pure cold wash buffer completed this step.

Cell nuclei were then labeled using a 200µL solution of 0.4µL DAPI (Invitrogen) in cold PBS for each sample. Samples were incubated with this dye for 10 minutes on ice, in the dark, and then rinsed with cold PBS.

The last step was mounting: 30µL of DABCO anti-fade reagent (Sigma) was added to the center of each sample dish. A glass coverslip was gently lowered onto the surface of the cells and sealed in place using clear nail polish. Cells were stored in a refrigerator at 4°C until they were ready to be imaged.

In some cases, variations of the protocol above were implemented in order to accommodate the needs of the experiment. For example, cells that had been previously transfected with vimentin-GFP in order to visualize vimentin intermediate filaments (discussed in the following section) could not be simultaneously stained for microtubules using the reagents above. Instead, these cells were stained for only actin and DAPI. In addition, cells that had not quite adhered to the surface of the dish – specifically, those that were fixed less than an hour after passaging and were still round in shape – ran a high risk of being detached from the dish due to the frequent rinsing. As such, for each plate containing these cells the 200µL solutions of phalloidin, α-tubulin primary antibody, rabbit anti-mouse secondary antibody and DAPI were added simultaneously. A 30-minute incubation period in the dark, on ice was followed by a single wash with cold PBS, before mounting as usual.

3.3 Transfection

Transfections were performed 12 hours after cell passage and 24 hours prior to actin-DAPI staining (see Section 3.2). GFP-vimentin DNA plasmids (Martys, Ho et al. 1999) were a kind gift from Robert Goldman of Northwestern University. Transfections with these plasmids were carried out using the liposome method discussed in Section 2.3.2.

For each dish of cells that would be stained for actin and DAPI, a solution containing 46μL of DMEM and 4 μL of Lipofectamine 2000 reagent (Invitrogen) was prepared. In addition, a separate 50μL-solution containing 1μg of GFP-vimentin plasmid DNA in DMEM was also prepared. After a five-minute period to allow equilibration, these two solutions were combined. The resulting 100μL-solution was then allowed to sit at room temperature for at least 25 minutes, before it was added directly to the dish of cells containing DMEM. Cells from dishes prepared in this manner were fixed stained within 48 hours according to the procedure outlined in Section 3.2.

3.4 Drug Treatments

In order to study the influence of the CSK on nuclear deformation, cells were treated with either Cytochalasin-D (CytD; 10 μM in DMSO; Sigma) or nocodazole (10 μM in DMSO; Sigma) to specifically depolymerize actin or tubulin, respectively (Rotsch & Radmacher 2000; Pelling, Dawson et al. 2007). Double-drug experiments, in which the cells were treated with both of these drugs simultaneously, were also performed.

Appropriate amounts of each drug were directly added to the culture media 15 minutes prior to the experiment or, in case of staining, 15 minutes prior to fixing. For double-drug experiments, equal amounts of Cyt-D and nocodazole were introduced to the same culture dish simultaneously.

3.5 Simultaneous AFM and Confocal Microscopy

3.5.1 Sample Preparation

After passaging, 3T3 fibroblast cells to be used in AFM-LSCM experiments were seeded at the desired concentrations onto 35-mm glass-bottomed tissue culture dishes (MatTek) containing 2 mL of DMEM each. They were then left to adhere and settle for at least 12 hours. An hour prior to experimentation, nuclei of live cells were stained with Hoechst 33342 (Invitrogen) according to manufacturer protocols.

3.5.2 Experimental Setup

Atomic Force Microscopy (AFM) and high-speed Laser Scanning Confocal Microscopy (LSCM) were performed simultaneously by mounting the AFM (NanoWizard II, JPK Instruments AG, Berlin, Germany) onto a Nikon TiE inverted microscope with a resonant scanner A1R confocal. A 60X/NA1.2 water immersion objective was used for all experiments, and the culture dish was kept at 37°C with a temperature-controlled stage.

All AFM cantilevers were Veeco MSCT-AUHW probes, pyramidal in shape with an opening angle of 35°. The spring constant was determined by the thermal resonance method (discussed in Section 2.1.1.2), and had an experimentally determined value of $k = 0.06 \pm 0.01$ N/m.

3.5.3 Static (single-push) force application

Static long-term nuclear deformation was recorded by performing simultaneous AFM and 4D LSCM. The AFM cantilever was aligned over the center of the nucleus of an adherent, well-spread fibroblast cell. The tip was then extended (as seen in Figure 3.1a) in order to apply a constant force of 0, 10 or 20nN for 15 minutes while the structural deformation of the nucleus was recorded in 3D LSCM image volumes. Image volumes of the nucleus were recorded one minute before the application of force and once every minute for 15 minutes thereafter.

Tracking static short-term nuclear deformation entailed capturing images in a single plane (x-y) set in the middle of the nucleus at a rate of 8 frames per second. Images were recorded through 5.0 seconds of constant force application, as well as 2.5 seconds before

extension of the AFM tip as control. During imaging, the AFM cantilever was brought into contact with the cell surface, above the center of the nucleus, and a constant force was applied for 5.0 seconds, followed by retraction of the tip.

3.5.4 Cyclic force application

Cycling experiments were conducted by bringing the cantilever down onto the cell surface, applying constant force for 5 seconds, and retracting the tip for 10 seconds. These steps were repeated for 15 cycles, all throughout which images were being captured at the same rate mentioned above.

In both static (whether long-term or short-term) and cycling experiments, cells were separately imaged in the absence of force – that is, with the AFM tip completely retracted – as control.

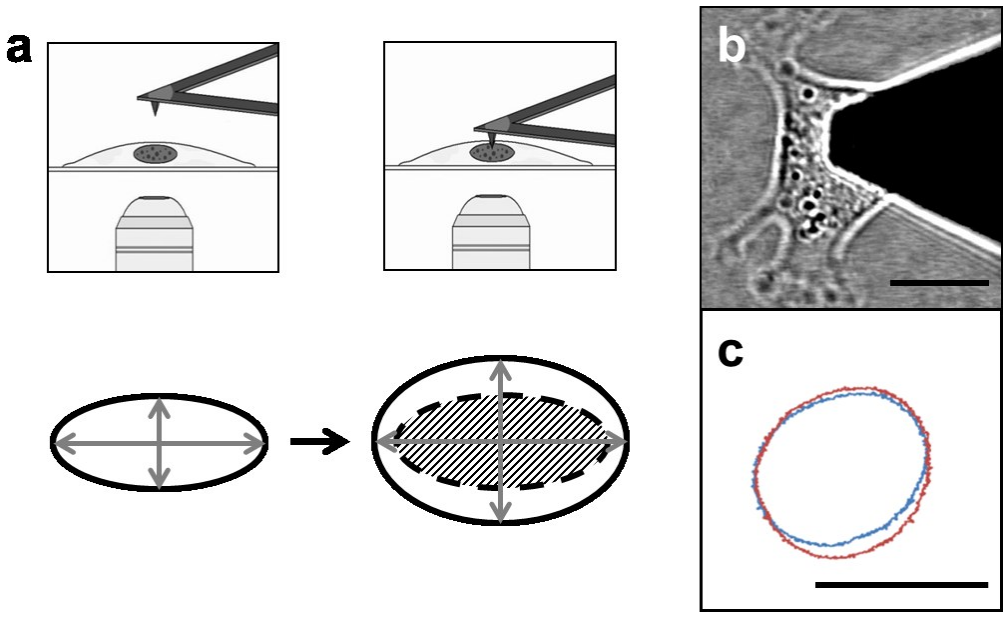

Figure 3.1. Schematic representation of the AFM-LSCM experiment, and how deformation is quantified. (a) The (projected) area of the nucleus prior to force application (AFM tip retracted) is set to 1.0. Throughout the duration of the force application (AFM tip extended), all measured projected areas are normalized with respect to the initial value (shaded region; see Section 3.5.5 for a detailed explanation). Longitudinal and transverse strains are calculated by comparing measurements of the lengths of the major and minor axis, respectively, against their initial values. Phase images of the cell and AFM tip (b) are separated from images of Hoechst-stained nuclei prior to image processing. (c) Post-image processing: superimposed outlines of the nucleus immediately before (blue) and 15 minutes after (red) initial force application are shown. All scale bars 12μm.

3.5.5 Image Analysis

Upon completion of the AFM-LSCM experiments, raw image data were analyzed using open-source image-processing software called ImageJ (Abramoff, Magalhaes et al. 2004) in order to quantify the deformation of the nucleus. We designed an image-processing algorithm using a custom macro built in the software's programming environment (shown in Figure 3.2b, and provided in Appendix A). Here, 4D and 3D image data obtained from LSCM are treated as hyperstacks. Fluorescent images that showed only the Hoechst-stained nuclei and phase images showing the cell body along with the AFM tip are separated prior to image processing.

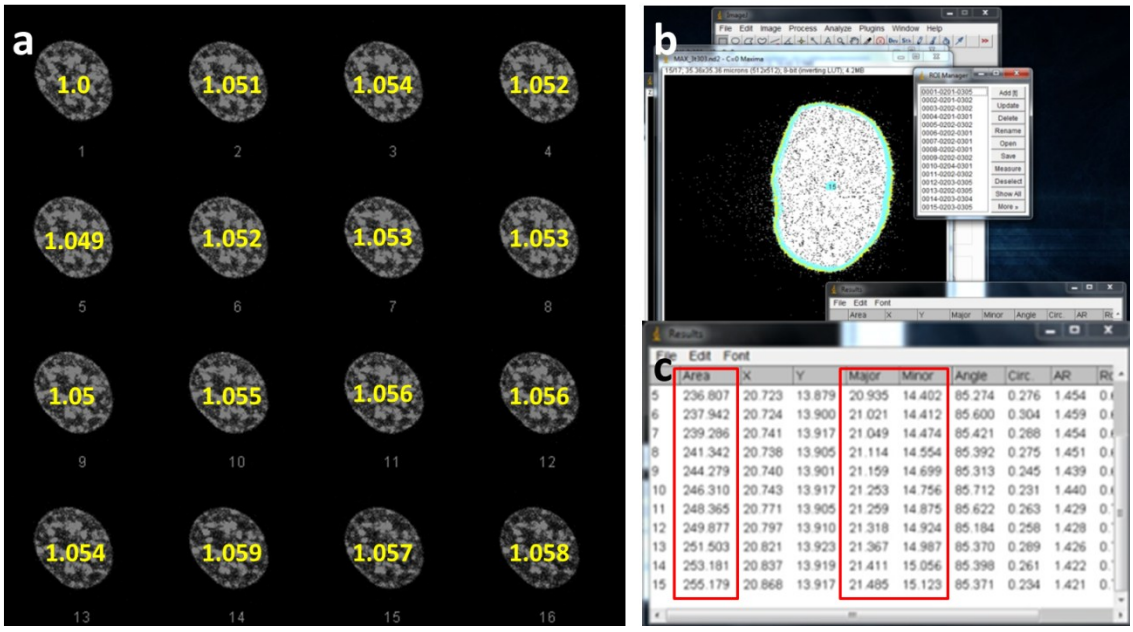

Figure 3.2. Quantifying AFM-induced nuclear deformation with ImageJ. (a) A montage of the maximum intensity projections of 3D image volumes for a nucleus indented with 10nN of force from a single static long-term AFM-LSCM experiment is shown. Here, t=1 (time points are indicated underneath the images) corresponds to the time frame immediately before AFM tip extension, with a normalized area (shown in yellow over the image) of 1.0. Successive images correspond to those taken every minute after tip extension, and show the projected normalized area of the nucleus expanding by approximately 5-6%. The ImageJ user interface includes (b) a window recording the thresholded images and outlines of the nuclei, as well as (c) a table of all measurements performed on these images. Most of these were performed using the custom macro (shown running in the figure; also, provided in Appendix A) developed in order to automate measurements for data from short-term deformation experiments containing a large number of time frames. Boxed in red are the columns containing measurements used to quantify deformation: the measured area, as well as the lengths of the major and minor axes of the ellipse of best fit.

For long-term (single-push) deformation, three-dimensional image volumes of a whole, single nucleus were tracked for the 16-minute duration of each experiment. They were then collapsed into 2D maximum intensity projections for each of the 16 time frames (as seen in Figure 3.2a). Each resulting image, a projection of the nucleus onto the xy-plane, was then converted into a corresponding binary mask (shown in Figure 3.2b), which allowed the border of the nucleus to be traced and selected automatically; the area of this selection (in μm^2) was then measured. Simultaneously, each selection was fitted to an ellipse, from which we obtained the lengths of the major and minor axes. These measurements were obtained for each timeframe, allowing us to track how these quantities of interest, shown schematically in Figure 3.1a, changed over the duration of the experiment.

The method for processing short-term (single-push) and cyclic deformation was very similar to the one above. Instead of three-dimensional volumes, however, raw image data for these experiments involved two-dimensional planes taken from the center of the nucleus, eliminating the need to obtain maximum intensity projections.

3.6 Optical Stretcher

3.6.1 Sample Preparation

An hour prior to experimentation, nuclei of 3T3 fibroblast cells to be used in optical stretching experiments were stained with Hoechst 33342 according to manufacturer protocols. Immediately before the experiment, cells were then passaged as usual (see Section 3.1) until the centrifugation step. They were then isolated and re-suspended vigorously in fresh culture media, after which 1mL of this cell suspension was extracted into a 5mL plastic syringe.

3.6.2 Experimental Setup

As discussed in Section 2.2.2, the optical stretcher requires two axially-aligned, counter-propagating laser beams forming a two-beam optical trap. Specifically, my setup was built around a CW (continuous wave) Yb Fiber Laser Module (YLM-5-1070, IPG Photonics) at a wavelength of 1070 nm, with a maximum output power of 5W. Built into the module was a

50/50 beam splitter, and the laser was coupled into two single-mode optical fibers, each capable of delivering up to 2.5W of power. The bare ends of the fibers were stripped, cleaved, and aligned carefully onto a glass centerpiece using a glass capillary as a temporary backstop, inspired by previous techniques (Constable, Kim et al. 1993; Guck, Ananthakrishnan et al. 2002). This was done so that the fibers were collinear and facing one another, with a gap of approximately 240µm between them.

In order to facilitate trapping and stretching of cells within the optical stretcher, I made use of a flow chamber geometry outlined in previous literature (Guck, Ananthakrishnan et al. 2001; Guck, Schinkinger et al. 2005). A square glass capillary (inner diameter 80µm; wall thickness 40µm) was placed along the gap between the fibers. The ends of the capillary were coupled to PEEK (polyetheretherketone) tubing, allowing for the streaming of a cell suspension directly through the capillary. One end of the PEEK tubing was connected to the syringe with cells suspended in DMEM, while the other led to a reservoir of pure DMEM. This arrangement enabled manual flow control of the solution in both directions.

The glass centerpiece holding the fibers and capillary was then mounted onto a customized stage on an inverted microscope (Nikon TiE) equipped for both phase contrast and fluorescence microscopy. The area on the surface containing the ends of the fibers and the length of the capillary directly above the microscope objective was then covered with immersion oil (Nikon) with n = 1.51 to match that of crown glass (n_{glass} = 1.50-1.52). Lastly, a glass coverslip (Fisher Scientific) was placed on top, sealing the immersion oil and protecting the fiber ends from dust and debris.

3.6.3 Stretching experiments

The analog voltage control and reference signal of the laser were connected to a data acquisition device (NI-USB-6229, National Instruments). This allowed for complete and precise user control of the laser's output power on a computer using custom-built software programmed in LabVIEW (National Instruments; see Appendix C). Calibration data was obtained using a laser power meter and is provided in Figure 3.3 below. Images of the cell suspended within the trap were recorded at 15 frames per second and displayed on the same interface.

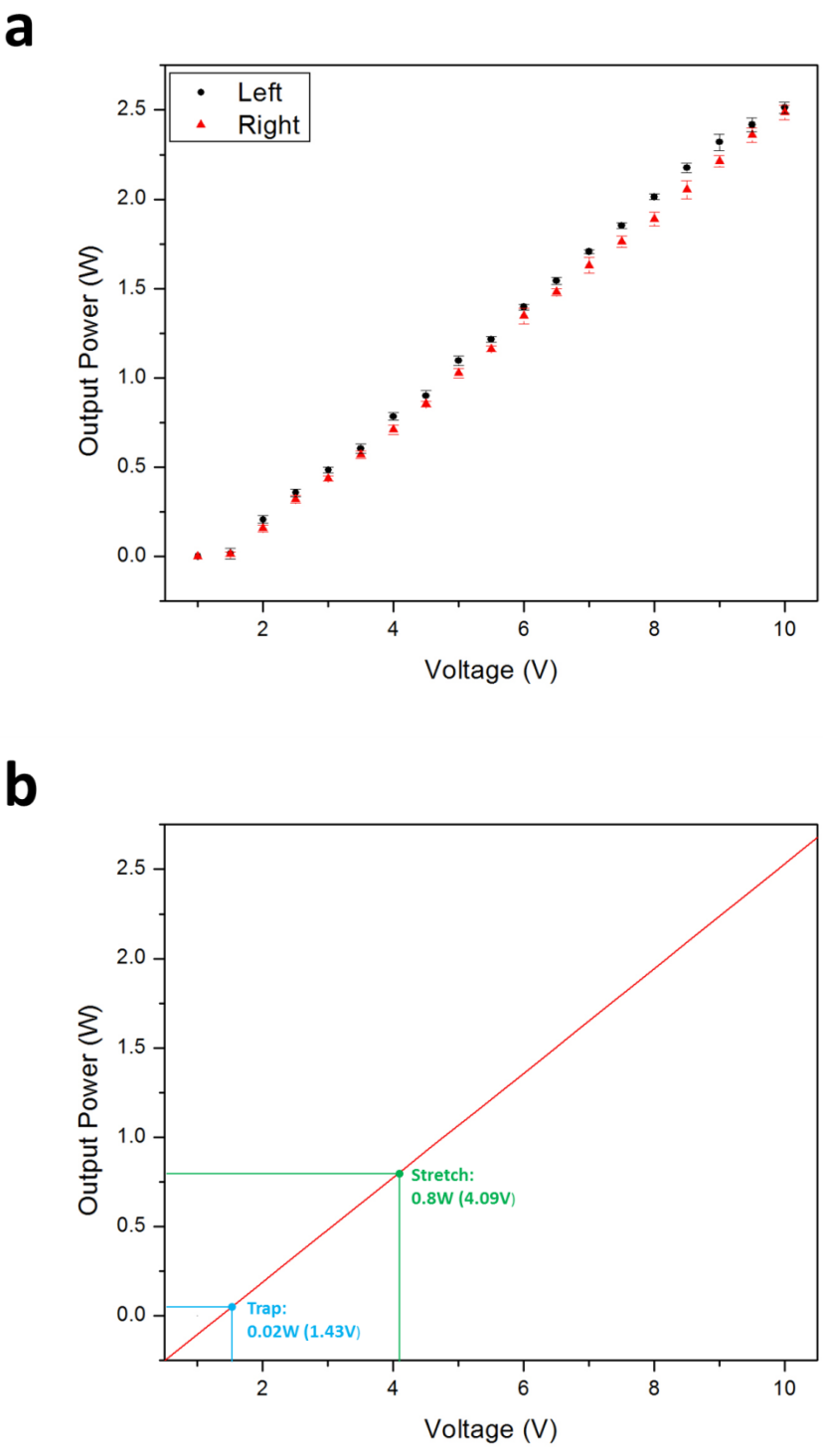

Figure 3.4. Laser calibration data for the optical stretcher. (a) Output power vs. voltage plots for each of the optical fibers. The relationship is linear and almost identical within the range of powers used for stretching experiments. (b) The linear fit of the average curves is shown in red, as well as the voltages used for trapping (P = 20mW) and stretching (P=800mW).

Optical stretching experiments were performed such that they were as similar to the static short-term AFM-LSCM experiments as possible (see Section 3.5.3). Although experiments were performed in which a cyclic force was applied with the AFM (discussed in Section 3.5.4), I did not conduct any corresponding cyclic optical stretching experiments. Dual-beam optical traps are known to cause a significant temperature increase in the cell at the center of the trap as an unwanted side-effect (Guck, Ananthakrishnan et al. 2001; Wetzel, Rönicke et al. 2011). This temperature increase is almost instantaneous, with 1W of laser power corresponding to an increase of 21 ± 2 °C after only 0.5 s (Wetzel, Rönicke et al. 2011).

Multiple studies employing the optical stretcher have shown that cells are viable even under these conditions (Guck, Ananthakrishnan et al. 1999; Guck, Ananthakrishnan et al. 2001; Schinkinger, Wottawah et al. 2004; Guck, Schinkinger et al. 2005; Ananthakrishnan, Guck et al. 2006), but only for short periods of time (~5 seconds). Cell spreading experiments, in which the ability of a cell to spread in a certain time frame is correlated to its viability, were performed in a recent study on NIH3T3 fibroblasts. These cells were initially kept at 37°C, and then subsequently exposed to heat shocks of varying temperatures and durations within the optical stretcher (Wetzel, Rönicke et al. 2011). While 60% of the cells that had been subjected to 5-second heat shocks of 48°C (corresponding to a stretching power of 1.0 W) were still found to be viable, this number dropped sharply to less than 20% for 48°C heat shocks of 10 seconds (Wetzel, Rönicke et al. 2011). Given these results, cyclic optical stretching experiments with 5-second stretching periods, analogous to the cyclic AFM/LSCM experiments, are clearly not feasible.

Stretching experiments began with streaming the cell suspension through the capillary. Once a target cell became visible in the field of view between the laser fibers, flow was stopped and the laser power was increased from zero to the set trapping power (20 mW). Once the cell had been trapped for 2.5 seconds, the laser was set to the stretching power (800 mW; all laser powers were defined according to standards set by Guck, Ananthakrishnan et al. 2001) for 5.0 seconds. The laser power was then reduced to 20 mW (trapping power) for an additional 2.5 seconds, before finally being set to zero once more. Flow was resumed until the next target cell was spotted, after which the above procedure was repeated.

3.6.4 Image Analysis

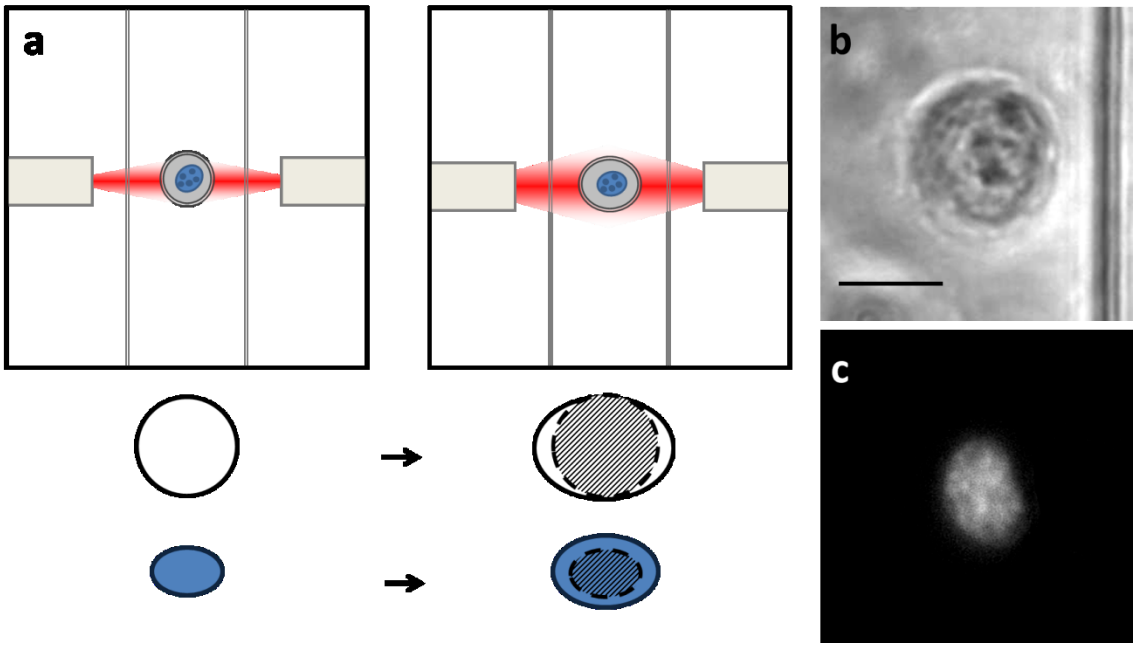

Figure 3.4. Schematic representation of the optical stretching experiment, and how deformation is quantified. (a) The projected area of either the cell membrane or the nucleus prior to stretching (trap power in effect) is set to 1. Throughout the duration of the force application (stretching power in effect), all measured projected areas are normalized with respect to the initial value (shaded region). Phase images of the cell (b) and fluorescence images of Hoechst-stained nuclei (c) are taken in order to compare the deformation of the nucleus to that of the cell as a whole, in response to stretching forces generated in the optical stretcher. Scale bar 10μm.

For experiments with the optical stretcher, the same protocol and ImageJ macro from the AFM-LSCM experiments (discussed in Section 3.5.5) were used to analyze the change in normalized area for both fluorescence images (of nuclei) and phase-contrast images (of whole cell membranes). In the case of the latter, though, additional steps were taken to improve contrast prior to image processing. However, the stretching force within the optical stretcher was not applied normal to the x-y plane, as in AFM-LSCM experiments, but rather along this plane. Thus, it became more meaningful to define the strain along the directions parallel and perpendicular to the beam axis, as opposed to comparing the strain along the major and minor axes of the cells/nuclei.

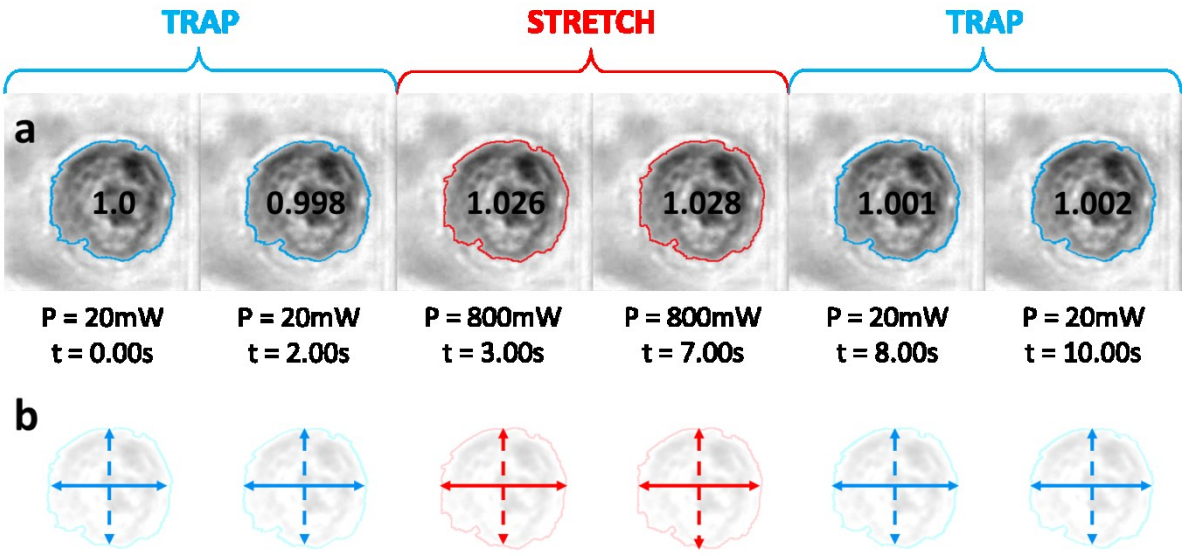

Figure 3.5. Quantifying stretching-induced deformation with ImageJ. A series of phase images displaying one whole 3T3 cell at selected time points during a single optical stretching experiment is shown. Time points and laser powers used are indicated underneath the images. (a) Outlines of the cell are also shown, with normalized area indicated (area at t=0.00 corresponding to 1.0) over each image. Results from this particular experiment show the projected normalized area of the cell expanding by approximately 3% throughout stretching, returning to roughly its original value within 0.5 s of power reduction. (b) After image processing, cell lengths were measured in ImageJ along the direction parallel to the beam axis (solid) and the direction perpendicular to the beam axis (dashed), in order to quantify the strain along these axes.

3.7 References

Abramoff, M.D., P.J. Magalhaes et al. (2004). "Image processing with ImageJ." Biophotonics International **11**(7): 36-42.

Constable, A., J. Kim et al. (1993). "Demonstration of a fiber-optical light-force trap." Opt Lett **18**: 1867-1869.

Guck, J., R. Ananthakrishnan et al. (1999). "Optical Deformability of Soft Biological Dielectrics." Phys Rev Lett **84**(23): 5451-5454.

Guck, J., R. Ananthakrishnan et al (2001). "The Optical Stretcher: A Novel Laser Tool to Micromanipulate Cells." Biophys J **81**:767-784.

Guck, J., R. Ananthakrishnan et al. (2002). "Stretching biological cells with light." J Phys Condens Matter **14**: 4843-4856.

Guck, J. S. Schinkinger et al. (2005). "Optical Deformability as an Inherent Cell Marker for Testing Malignant Transformation and Metastatic Competence." Biophys J **88**:3689-3698.

Martys, J.L., C. Ho et al. (1999). "Intermediate Filaments in Motion: Observations of Intermediate Filaments in Cells Using Green Fluorescent Protein-Vimentin." Mol Biol Cell **10**(5): 1289-1295.

Pelling, A.E., D.W. Dawson et al. (2007). "Distinct contributions of microtubule subtypes to cell membrane shape and stability." Nanomedicine **3**(1): 43-52.

Pelling, A. E., F. S. Veraitch, et al. (2009). "Mechanical dynamics of single cells during early apoptosis." Cell Motil Cytoskeleton **66**(7): 409-422.

Rotsch, C. and M. Radmacher (2000). "Drug-Induced Changes of Cytoskeletal Structure and Mechanics in Fibroblasts: An Atomic Force Microscopy Study." Biophys J **78**(1): 520-535.

Schinkinger, S., F. Wottawah et al. (2004). "Feeling for cells with light." Proc SPIE Int Soc Opt Eng **5514**: 170-178.

Wetzel, F., S. Rönicke et al. (2011). "Single cell viability and impact of heating by laser absorption." Eur Biophys J **40**: 1109–1114.

Chapter 4

Nuclear Deformation under Static Force Application

In this chapter I investigated the mechanical response of the nucleus when an external force is applied onto an individual NIH3T3 fibroblast. The results in Section 4.1 show that when a 10 nN or 20 nN force from the AFM is applied onto the center of the nucleus of an adherent cell, the nucleus expands in the plane perpendicular to the force application. In addition, results in Section 4.2.1 show that most of this deformation actually takes place within the first few seconds of force application. Remarkably, this expansion is not isotropic: the deformation along the minor (short) axis of the nucleus is significantly larger than that along its major (long) axis.

However, optical stretcher experiments performed on suspended 3T3 cells yielded no significant change in nuclear size or shape, although the cell membrane itself deformed significantly (Section 4.2.2). It is important to note that in the optical stretcher, the stretching force is three orders of magnitude smaller than the force applied by the AFM tip. In addition, Section 4.3 shows that the morphology of the cytoskeleton varies significantly between adherent cells (used in the AFM/LSCM experiments) and suspended cells (used in the optical stretching experiments). Taken together, these results indicate that the mechanical response of the nucleus depends significantly on the magnitude of the applied force, as well as the state of the cytoskeleton.

4.1 Nuclear Deformation over Long Timescales

Force-induced nuclear deformation was observed by performing simultaneous AFM and LSCM, in which the cantilever of the AFM was aligned over the center of the nucleus and then lowered to apply a constant force (shown schematically in Fig. 3.1a). Simultaneously, confocal image volumes were acquired once per minute throughout the entire duration of the constant force application. These confocal data stacks were then Z-projected for further analysis.

In this first series of experiments, I observed the deformation of nuclei subjected to a constant force for 15 minutes. The nuclei examined in this study were generally elliptical, and I characterized the normalized projected area and the strain (ε) along the major and minor axes of the nucleus as a function of time.

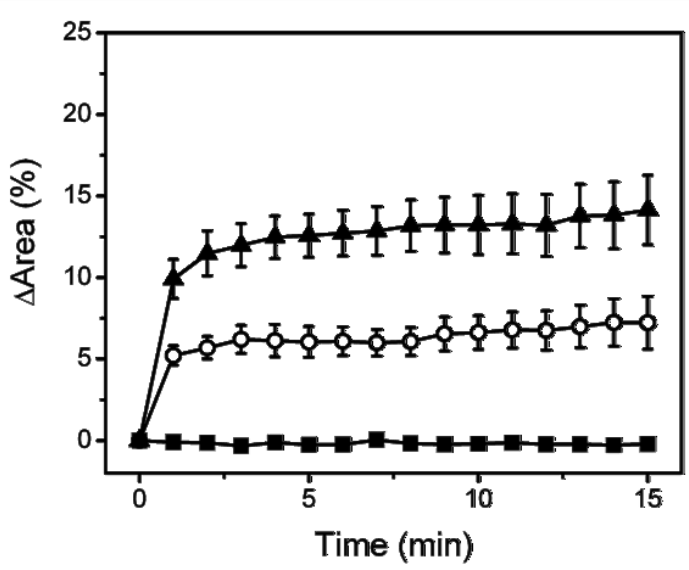

Figure 4.1. Nuclei observed under long-term deformation (1). The change in normalized area is plotted against time for an applied force of 0nN (filled squares, n=3), 10nN (empty circles, n=12) and 20nN (filled triangles, n=12). Error bars in this and all succeeding plots correspond to standard error of the mean (SEM; see Appendix D for further details).

Upon application of force, the projected area increased rapidly within the first minute of force application, reaching 90-95% of its final value after a subsequent 14 minutes of constant force application (Fig. 4.1). There was also a clear dependence on applied force ($p < 0.001$): at the 15-minute time point, the projected area increased by 7 ± 2% and 14 ± 2% for a 10nN and 20nN constant applied force, respectively. No significant change in projected area was observed in the absence of applied force (0nN).

Interestingly, the change in shape was not isotropic along the major and minor axes of the nucleus. The absolute deformation along the major axis was about one third of the absolute deformation along the minor axis. In Fig. 4.2, I plot the force dependent strain, ε_{major} and ε_{minor}, as a function of time. After 15 minutes of constant force application, the final strain was largest for cells exposed to 20nN (ε_{major} = 3 ± 1% and ε_{minor} = 11 ± 2%), followed by 10nN (ε_{major} = 2 ± 1% and ε_{minor} = 6 ± 1%, respectively). Control cells (0nN) displayed no significant changes in strain along either axis.

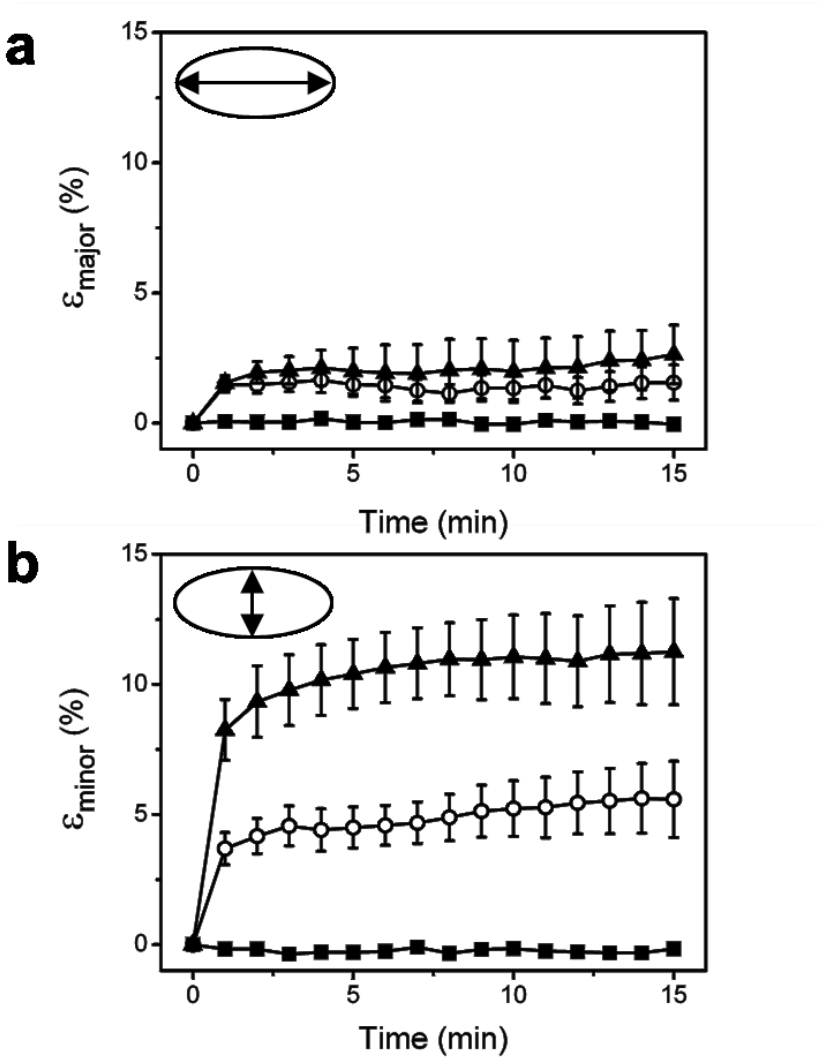

Figure 4.2. Nuclei observed under long-term deformation (2). Strain along (a) the major axis and (b) the minor axis is plotted against time for an applied force of 0nN (filled squares, n=3), 10nN (empty circles, n=12) and 20nN (filled triangles, n=12). It is immediately apparent that the magnitude of strain along the minor axis is greater than that along the major axis, for both 10nN and 20nN of applied force.

As the deformation along the minor axis was consistently greater than that along the major axis, the nuclear shape can be described as becoming less elliptical, or more circular. To quantify this, we defined the ellipticity (χ) of the nucleus as

$$\chi = \arctan(\rho) \quad [35]$$

where ρ is the ratio of the lengths of the major and minor nuclear axes:

$$\rho = \frac{L_{\text{major}}}{L_{\text{minor}}} \quad [36]$$

Therefore, χ = 45° for a perfect circle, and as an object becomes more elliptical χ increases and approaches 90°.

After application of a constant force for 15 minutes, χ decreased by an average of ~2°, indicating that the nucleus had become more circular. Specifically, χ decreased from 54° ± 1° (0nN) to 52° ± 1° (10nN) and from 55° ± 1° (0nN) to 53° ± 1° (20nN) ($p < 0.05$ in both cases; paired t-test). Although the decrease in the value of χ in response to force was significant, the magnitude of χ itself was not dependent on the applied force ($p > 0.4$). The data demonstrates that while the absolute deformation – the change in area and the change in the length of the major and minor axes – of the nucleus is larger with increasing loads, nuclear shape change is conserved.

The results indicate that the change in ellipticity is caused by the fact that ε_{minor} is generally about four times greater than ε_{major}. In Fig. 4.2, it can be readily observed that the strain is always greater along the minor axis of the nucleus. I then chose to quantify the anisotropy of nuclear deformation by means of a dimensionless ratio (α), defined as

$$\alpha = \frac{\varepsilon_{\text{major}}}{\varepsilon_{\text{minor}}} \quad [37]$$

at a given time point. Small values of α imply a large deformation anisotropy ($\varepsilon_{minor} > \varepsilon_{major}$) and α = 1 represents isotropic deformation ($\varepsilon_{minor} = \varepsilon_{major}$). After 15 minutes, α = 0.3 ± 0.1 for 10nN and 20nN of applied force ($p > 0.9$).

Taken together, these results demonstrate that the nucleus can rapidly deform in response to applied nanonewton forces, reaching 90-95% of the final value of the change in projected area, ε_{major} and ε_{minor} at 15 minutes, after only 1 minute of force application. This observed rapid response of the nucleus motivated the following series of experiments, which were designed to study the deformation of the nucleus on a millisecond timescale.

4.2 Nuclear Deformation over Short Timescales

4.2.1 AFM-LSCM Experiments

To increase the temporal resolution of the measurement, I collected images of the nucleus at a rate of 8 frames per second at a single confocal plane. I set the confocal acquisition plane in the middle of the nucleus, which is the region of greatest fluorescence intensity, and used this as the baseline for all subsequent measurements (see Fig. 4.3a, b).

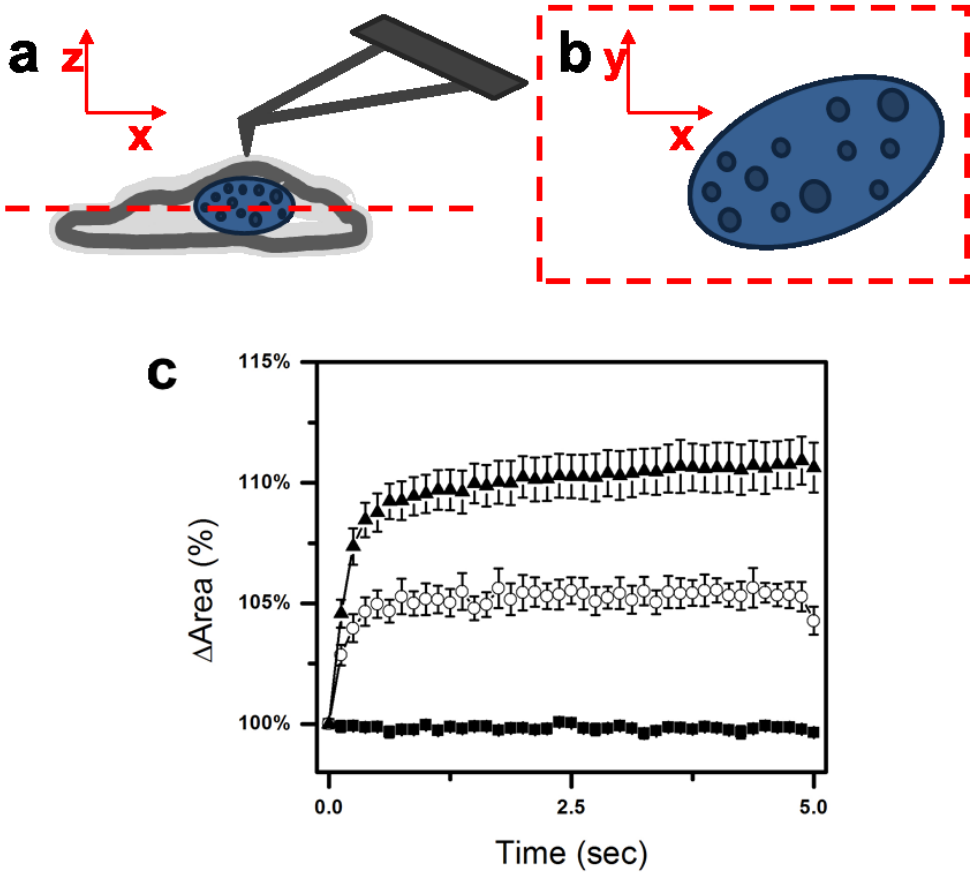

Figure 4.3. Nuclei observed under short-term deformation (1). (a) For this series of experiments, I looked at a single imaging plane in the center of the nucleus (b), as opposed to projecting image volumes as in Section 4.1. (c) The change in normalized area is plotted against time for an applied force of 0nN (filled squares, n=5), 10nN (empty circles, n=10) and 20nN (filled triangles, n=10).

In order to avoid any artifacts due to focal drift, I acquired data for only 5 seconds after force application. It was observed that this time span was more than adequate to capture the deformation of the nucleus up to 90-95% of its final value observed after 15 minutes of force application. The data, shown in Fig. 4.3c-4.4, is also consistent with the previous results shown in Fig. 4.1-4.2.

After 5 seconds of constant force application, the area of the nucleus taken within the confocal plane increased by 5.2 ± 0.6% and 10 ± 1% for an applied force of 10nN and 20nN, respectively. As in the long-term deformation experiment, no significant change in this area was observed in the absence of applied force (0nN), as shown in Fig. 4.3c. Once again, deformation along the minor axis was larger than along the major axis; this is shown more clearly by the plots of strain versus time in Fig. 4.4. To further quantify this, we again measured the change in ellipticity χ of the nucleus, defined in equation 35, after constant force application. After 5 seconds, χ decreased from 52° ± 1° (0nN) to 51° ± 1° for both 10 and 20nN of applied force. This indicated that the nucleus became more circular after force application. The decrease in χ was statistically significant ($p < 0.01$ in both cases; paired t-test), but χ itself was found once again not to be dependent on the magnitude of the applied force ($p > 0.6$).

The final strain measured in nuclei under 5 seconds of constant force application was largest for magnitudes of 20nN (ε_{major} = 2.6 ± 0.4% and ε_{minor} = 7.6 ± 0.8 %), followed by 10nN (ε_{major} = 1.3 ± 0.2 % and ε_{minor} = 3.9 ± 0.4%, respectively). Again, control cells (0nN) displayed no significant changes in strain along either axis, as shown in Fig. 4.4.

Using these values of ε_{major} and ε_{minor}, I was able to calculate the anisotropy parameter α (from equation 37) for each force. After 5 seconds, α = 0.4 ± 0.1 for both 10nN and 20nN of applied force ($p > 0.2$). These values of $\alpha < 1$, in addition to the negative change in χ reported earlier ($\Delta\chi < 0$) indicate that the nucleus expands anisotropically throughout the 5 seconds of force application. This is very consistent with the results obtained from observations of nuclear deformation under a 15-minute constant force application. All values of $\Delta\chi$, ε_{major}, ε_{minor} and α, calculated for both long-term and short-term deformation, are listed in Table 4.1.

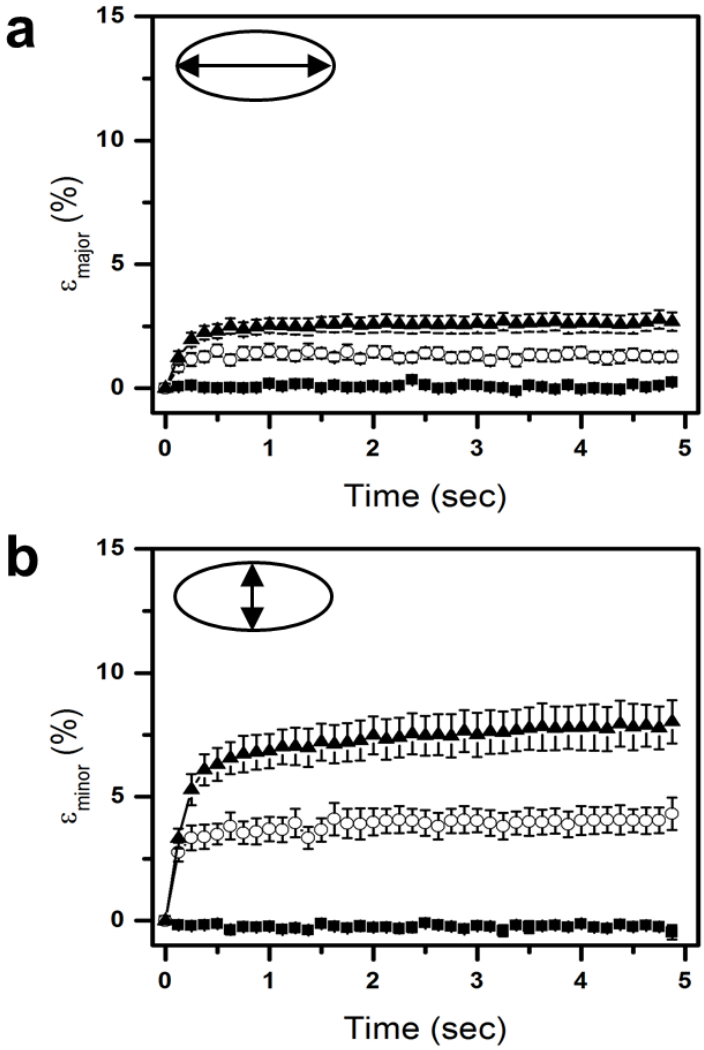

Figure 4.4. Nuclei observed under short-term deformation (2). Strain along (a) the major axis and (b) the minor axis is plotted against time for a constant force of 0nN (filled squares, n=3), 10nN (empty circles, n=12) and 20nN (filled triangles, n=12) applied for 5 seconds. As in the long-term strain plots, the minor axis strain is greater than major axis strain for both 10nN and 20nN of applied force.

Table 4.1: Summary of Parameters Indicating Anisotropy in Nuclear Deformation

Timescale	$\Delta\chi$		ε_{major} (%)		ε_{minor} (%)		α
	(10nN)	(20nN)	(10nN)	(20nN)	(10nN)	(20nN)	
Long (15 min)	-2°	-2°	2±1	3±1	6±1	11±2	0.3±0.1
Short (5 sec)	-1°	-1°	1.3±0.2	2.6±0.4	3.9±0.4	7.6±0.8	0.4±0.1

For both timescales, and for either magnitude of applied force, $\Delta\chi$ is negative, corresponding to a decrease in ellipticity of the nucleus. Strain along the major axis, ε_{major}, is also consistently smaller than strain along the minor axis, ε_{minor}, from which it follows that α is always less than 1. All of these values indicate a clear anisotropy in the expansion of the nucleus in response to constant force. Specifically, this mechanical anisotropy was observed in the deformation of the nucleus along the XY-plane, from a force directly exerted by the AFM tip extending along the Z-axis, onto the surface of the cell.

4.2.2 Optical Stretcher Experiments

In parallel with the AFM-LSCM experiments described above, I also performed stretching experiments with 3T3 cells in the optical stretcher. Single cells suspended in culture media were streamed through a flow chamber and individually subjected to a constant stretching force in a double-beam optical trap for 5 seconds. Phase-contrast images were initially taken of whole cells being stretched in order to verify that the device was effective. Afterwards, fluorescence images were then acquired showing the nuclei of cells being stretched. Both of these data sets were processed in order to quantify whole cell (membrane) and nuclear deformation within the optical stretcher.

As discussed in Section 3.6.4, deformation of nuclei and whole cell membranes from stretching experiments were measured in terms of the change in normalized area, as well as the strain along the axes parallel to and perpendicular to the beam axis. However, as seen in Figure 4.5, stretching experiments yielded no significant nuclear deformation at any point throughout the 5 seconds of force application (0 ± 0.5% change in normalized area). Since there was no detectable change in nuclear shape throughout either trapping or stretching, I did not measure or analyze any strain dynamics for the nucleus.

In contrast, a significant amount of deformation was exhibited by the cell membrane. The projected area of the membrane increased by an average of 2.4 ± 0.2% as the cell was being stretched (Fig. 4.5). Membrane deformation was also characterized by an average strain of 3.3 ± 0.1% in the direction parallel to the beam axis, and an average strain of -1.17 ± 0.1% in the perpendicular direction. Strain data for the cell membrane along both axes are shown together in Figure 4.6.

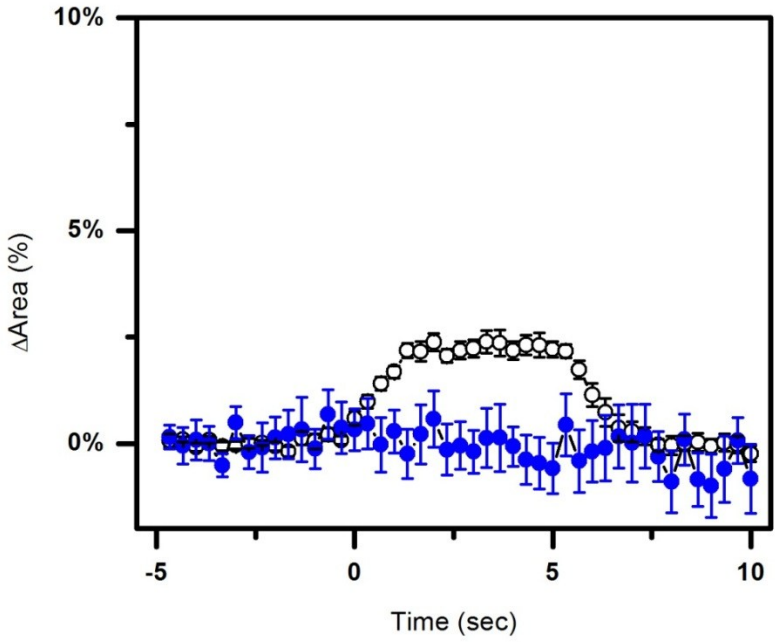

Figure 4.5. Change in normalized area for whole cells and nuclei observed in the optical stretcher. The change in normalized area is plotted against time for whole cells (open circles, white, n=11), and nuclei (filled circles, blue, n=10). From t = -5 sec to t = 0 the lasers are set to a constant trapping power of 20mW. At this point, power is increased to the stretching power, 800 mW, for the next 5 seconds, after which it is decreased to 20 mW again (t = 5 sec to t = 10 sec) before the laser is switched off. The difference between the responses of cells and nuclei to stretching force is statistically significant ($p<0.001$).

From the strain dynamics shown in Fig. 4.6, I was able to extract a value for Poisson's ratio (ν), defined as

$$\nu = -\frac{\varepsilon_{\perp}}{\varepsilon_{//}} \quad [38]$$

where $\varepsilon_{//}$ and $\varepsilon_{\perp}$ represent the lateral and axial strain measured when a material is stretched in one direction (Gere & Goodno 2011). In this case they represent the strain along the beam axis and the strain in the perpendicular direction, respectively. Using the strain data in Fig. 4.6, I obtained a value for Poisson's ratio of $\nu = 0.36 \pm 0.04$ for whole cells suspended in the optical stretcher.

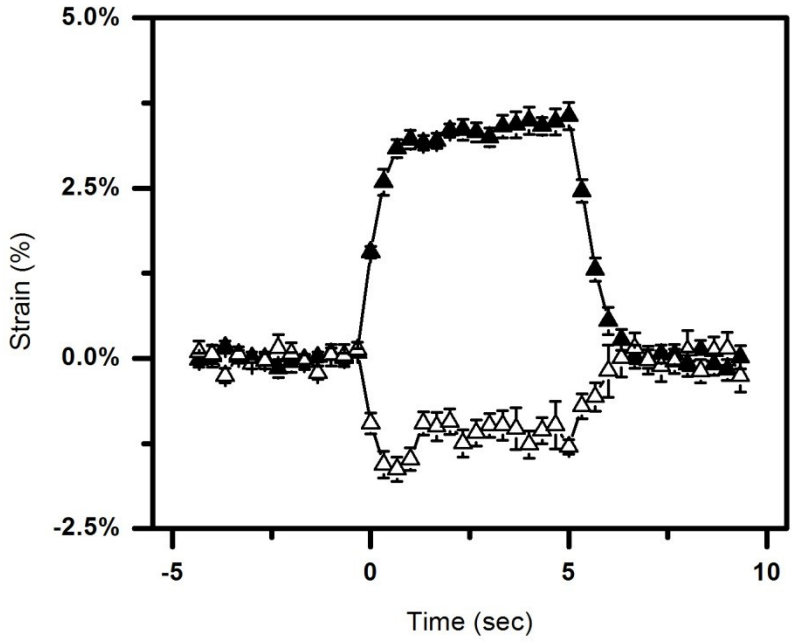

Figure 4.6. Cell membrane strain measured in the optical stretcher. Strain is plotted against time for whole cells along the direction parallel (filled triangles) and perpendicular to the beam axis (open triangles). The difference between the strain dynamics along the two axes is clear ($p<0.001$): the cell tends to expands in the direction parallel to the beam axis, but is compressed in the perpendicular direction.

4.3 Morphology of the Cytoskeleton in Adherent and Suspended 3T3 Fibroblasts

So far, the AFM-LSCM experiments showed results that point to a force-dependent, anisotropic expansion of the cell nucleus in response to constant force, whereas experiments with the optical stretcher yielded no significant nuclear deformation at all. A number of factors could account for this discrepancy. One of these is the magnitude of the applied force: using equations 31-33 in Section 2.2.1, the stretching power used in my experiments (800mW) corresponds to a stretching force of 28.4 pN. This is three orders of magnitude away from the forces I used with the AFM.

Another very important element to consider, however, is that while the nuclei observed in both sets of experiments all come from live, single cells of the same type, these cells are kept in very different conditions. In AFM-LSCM experiments the cells are attached onto the bottom of the culture dish, whereas stretching experiments have them detached and suspended in culture media. Although the nucleus of an adherent cell is visually identical to that of a suspended one, the difference in the structure of the cytoskeleton is substantial and immediately apparent, as shown in Figure 4.7 below.

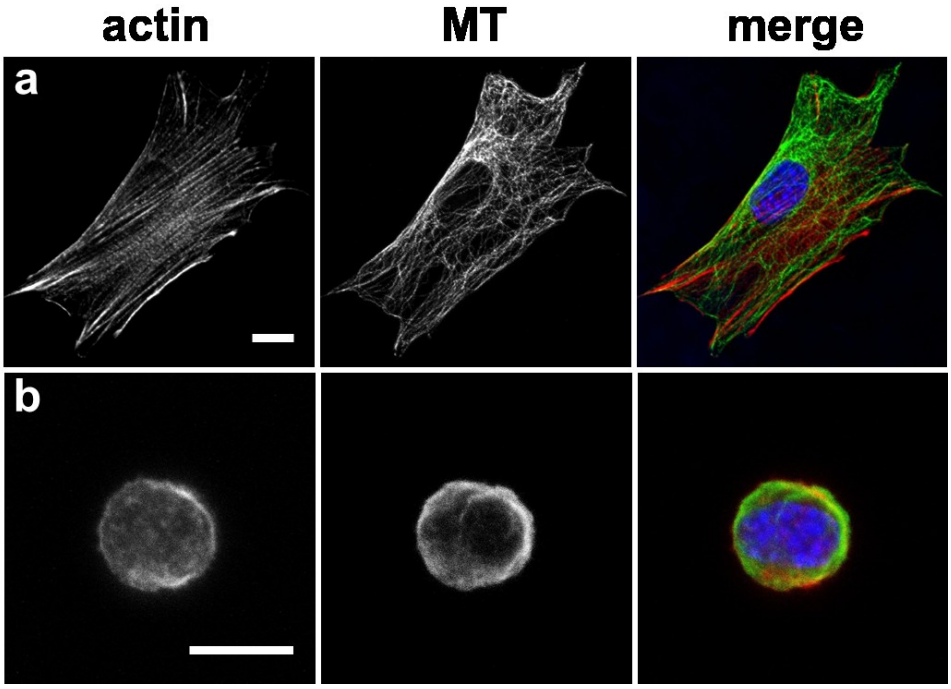

Figure 4.7. Immunofluorescent images of the cytoskeleton in fixed cells. Actin and microtubule (MT) networks are shown for two different morphologies of the same cell type: flat, adherent cells (a) and round cells (b) representative of those suspended within the optical stretcher. Scale bar = 12um for both.

Comparing the cytoskeleton of an adherent cell to that of a round (suspended) cell confirms that the morphology of each of the major filament systems varies greatly between the two cell states. Most notably, adherent cells (Fig 4.7a) have a complex cytoskeleton that includes prominent actin stress fibers. These stress fibers are completely absent in suspended

cells (Fig 4.7b), where the main structural ensemble that actin forms is a thick shell-like structure just beneath the membrane called the actin cortex (Ananthakrishnan, Guck et al. 2006). Microtubules, while emanating from around the nucleus in both cell states, are much more clearly defined in adherent cells. Here they also span the entirety of the cell and radiate to the cell edges, while in suspended cells they radiate towards the actin cortex (Ananthakrishnan, Guck et al. 2006).

It was discussed in Section 1.1.3 that the nucleus is intimately connected to the cell's cytoskeleton. Indeed, the CSK is an integral part of a discrete path of molecular connections that enables the nucleus to respond to a mechanical signal from the cell's microenvironment (Maniotis, Chen et al. 1997). This is supported by the fact that, among other factors, changing the morphology of the cytoskeleton in cells of the same time seems to change the response of the nucleus to external force. In the next chapter, I will further explore the role the CSK plays in modulating the mechanical response of the nucleus.

4.4 References

Ananthakrishnan, R., J. Guck, et al. (2006). "Quantifying the contribution of actin networks to the elastic strength of fibroblasts." J Theor Biol **242**:502-516.

Gere, J.M. and B.J. Goodno (2011). Mechanics of Materials. Cengage Learning, 28-30.

Maniotis, A.J., C.S. Chen et al. (1997). "Demonstration of mechanical connections between integrins, cytoskeletal filaments, and nucleoplasm that stabilize nuclear structure." Proc Natl Acad Sci USA **94**: 849-854.

Chapter 5

Effects of Anti-Cytoskeletal Drugs on the Mechanical Response of the Nucleus

5.1 Morphological Responses Following Treatment with Anti-Cytoskeletal Drugs

In order to determine how each of the cytoskeletal components affects nuclear deformation, I made use of two very well-known anti-cytoskeletal drugs (discussed in Section 2.3.1) to selectively inhibit certain aspects of the CSK. Cytochalasin D (CytD) and nocodazole inhibit the polymerization of actin filaments and microtubules (MTs), respectively. In Figure 5.1, comparative images of cells stained for actin, tubulin, and DNA are presented. Untreated cells display well-defined actin and MT networks (Fig 5.1a). Treatment with nocodazole, however, leaves the actin network intact and results in the depolymerization of MTs (Fig 5.1c). Conversely, treatment with CytD depolymerizes actin, whereas clearly-defined MT filaments still remain (Fig 5.1b). Cells treated with CytD also appear rounder, and exhibit less of a characteristic fibroblast morphology (Yuen, Zak et al., 2008) observed in both nocodazole-treated and control cells. In some experiments I also studied cells treated simultaneously with CytD and nocodazole (CytD-Noco). This double drug treatment yielded cells that exhibited no well-defined fibers for either the actin or the MT network (Fig 5.1d).

Importantly, depolymerization of the MT CSK has a significant effect on the size of the nucleus. It was observed that the area of the nucleus increased by ~40% compared to untreated cells ($p < 0.01$). However, there was no significant difference in nuclear area between untreated, CytD and CytD-Noco treated cells ($p > 0.05$), as seen from the plots in Fig. 5.2.

5.2 Effect of Depolymerizing Actin and MT Filament Networks on Nuclear Deformation

Previously, I have utilized AFM and LSCM to track nuclear deformation in single cells under external applied force. Earlier results demonstrated that nuclear deformation can take place over very fast timescales (millisecond-second) and that most of the deformation takes place within the first few seconds of force application. In order to explore the contribution of

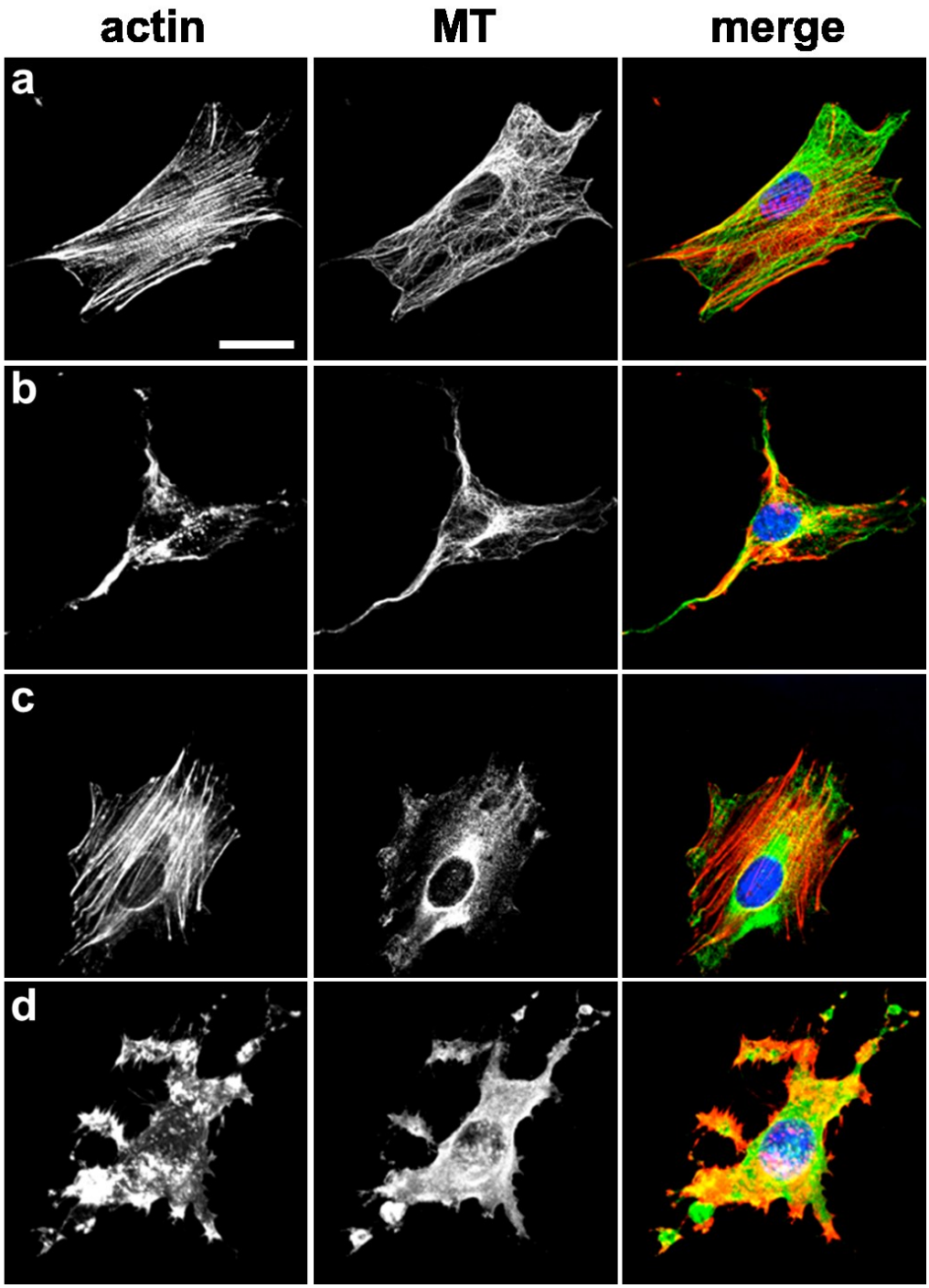

Figure 5.1. Immunofluorescent images of the cytoskeleton in fixed cells in response to various drug treatments. (a) Untreated (scale bar = 20 μm, and applies to all), (b) CytD, (c) nocodazole and (d) CytD-Nocodazole. The CytD treatment specifically depolymerizes actin while leaving MTs intact. Conversely, nocodazole leaves actin filaments intact while specifically depolymerizing MTs. In the double drug treatment (CytD-Noco) both filament systems are depolymerized.

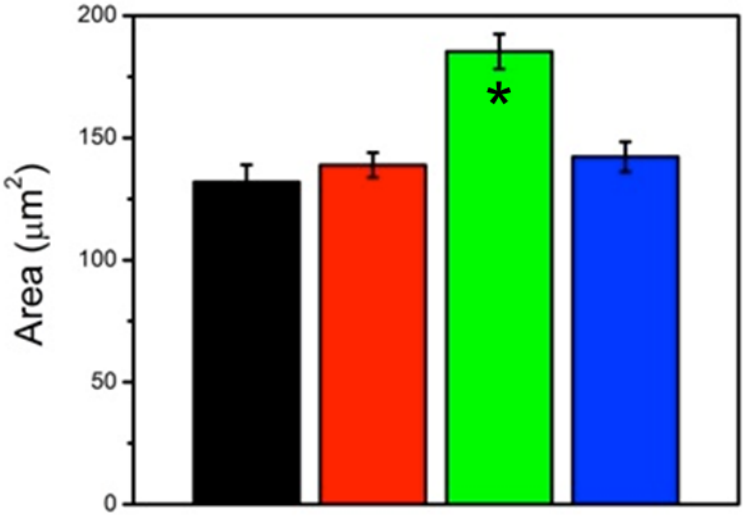

Figure 5.2. Effect of drug treatments on nuclear area. The graph above shows the initial projected nuclear area for untreated (black), CytD (red), nocodazole (green) and CytD-Noco (blue) treated cells. The loss of MTs in response to nocodazole results in a statistically significant (*) increase in nuclear size.

the CSK to nuclear deformation, I have repeated the AFM/LSCM study on cells that had been initially subjected to CytD, nocodazole, and CytD-Noco treatments, comparing the observed responses to that of the untreated cells studied in Chapter 4.

Untreated, CytD, nocodazole and CytD-Noco treated cells all displayed a force-dependent ($p < 0.05$) increase in area (Fig. 5.3). In the absence of force, no significant change in area was observed for the duration of the measurement. The change in normalized area in response to a 10nN (Fig 5.3a) or 20nN (Fig 5.3b) constant force was greatest after CytD-Noco treatment (11 ± 1% and 19 ± 2%, respectively) followed by CytD treatment (10 ± 1% and 19 ± 1%, respectively) and untreated cells (5 ± 1% and 11 ± 1%, respectively). Nocodazole treated cells exhibited the smallest increase in area in response to a 10nN or 20nN constant force (3 ± 1% and 5 ± 1%, respectively).

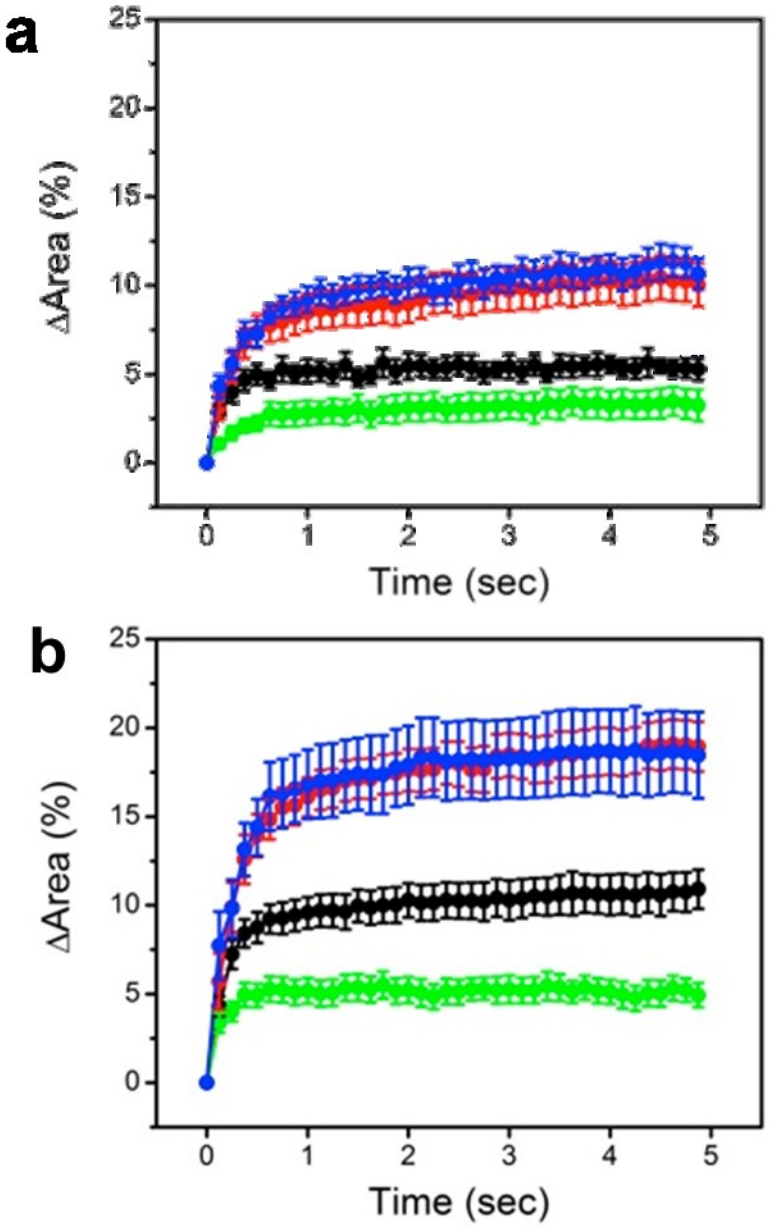

Figure 5.3. Change in nuclear area in response to applied force under various drug conditions. The plots above indicate nuclear deformation for untreated (black), CytD (red), nocodazole (green) and CytD-Noco (blue) treated cells. The change in nuclear area is plotted against time in response to a (a) 10nN and (b) 20nN force. In both cases the nocodazole treatment decreases the change in nuclear area relative to untreated cells indicating an increase in nuclear stiffness. The loss of actin due to CytD or CytD-Noco treatments results in a significant increase in nuclear area in response to force, indicating a decrease in nuclear stiffness.

5.2.1 Observation of Nuclear Strain Anisotropy in Cells Treated with Anti-Cytoskeletal Drugs

Regardless of drug treatment, it was observed that the overall χ (defined in equation 35) decreased from 53° to 52° in response to force ($p < 0.05$, paired t-test) but was not force-dependent ($p > 0.6$), similar to the 15min data presented in Section 4.1. Taking each drug treatment individually saw a significant decrease in ellipticity by 1° ($\Delta\chi$ = -1°) in all cases ($p<0.01$, paired student's t-test), although there is no significant dependence on the drug treatment itself ($p>0.05$). Values for $\Delta\chi$ are listed in Table 5.1.

I also observed the strain along both axes in response to applied force. In order to quantify the strain dynamics (shown in Figure 5.4), I fit the data from these experiments to an expression that predicts deformation of a viscoelastic Kelvin-Voigt material (Crawford 1998; Rosato, Rosato et al. 2001):

$$\varepsilon(t) = \varepsilon_p\left(1 - e^{-t/\tau}\right) \quad [39]$$

where $\varepsilon(t)$ is the time-dependent strain, ε_p represents the plateau strain observed in the long-time elastic regime, and τ is the characteristic relaxation time which is inversely proportional to the deformation rate ($\kappa = \tau^{-1}$). From the fits to the strain data in Fig. 5.4, I extracted values of $\varepsilon_{p,major}$ and $\varepsilon_{p,minor}$ for the major and minor axes, respectively, for each applied force. These values are also listed in Table 5.1. In the case of nocodazole-treated cells, the fits of ~25% of nuclei were very poor for the major axis data only, and these values were excluded from the analysis. Both $\varepsilon_{p,major}$ and $\varepsilon_{p,minor}$ were significantly different from one another ($p < 0.03$) and significantly dependent on the magnitude of the applied force ($p < 0.02$) under all conditions. There was also a significant drug-dependence of $\varepsilon_{p,major}$ and $\varepsilon_{p,minor}$ for all comparisons ($p < 0.02$ and $p < 0.05$, respectively) except when comparing CytD and CytD-Noco treated cells ($p > 0.6$ and $p > 0.4$, respectively). In general, there is a statistically significant force- and drug-dependent response in $\varepsilon_{p,major}$ and $\varepsilon_{p,minor}$ for all conditions, although CytD and CytD-Noco treated cells were indistinguishable from one another. Regardless of the magnitude of applied force, two general phenomena were observed. The first is that cells treated with CytD or CytD-Noco exhibited the largest values of $\varepsilon_{p,major}$ and $\varepsilon_{p,minor}$. Secondly, cells treated with nocodazole alone exhibited significantly lower values for $\varepsilon_{p,major}$ and $\varepsilon_{p,minor}$ compared to untreated cells.

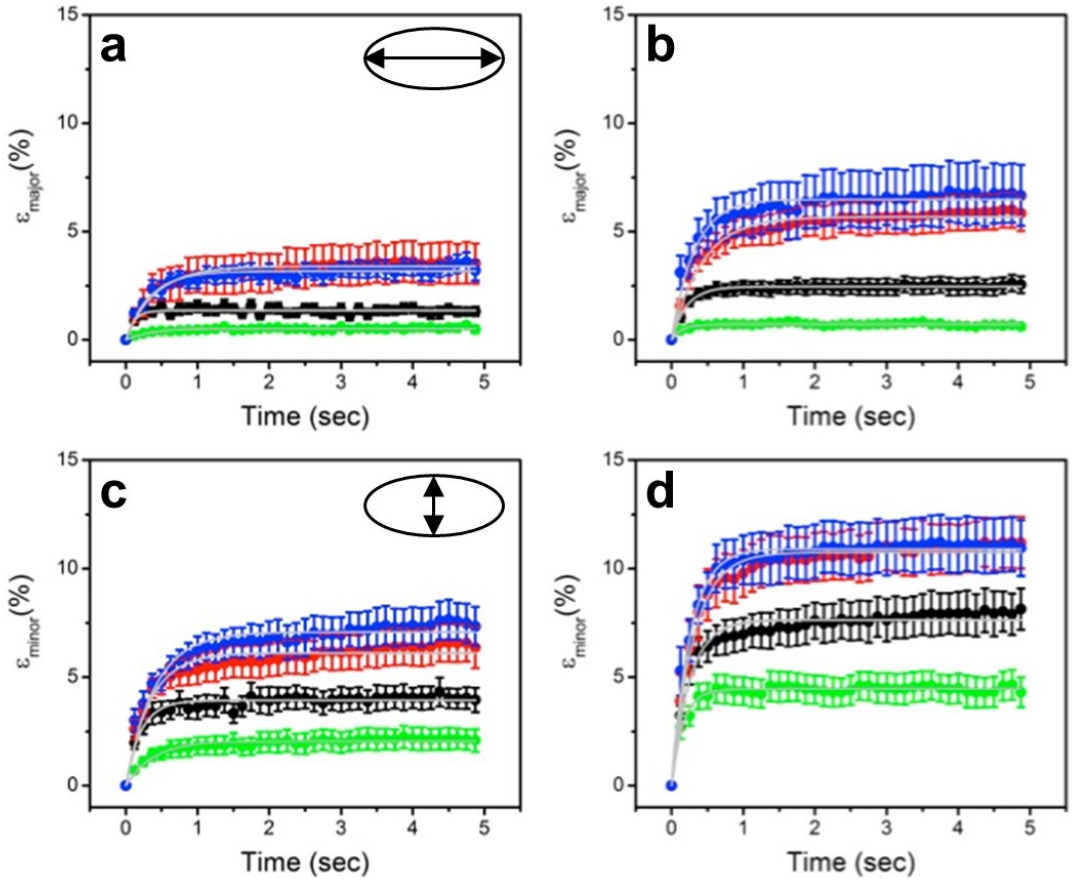

Figure 5.4. Major and minor axis strain in response to applied force under various drug conditions. Nuclear strain dynamics along the major and minor axes observed over 5sec timescales are shown for untreated (black), CytD (red), nocodazole (green) and CytD-Noco (blue) cells. ε_{major} is plotted as a function of time for cells exposed to (a) 10nN or (b) 20nN force. ε_{minor} as a function of time is also plotted for cells exposed to (c) 10nN or (d) 20nN force. The results reveal that the strain magnitude is force-dependent and that the strain is anisotropic under all drug conditions. In all cases, the data was fit with equation 39 (grey lines) in order to extract the plateau strain (ε_p) and the characteristic deformation rate (κ), which are summarized in Table 5.1 and Fig. 5.5 respectively.

I also calculated the anisotropy parameter α for nuclei exposed to force using the values of the plateau strains $\varepsilon_{p,major}$ and $\varepsilon_{p,minor}$ in equation 37. Consistent with the 15min data presented in Section 4.1, α displayed no significant dependence on the magnitude of the applied force ($p > 0.2$) or on drug treatment ($p > 0.1$). Values for α, in addition to the other parameters indicating nuclear anisotropy discussed earlier ($\Delta\chi$, $\varepsilon_{p,major}$ and $\varepsilon_{p,minor}$), are shown together in Table 5.1:

Table 5.1: Summary of Parameters Indicating Anisotropy in Nuclear Deformation Following Treatment with Anti-Cytoskeletal Drugs

Treatment	$\Delta\chi$		$\varepsilon_{p,major}$ (%)		$\varepsilon_{p,minor}$ (%)		α	
	10nN	20nN	10nN	20nN	10nN	20nN	10nN	20nN
Untreated	~-1°	~-1°	1.4±0.2	2.5±0.4	3.9±0.5	7.7±0.9	0.4±0.1	0.4±0.1
CytD	~-1°	~-1°	3.4±0.9	5.8±0.8	6.1±0.8	10.8±1.1	0.6±0.2	0.6±0.1
Nocodazole	~-1°	~-1°	0.6±0.2	0.9±0.1	1.4±0.2	4.7±0.7	0.5±0.1	0.3±0.1
CytD-Noco	~-1°	~-1°	3.2±0.4	6.5±1.3	7.2±0.8	10.9±1.2	0.5±0.1	0.6±0.1

In each of the cases presented above, the change in ellipticity of the nucleus is negative ($\Delta\chi < 0$), the plateau strain along the minor axis is significantly greater than that along the major axis ($\varepsilon_{p,major} < \varepsilon_{p,minor}$), and α is consistently less than 1. This indicates that the nucleus expands anisotropically under all conditions, even when lacking an intact actin and/or microtubule cytoskeleton.

5.2.2 Deformation Rates

Deformation rates were determined from the fits of equation 39 ($\kappa_{major} \approx \kappa_{minor} \approx 5\ s^{-1}$) and were observed to display a significant amount of variance, falling in the range of 0.1–30 s^{-1}, as seen from the plots in Figure 5.5. κ values displayed no significant dependence on the magnitude of the applied force, drug treatment or between the major and minor axes ($p > 0.2$).

5.2.3 Effective Stiffness

In order to quantify the physical implications of these results, we recall that the long-time elastic modulus (ξ) of the material is the ratio between the applied stress σ and the plateau strain ε_p:

$$\xi = \frac{\sigma}{\varepsilon_p} \quad [40]$$

As described earlier, α is a measure of the anisotropic strain that occurs along the major and minor axes of the nucleus. Therefore, under a constant stress σ one can write:

$$\alpha = \frac{\varepsilon_{p,\mathrm{major}}}{\varepsilon_{p,\mathrm{minor}}} = \frac{\xi_{\mathrm{minor}}}{\xi_{\mathrm{major}}} \quad [41]$$

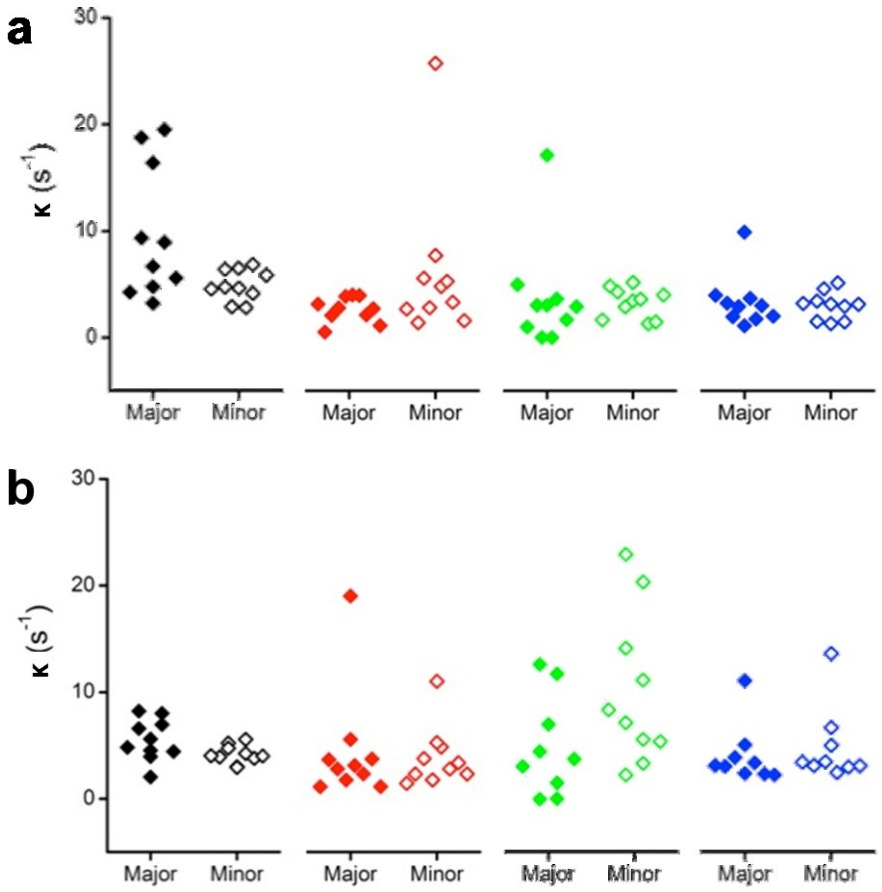

Figure 5.5. The deformation rate constants determined using fits of Equation 39 to the strain data ($\kappa = \tau^{-1}$). All measured values for κ_{major} and κ_{minor} are plotted for untreated (black), CytD (red), nocodazole (green) and CytD-Noco (blue) cells in response to (a) 10nN and (b) 20nN forces. The values of κ are highly variable and independent of the applied force, drug treatment and not significantly different along the major or minor axis. The results reveal that the deformation rate (~$5s^{-1}$) is controlled by the nucleus itself and independent of the state of the cytoskeleton.

Since α is always less than 1 (as seen in Table 5.1), this implies that the nucleus has a larger ξ_{major} than ξ_{minor}, indicating a clear mechanical anisotropy in the material properties of the nucleus. In order to examine the change in ξ_{major} and ξ_{minor} after drug treatments compared to untreated cells, the effective elastic modulus (ξ_{eff}) can be determined along each of the nuclear axes using the values of ε_p determined from equation 39:

$$\xi_{\text{eff}} = \frac{\xi_{\text{drug}}}{\xi_{\text{untreated}}} = \frac{\varepsilon_{p,\text{untreated}}}{\varepsilon_{p,\text{drug}}} \qquad [42]$$

The results demonstrate that the loss of actin after CytD or CytD-Noco treatment leads to an effective softening of the nucleus ($\xi_{eff,major} \approx \xi_{eff,minor} \approx 0.7$). Importantly, treatment with CytD-Noco reveals physical properties and structural characteristics that are statistically indistinguishable from CytD treatment alone ($p > 0.4$). Conversely, the loss of MTs after nocodazole treatment results in an effective threefold stiffening of the nucleus ($\xi_{eff,major} \approx \xi_{eff,minor} \approx 2.8$). Under each given condition ξ_{eff} was not dependent on the magnitude of the applied force ($p > 0.09$) and there was no statistically significant difference between $\xi_{eff,major}$ and $\xi_{eff,minor}$ in any case ($p > 0.4$). This indicates that loss of cytoskeletal filaments results in a global change in the effective stiffness of the nucleus and is not limited to one axis, regardless of the deformation anisotropy. Values for $\xi_{eff,major}$ and $\xi_{eff,minor}$ under each of the three different drug conditions are shown in Table 5.2:

Table 5.2: Effective Elastic Moduli along the Major and Minor Axes of the Nucleus

Treatment	$\xi_{eff,\ major\ axis}$		$\xi_{eff,\ major\ axis}$	
	10nN	20nN	10nN	20nN
CytD	0.8 ± 0.2	0.5 ± 0.1	0.8 ± 0.1	0.8 ± 0.1
Nocodazole	3.2 ± 0.9	2.9 ± 0.2	3.1 ± 0.3	2.1 ± 0.4
CytD-Noco	0.5 ± 0.1	0.5 ± 0.1	0.7 ± 0.1	0.9 ± 0.2

5.3 Effects of Anti-Cytoskeletal Drugs on Intermediate Filaments

Up to this point we have ignored the role of intermediate filaments (IFs), which do play important roles in governing the mechanical properties of whole cells (Lazarides 1980; Fuchs & Weber 1994; Fuchs & Cleveland 1998). We generated cells transiently expressing vimentin-GFP (a major IF protein) and stained the nucleus and actin CSK after treating with CytD, nocodazole and CytD-Noco (Fig. 5.6). Untreated cells and cells treated with CytD alone exhibit similar morphologies, with well-defined vimentin IFs spread throughout the entirety of the cell body. However, in cells treated with nocodazole (whether alone or simultaneously with CytD), the IF network tended to condense around the nucleus. From this result, it is tempting to explain the

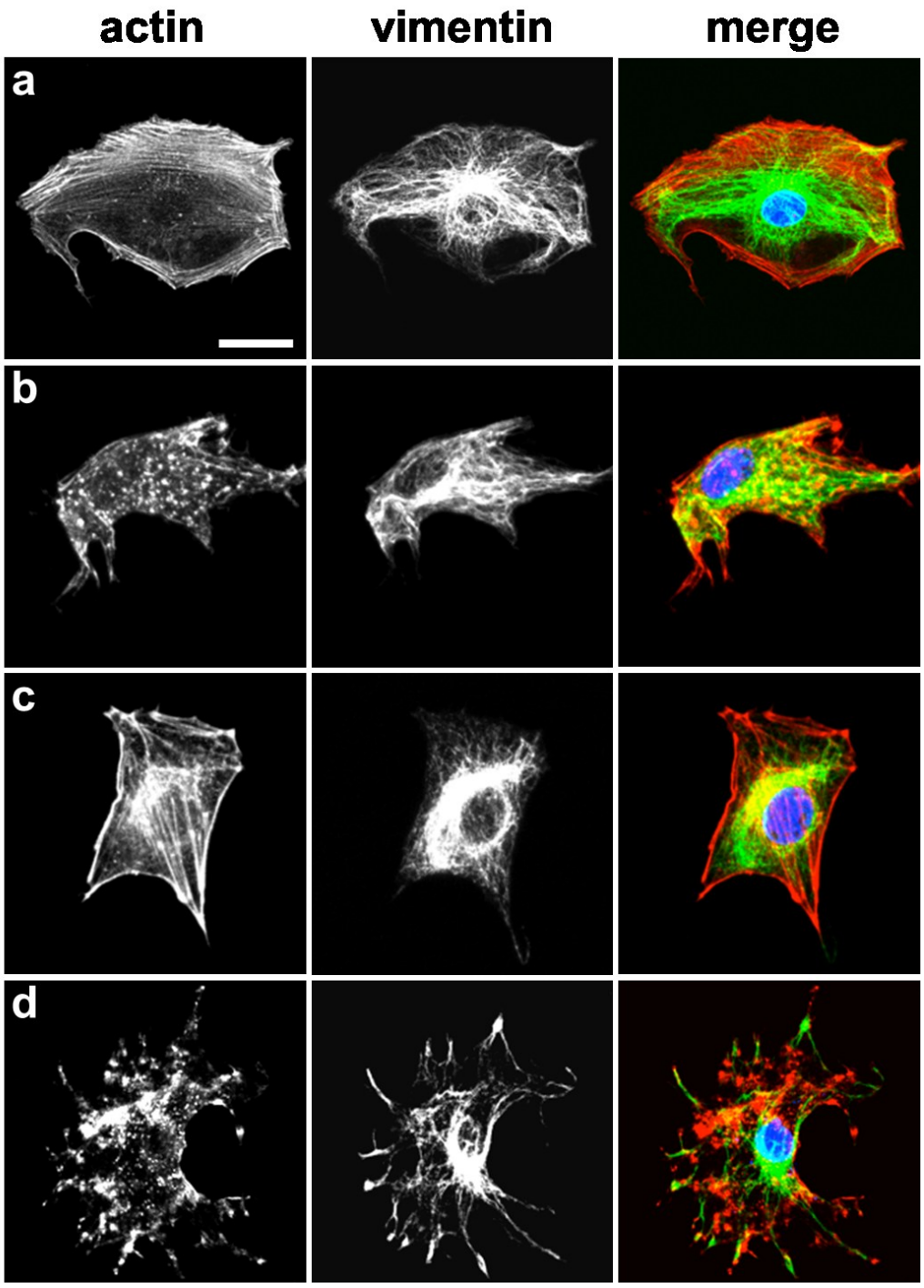

Figure 5.6. Immunofluorescent images of actin and the nucleus in fixed cells expressing vimentin-EGFP, in response to various drug treatments. (a) Untreated (scale bar = 20 µm, and applies to all), (b) CytD, (c) Nocodazole and (d) CytD-Nocodazole treated cells are shown. In all cases, a loss of actin or MTs results in a slight increase in IF density around the nucleus. However, no clear changes in IF morphology were observed specifically in response to nocodazole treatment. Therefore, the IF cytoskeleton does not appear to be causing the apparent increase in nuclear stiffness upon loss of MTs.

nocodazole-induced increase in ξ as originating from this increase in IF density around the nucleus, effectively inhibiting nuclear deformation. However, the nucleus not only increases in size due to nocodazole treatment by ~40% on average (as seen in Fig. 5.2), but the apparent increase in ξ does not occur in CytD-Noco cells even though the IFs maintain the same perinuclear morphology. Therefore, while IFs are highly important in governing nuclear shape and structure (Sarria, Lieber et al. 1994), the data suggests that they do not appear to be governing the deformation mechanics of the nucleus in mouse NIH3T3 cells. These are somewhat surprising results, but they are not necessarily representative of a general phenomenon occurring in all cell types and contexts.

5.4 References

Crawford, R.J. (1998). Plastics Engineering. Butterworth-Heinemann, 87-89.

Fuchs, E. and D.W. Cleveland (1998). "A structural scaffolding of intermediate filaments in health and disease." Science **279**: 514-519.

Fuchs, E. and K. Weber (1994). "Intermediate filaments: structure, dynamics, function and disease." Annu Rev Biochem **63**: 345-382.

Lazarides, E. (1980). "Intermediate filaments as mechanical integrators of cellular space." Nature **283**: 249-255.

Rosato, D.V., M. G. Rosato et al. (2001) Plastics Engineering, Manufacturing & Data Handbook. Kluwer Academic Pub.

Sarria, A.J., J.G. Lieber et al. (1994). "The presence or absence of a vimentin-type intermediate filament network affects the shape of the nucleus in human SW-13 cells." J Cell Sci **107**: 1593-1607.

Yuen, F.L.Y., G. Zak, et al (2008). "Morphology of fibroblasts grown on substrates formed by dielectrophoretically aligned carbon nanotubes." Cytotechnology **56**: 9-17.

Chapter 6

Nuclear Deformation under Cyclic Force Application

6.1 Mechanical Response of the Nucleus to Cyclic Force Application

Until this point, all the experiments I have performed using simultaneous AFM and LSCM involved the application of a constant (static) force onto the nucleus of single, adherent NIH3T3 fibroblasts. My previous results pointed to a force-dependent, anisotropic expansion of the nucleus in the plane normal to the force application. In addition, the nucleus was found to expand anisotropically even when cells were treated with the anti-cytoskeletal drugs cytochalasin D (CytD) and nocodazole. In this chapter, I investigated whether this anisotropy in nuclear deformation is conserved even under repeated (cyclic) force application.

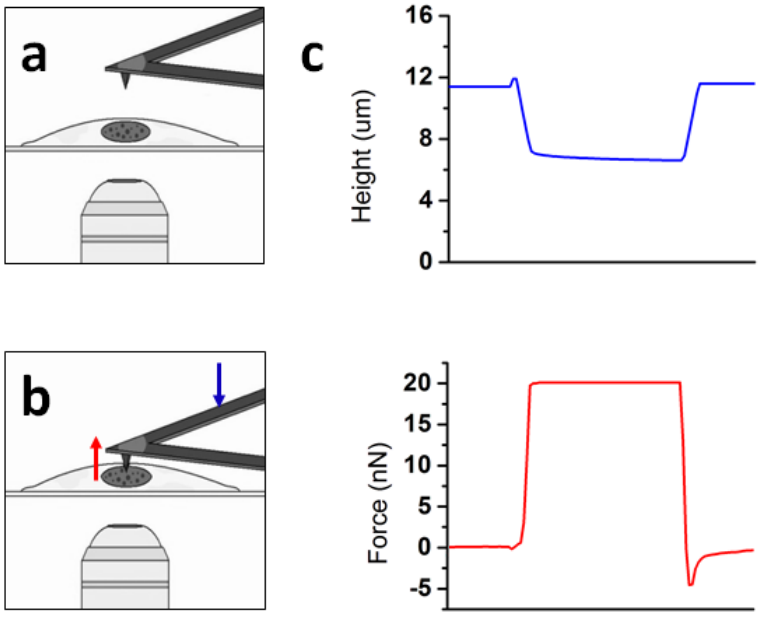

Figure 6.1. Cyclic AFM/LSCM experiment. Similar to previous AFM/LSCM experiments, the cantilever of the AFM was aligned over the center of the nucleus of the target cell (a). The tip was then extended to apply a constant force (b) for exactly 5 seconds before being retracted. The tip was kept retracted for exactly 10 seconds ('resting' period) before being extended again, repeating the cycle. Comparative graphs show plots of cantilever height (blue), and force (red) against time for one cycle (c) which was performed 15 times for each cyclic AFM/LSCM experiment.

In these sets of experiments, nuclear deformation was observed by performing simultaneous AFM and LSCM, in which the cantilever of the AFM was aligned over the center of

the nucleus, and then periodically extended and retracted in order to apply a cyclic force. This process is shown schematically in Figure 6.1. Either 10 nN or 20nN of force was applied with the AFM tip for 5 seconds for 15 cycles, with 10-second 'resting' periods with the tip retracted (no force) in between each cycle. With the confocal acquisition plane set in the middle of the nucleus, images were then taken at 8 frames per second for the entire duration of the 15 cycle experiment. These experiments were performed for untreated as well as CytD- and nocodazole-treated cells. Deformation was quantified by the normalized change in projected area (shown in Figures 6.2-6.3) of the nucleus as a function of time. However, in the absence of applied force there was no significant change in normalized area throughout the entire duration of the experiment, as shown in Figure 6.2.

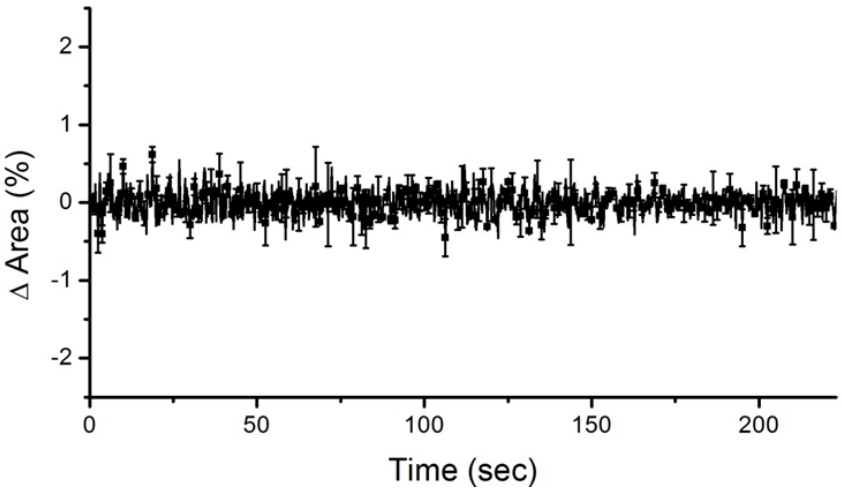

Figure 6.2. Change in nuclear area in the absence of applied force. The plot above indicates the change in nuclear area for untreated cells (n=3) in the absence of applied force over a period of time equivalent to the duration of a cycling experiment (t = 225 seconds). The nuclear area remains effectively constant throughout that time period, fluctuating between ΔArea = ± 0.5%.

As in the static AFM/LSCM experiments, all cells displayed a force-dependent increase in projected nuclear area, regardless of treatment conditions. This force-dependent increase was observed for each individual cycle ($p < 0.05$). For the first cycle, the change in normalized area in response to a 10nN (Fig 6.3a) or 20nN (Fig 6.3b) force was greatest after the CytD treatment (11 ± 2% and 18 ± 2%, respectively), followed by untreated cells (6 ± 1% and 11 ± 1%, respectively), and then nocodazole-treated cells (3 ± 1% and 5 ± 1%, respectively). These are

equivalent to the changes in normalized area measured in response to the static 5-second force application discussed in Section 5.2. After this initial force application, the nucleus returned to its initial size (ΔArea ≈ 0%) for the duration of the 10-second 'resting' period, regardless of the magnitude of initial force applied, and for all treatment conditions.

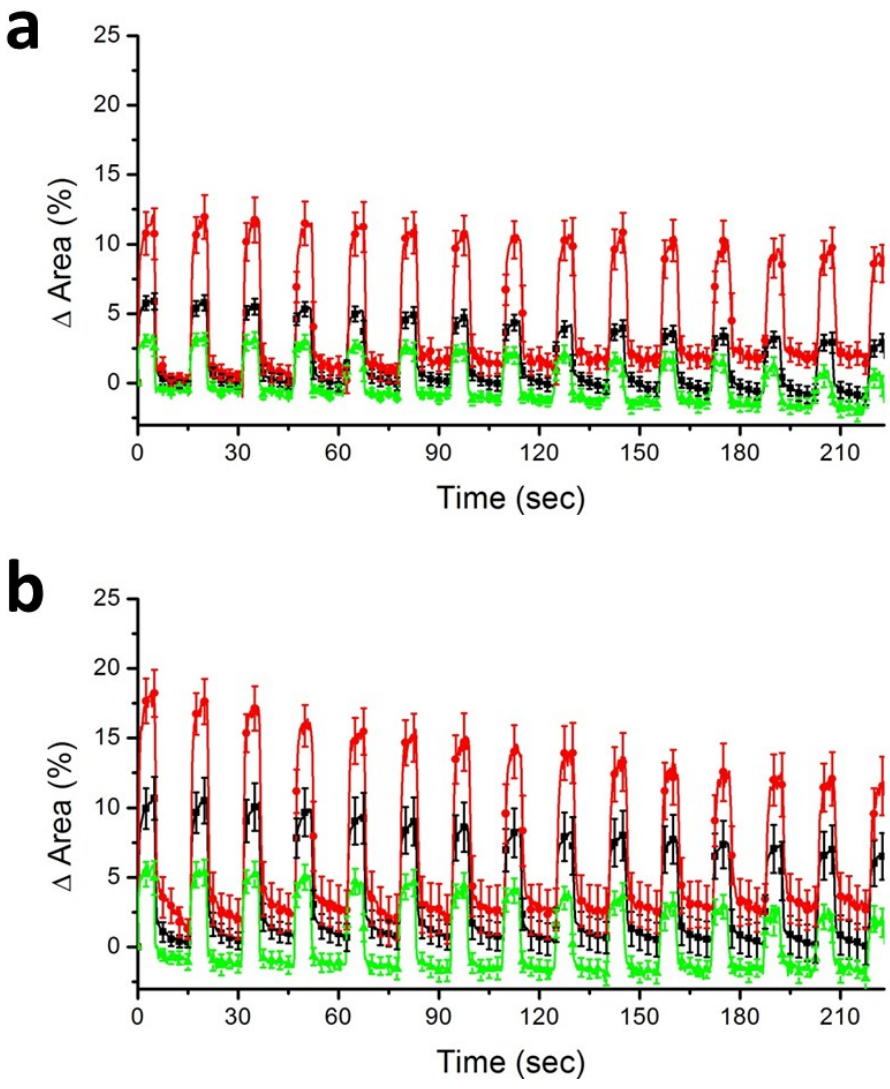

Figure 6.3. Change in nuclear area in response to cyclic force under various drug conditions. The plots above indicate nuclear deformation for untreated (black), CytD (red) and nocodazole (green) treated cells. Data sets were sampled at 8 fps, but only every 10th point is shown for clarity. The change in nuclear area is plotted against time in response to (a) 10nN and (b) 20nN cyclic force. As in the static force experiments, the nocodazole treatment decreases the change in nuclear area relative to untreated cells, while the CytD treatment increases it.

There was no significant difference among the magnitudes of the area change observed between cycles, regardless of the applied force. This was true for untreated ($p>0.1$), CytD- ($p>0.06$) and nocodazole-treated cells ($p>0.2$). There was no significant difference among the magnitudes of the area change observed between 'resting' periods, either, for all forces and treatment conditions. However, there was a significant dependence of the area change on drug treatment ($p<0.01$) for each cycle, although this dependence vanished when comparing area changes between 'resting' periods ($p>0.05$). This suggested that during each 'resting' period, the nucleus returned to its approximate size prior to the initial force application, regardless of cycle number. The nucleus also displayed fairly consistent deformation behavior throughout the 15 cycles that was dependent only on the applied force and treatment conditions; the cycle number, or how many times the nucleus had been perturbed beforehand, was irrelevant.

6.2 Observation of Nuclear Strain Anisotropy in Cyclic AFM/LSCM Experiments

In addition to the increase in nuclear area, I also studied the strain along both axes in response to cyclic applied force. In order to quantify this, I took each portion of the strain curve corresponding to a force application and fit these data sets separately to equation 39. Using this method, I was able to extract values for the deformation rate ($\kappa = \tau^{-1}$) and the plateau strain along both axes ($\varepsilon_{p,major}$ and $\varepsilon_{p,minor}$) for each of the 15 cycles. For the purposes of this thesis I have presented here the strain dynamics and fitting results for the 10nN strain data (shown in Figure 6.4); the 20nN data, although not shown, follows a similar trend in all aspects.

Similar to the results from the static experiments, cells treated with CytD exhibited the largest values of $\varepsilon_{p,major}$, whereas cells treated with nocodazole exhibited significantly lower values for $\varepsilon_{p,major}$ compared to untreated cells for the first 5 cycles. Beyond cycle 5, however, $\varepsilon_{p,major}$ values were not significantly different between untreated and nocodazole-treated cells ($p>0.05$, student's paired t-test), although they were both significantly different from CytD-treated cells ($p<0.01$). $\varepsilon_{p,minor}$ was significantly dependent on drug treatment for all comparisons

($p<0.02$), and for all cycles. $\varepsilon_{p,minor}$ was highest for CytD-treated cells, followed by untreated cells, and lastly nocodazole-treated cells.

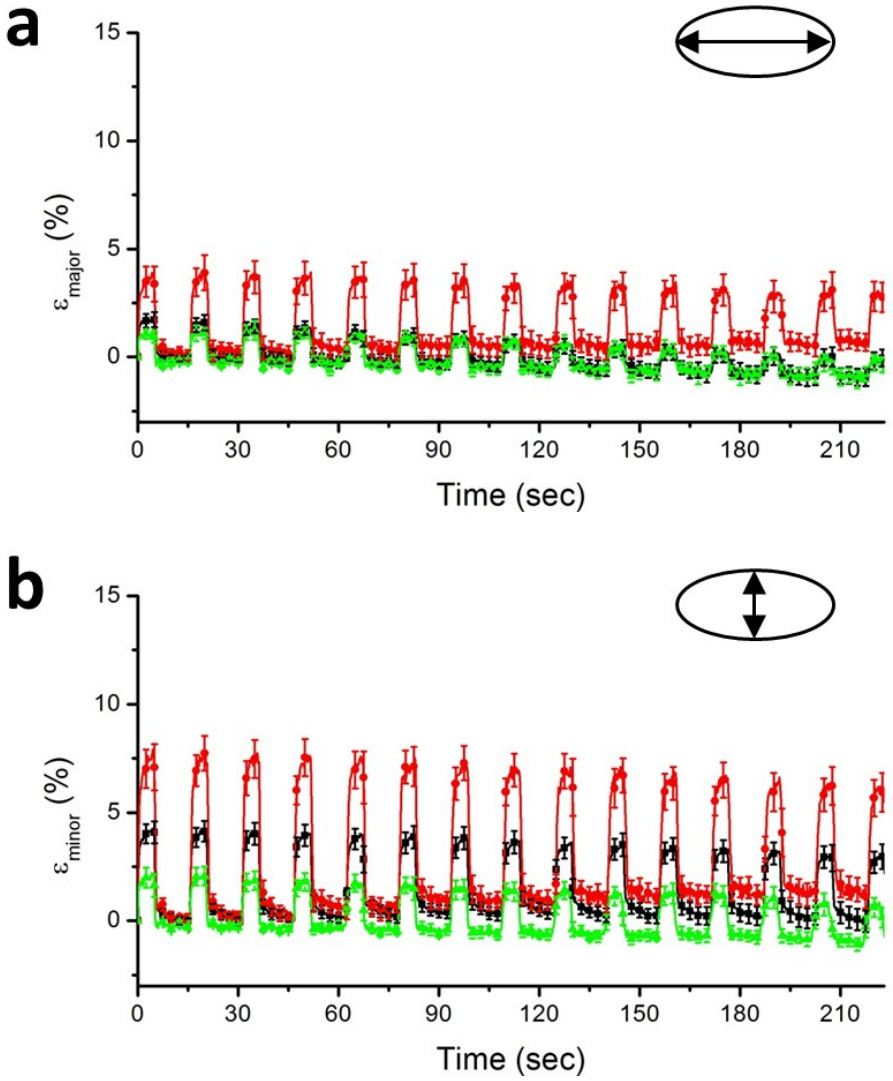

Figure 6.4. Major and minor axis strain in response to 10nN cyclic force under various drug conditions. Nuclear strain dynamics along the major and minor axes observed over the 15 cycle duration are shown for untreated (black), CytD (red), and nocodazole (green) treated cells. All sets of data were sampled at 8 fps, but only every 10^{th} point is shown for clarity. (a) ε_{major} and (b) ε_{minor} are plotted as functions of time for cells exposed to 10nN cyclic force. As in the static experiments, the strain magnitude is force-dependent and anisotropic under all drug conditions. 15 separate strain curves (taken from the data corresponding to periods of force application) were fit to equation 39 in order to extract the plateau strain (ε_p) and the characteristic deformation rate (κ) along each axis. These values are summarized in Table 6.1 and Figures 6.7-6.8, respectively.

Notably, $\varepsilon_{p,major}$ and $\varepsilon_{p,minor}$ were significantly different from one another ($p<0.05$) under all treatment conditions, and for all cycles. Except for the nocodazole strain data along the major axis, where the fit was once again poor for ~20% of the data, Cycle 1 values for $\varepsilon_{p,major}$ and $\varepsilon_{p,minor}$ were similar to those obtained in the 10nN static experiments: CytD-treated cells (4 ± 0.6% and 7.4 ± 0.8%, respectively), untreated cells (1.9 ± 0.4% and 4 ± 1%, respectively), and nocodazole-treated cells (1.2 ± 0.3% and 2.3 ± 0.6%, respectively).

Values for $\varepsilon_{p,major}$ or $\varepsilon_{p,minor}$ under any particular treatment were not, however, significantly different between cycles ($p>0.05$ for all comparisons). To illustrate this, Figure 6.5 below shows $\varepsilon_{p,major}$ and $\varepsilon_{p,minor}$ plotted against cycle number for untreated cells:

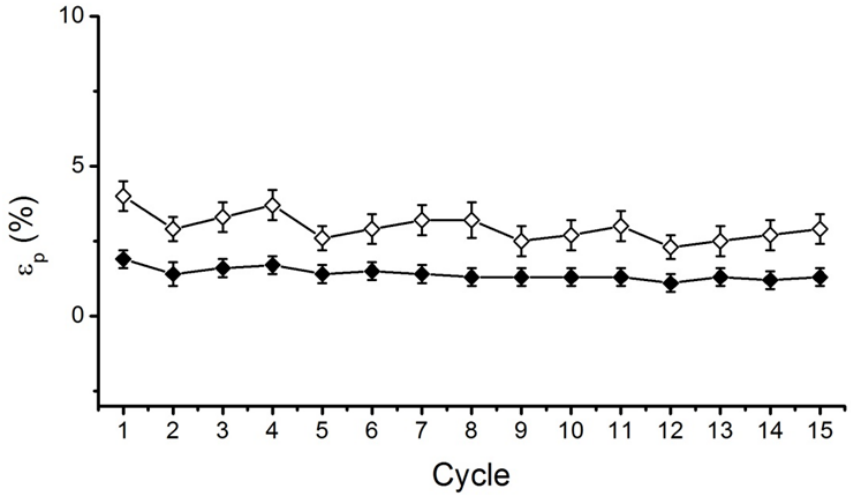

Figure 6.5. Plateau strain along major and minor axes in response to 10nN cyclic force for untreated cells. Values for $\varepsilon_{p,major}$ (filled diamonds, black) and $\varepsilon_{p,minor}$ (empty diamonds) are plotted as functions of cycle number for untreated cells exposed to 10nN cyclic force. Neither $\varepsilon_{p,major}$ nor $\varepsilon_{p,minor}$ is dependent on the cycle number.

Lastly, I calculated the anisotropy parameter α for nuclei exposed to cyclic force using the values of $\varepsilon_{p,major}$ and $\varepsilon_{p,minor}$ obtained for each individual cycle in equation 37. As with the static experiment data presented in Section 5.2.1, α exhibited no significant dependence on the magnitude of the applied force ($p>0.1$), or on the drug treatment ($p>0.07$). Furthermore, α did not change significantly with succeeding cycles ($p>0.8$), as shown in Figure 6.6.

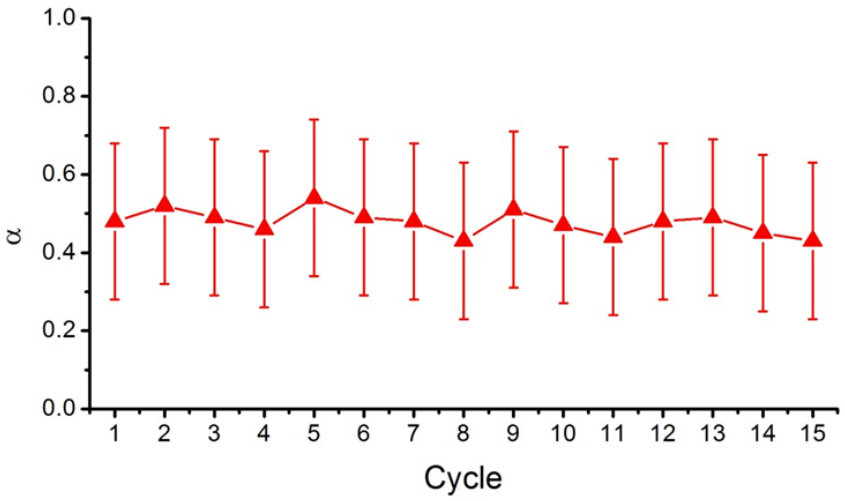

Figure 6.6. Degree of nuclear anisotropy does not vary with cycle number. α is plotted versus cycle number for untreated cells exposed to 10nN cyclic force. As with the plateau strain along either axis, it is not dependent on the cycle number.

Although not shown, the plots of α, $\varepsilon_{p,major}$ and $\varepsilon_{p,minor}$ against cycle number for CytD- and nocodazole-treated cells are similar to those shown for untreated cells in Fig. 6.5-6.6 in one important aspect: although the values fluctuate, the behavior of each of these parameters with increasing cycle number exhibits no real trend. Values for α, $\varepsilon_{p,major}$ and $\varepsilon_{p,minor}$, obtained from fits for each of the 15 cycles and for all drug treatments, are shown together in Table 6.1. These values show that the plateau strain along the minor axis is consistently greater than that along the major axis ($\varepsilon_{p,major} < \varepsilon_{p,minor}$), and that α is consistently less than 1. These results indicates that, over the course of the 15-cycle experiment, the nucleus expands anisotropically under all treatment conditions, regardless of how many times it was perturbed beforehand.

6.3 Deformation Rates for Cyclic 10nN Strain Data

Deformation rates were determined from the fits of equation 39 to the same strain data analyzed for plateau strain. Just as in the static force experiments, κ values displayed significant variance, ranging between 0.1 and 20 s^{-1}, as seen from the plots in Fig. 6.7-6.8.

Table 6.1: Summary of Parameters Indicating Anisotropy in Nuclear Deformation Under Cyclic Force Application

Cycle	Untreated			CytD			Nocodazole		
	$\varepsilon_{p,major}$ (%)	$\varepsilon_{p,minor}$ (%)	α	$\varepsilon_{p,major}$ (%)	$\varepsilon_{p,minor}$ (%)	α	$\varepsilon_{p,major}$ (%)	$\varepsilon_{p,minor}$ (%)	α
1	1.9±0.3	4.0±0.5	0.48±0.2	4.0±0.6	7.5±0.8	0.54±0.1	1.2±0.3	2.3±0.6	0.53±0.3
2	1.4±0.4	2.9±0.4	0.52±0.2	3.9±0.6	7.1±0.9	0.55±0.2	1.1±0.4	2.2±0.4	0.47±0.5
3	1.6±0.3	3.3±0.5	0.49±0.2	4.4±0.5	7.6±0.9	0.57±0.1	0.9±0.3	1.9±0.5	0.46±0.3
4	1.7±0.3	3.7±0.5	0.46±0.2	4.0±0.7	7.4±0.9	0.55±0.2	1.0±0.4	2.0±0.5	0.47±0.3
5	1.4±0.3	2.6±0.4	0.54±0.2	3.5±0.7	6.7±1.0	0.53±0.2	1.1±0.3	1.6±0.4	0.71±0.4
6	1.5±0.3	2.9±0.5	0.49±0.2	3.7±0.6	6.3±0.7	0.59±0.2	0.7±0.6	1.5±0.5	0.49±0.3
7	1.4±0.3	3.2±0.5	0.48±0.2	4.0±0.8	6.7±0.8	0.60±0.2	1.2±0.4	1.7±0.5	0.71±0.5
8	1.3±0.3	3.2±0.6	0.43±0.2	3.7±0.6	6.3±0.7	0.58±0.2	1.1±0.4	1.5±0.5	0.72±0.4
9	1.3±0.3	2.5±0.5	0.51±0.2	3.6±1.0	6.1±0.7	0.60±0.2	0.8±0.6	1.4±0.5	0.56±0.6
10	1.3±0.3	2.7±0.5	0.47±0.2	3.6±0.6	6.0±0.7	0.60±0.2	0.7±0.3	1.1±0.4	0.62±0.5
11	1.3±0.3	3.0±0.5	0.44±0.2	3.6±0.8	6.1±0.7	0.58±0.2	0.6±0.5	1.6±0.5	0.40±0.4
12	1.1±0.3	2.3±0.4	0.48±0.2	2.9±0.8	5.5±0.8	0.53±0.2	0.7±0.5	1.3±0.5	0.54±0.6
13	1.3±0.3	2.5±0.5	0.49±0.2	3.4±0.7	5.5±0.8	0.60±0.2	0.6±0.5	1.0±0.5	0.50±0.6
14	1.2±0.3	2.7±0.5	0.45±0.2	3.3±0.8	5.3±0.8	0.62±0.2	0.7±0.5	1.4±0.5	0.48±0.5
15	1.3±0.3	2.9±0.5	0.43±0.2	2.9±0.7	5.4±0.8	0.54±0.2	0.6±0.5	1.2±0.5	0.48±0.4

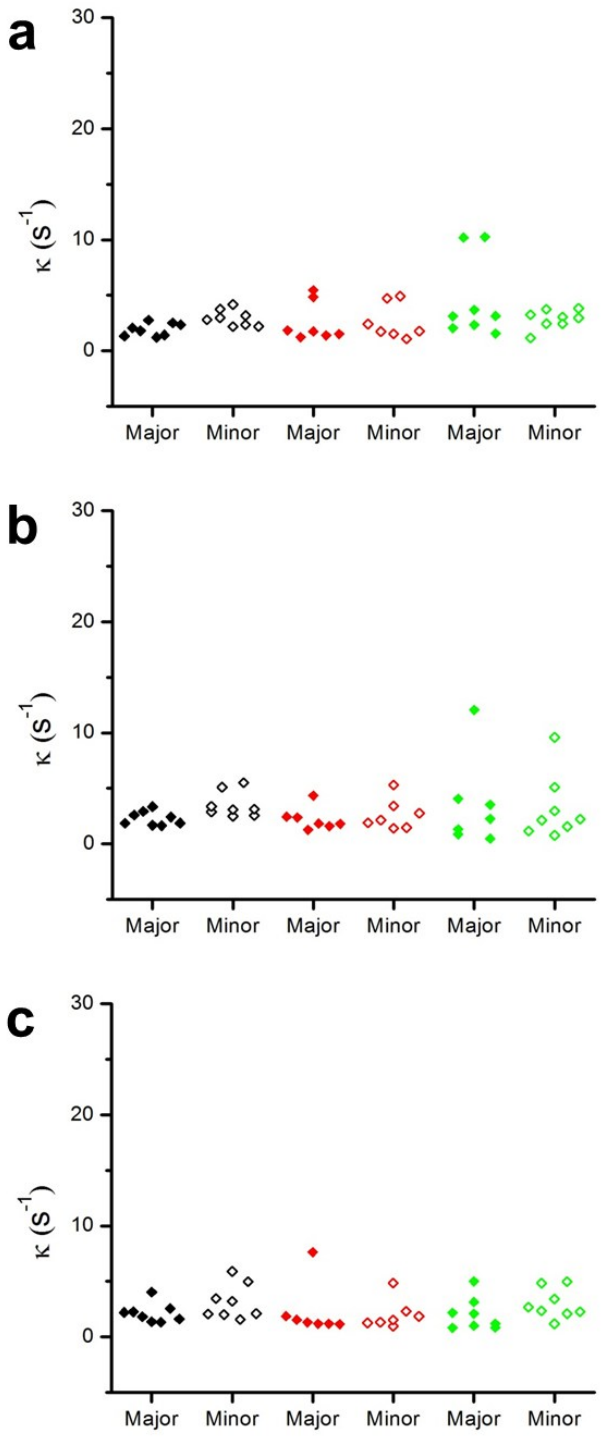

Figure 6.7. Deformation rate constants determined using fits of Equation 39 to cyclic strain data (Cycles 1-3). All measured values for κ_{major} and κ_{minor} are plotted for untreated (black), CytD (red), and nocodazole (green) treated cells in response to 10nN cyclic force. Values are shown for (a) Cycle 1, (b) Cycle 2, and (c) Cycle 3.

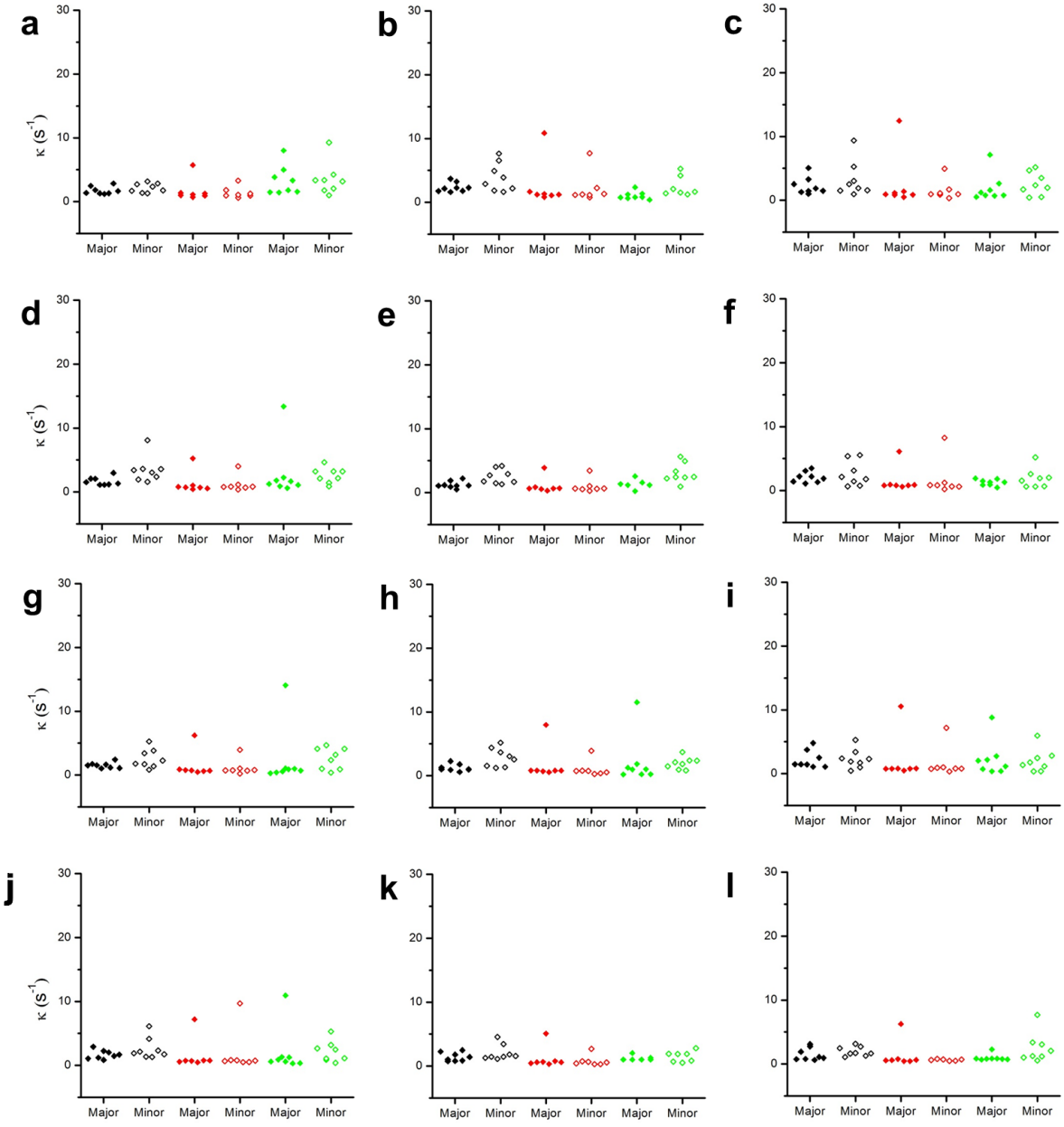

Figure 6.8. Deformation rate constants determined using fits of Equation 39 to cyclic strain data (Cycles 4-15). All measured values for κ_{major} and κ_{minor} are plotted for untreated (black), CytD (red), and nocodazole (green) treated cells in response to 10nN cyclic force. Values are shown for Cycles 4 through 15 (a through l, respectively). The values of κ obtained are highly variable, and not dependent on the drug treatment ($p>0.09$). They are not significantly different along the major or minor axis ($p>0.2$), or between any cycle comparisons ($p>0.1$). These results show that the deformation rate is not only independent of the state of the cytoskeleton, but also of any previous perturbation throughout the 15-cycle experiment (cycle number).

Chapter 7

Discussion and Conclusions

7.1 The Mechanical Response of the Nucleus to External Force in 3T3 Fibroblast Cells

In Chapter 1 I discussed how forces applied to the cell nucleus can induce changes in gene expression by affecting chromatin structure, nuclear compartmentalization and other regulatory factors which are physically contained within the nucleus (Dahl, Engler et al. 2005). This, in addition to remodelling of nuclear architecture during differentiation and the association of altered nuclear properties with disease (discussed in Section 1.3.3), shows the intimate link between fundamental biological processes and nuclear mechanics (Dahl, Ribeiro et al. 2008; Dahl & Kalinowski 2011).

In general, when a cell is exposed to a physical force from the microenvironment, an initial elastic response is followed by a slow compression of the cytoskeleton with an average time constant on the order of seconds (Wu, Kuhn et al. 1998). The results of this thesis have demonstrated that nuclear deformation can take place over very fast timescales (millisecond-second) and that most of the deformation takes place within the first few seconds of force application. These results have also demonstrated the interplay between nuclear and cytoskeletal prestress in governing the mechanical response of the nucleus to external mechanical forces. Performing parallel experiments on suspended cells of the same type, which were confirmed to exhibit an extensively different CSK morphology, verified that the CSK plays a significant role in transferring mechanical signals to the cell nucleus. Subsequently employing a combination of anti-cytoskeletal inhibitors then allowed me to specifically probe the influence of actin and MTs on the mechanical properties of nuclei inside the cell, as opposed to isolating them from the sub-cellular environment.

The results of this work demonstrate several important physical properties of the nucleus in NIH3T3 fibroblast cells. Most importantly, the nucleus displays a distinct mechanical anisotropy (α; defined in equation 37) along its major and minor axes. An external force applied to the center of the nucleus causes strain along the minor axis ($\varepsilon_{p,minor}$) which was observed to be ~2.5 times larger than that along the major axis ($\varepsilon_{p,major}$). Values of α are consistent with the

change in ellipticity (χ; defined in equation 35), which indicate that the nucleus becomes less elliptical in response to force.

Both α and χ are independent of the magnitude of the applied force and the drug treatment conditions. This indicates that the properties that govern the change in nuclear shape are independent of the cytoskeleton. Moreover, the characteristic deformation rate ($\kappa \approx 5\ s^{-1}$) is also independent of both the magnitude of the applied force and the drug treatment conditions. These results suggest that the rate of nuclear shape change and characteristics of nuclear shape are intrinsic to the nucleus itself and independent of the cytoskeleton, which is consistent with previous work (Mazumder & Shivashankar 2010).

On the other hand, the magnitude of nuclear deformation ($\varepsilon_{p,major}$ and $\varepsilon_{p,minor}$) is clearly governed by the cytoskeleton. The loss of actin, MTs, or both actin and MTs alters the strain magnitude in response to force, which is reflected in the elastic modulus (ξ) of the nucleus. Depolymerization of actin filaments, whether alone or in combination with the depolymerization of MT filaments, causes the nucleus to deform significantly more than in untreated cells with both filament systems intact. Values obtained for the effective moduli (defined in equation 41) indicate that the nuclear ξ decreases by a factor of ~0.7 relative to untreated cells. This result is unsurprising as the actin network is known to impart mechanical strength to living cells. It is also highly cross-linked to the nuclear architecture through nesprin-1 and -2 proteins (Dahl, Ribeiro et al. 2008; Dahl & Kalinowski 2011), and actin cytoskeletal prestress has been known to result in strain hardening (Stamenović & Wang 2000; Zhou, Shen et al. 2011).

Surprisingly, the effective long-time elastic modulus (ξ_{eff}) values of the nucleus indicate that the loss of MTs causes it to become ~3 times stiffer than in untreated cells. In this limit, the loss of MTs will likely enhance the prestress due to actin (Stamenović & Wang 2000), resulting in larger moduli in the case that pre-stress causes strain hardening. However, treatment with nocodazole was also shown to cause an increase in nuclear size, and the results may represent an upper limit on the ability of a 10nN or 20nN applied force to cause significant deformation. Therefore, as $\varepsilon_{p,major}$ is at most ≈ 1%, the nuclei in cells lacking MTs display an upper extreme in the compliance of the major axis.

7.2 Deformation Anisotropy is governed by the CSK as well as Intrinsic Nuclear Properties

Micropipette aspiration has been a popular approach for studying the role of various nucleoskeleton and nuclear envelope proteins in governing the mechanical properties of the nucleus. Importantly, in many of these studies, the nucleus is removed from the cell and studied in isolation from the cytoskeleton in order to assess its intrinsic mechanical properties (Dahl, Kahn et al. 2004; Dahl, Engler et al. 2005; Lammerding, Dahl et al. 2007; Pajerowski, Dahl et al. 2007). However, a recent study on nuclei left within the cell demonstrated a clear anisotropic response to laser ablation induced damage (Mazumder & Shivashankar 2010). Destroying heterochromatin nodes in the nuclei of differentiated fibroblasts and pluripotent embryonic stem cells resulted in anisotropic shrinkage of the nucleus, with the minor axis contracting more drastically than the major axis. The study also demonstrated that disruption of cytoskeletal filaments significantly affected nuclear morphology, with depolymerization of actin filaments leading to a reduction in nuclear size, but depolymerization of microtubules causing nuclei to enlarge (Mazumder & Shivashankar 2010). These results suggest that force-induced nuclear deformation observed within an intact cell is not intrinsically isotropic, and that its mechanical behavior may be regulated by the surrounding cytoskeleton.

It has been proposed that anisotropy in global cellular deformation is dominated by the presence of actin fibers, which tend to align parallel to the long axis of the cell (Heggeness, Wang et al. 1977). The results of this thesis strongly suggest this to be the case for nuclear deformation as well, as the major axis tended to align with the polarization of the actin cytoskeleton (as seen in Fig. 4.1a, Fig. 5.1a, and Fig. 5.1c). However, after treatment with CytD-Noco one would therefore expect the nucleus to expand isotropically under applied force, which was not the case. These results suggest the existence of an intrinsically prestressed nucleus due to the nucleoskeleton, nuclear envelope and/or chromatin organization (Dahl, Ribeiro et al. 2008; Dahl & Kalinowski 2011). This in turn implies that models which treat the nucleus as a uniform material with self-contained and isotropic mechanical properties (Guilak, Tedrow et al. 2000; Dahl, Engler et al. 2005; Vaziri, Lee et al. 2006) independent of the rest of the cell are clearly incomplete.

7.3 The Nucleus Maintains Structural Integrity under Cyclic Force

The results of the cycling experiments conducted in Chapter 6 show how the characteristic deformation behavior exhibited by the nucleus under static force application still persisted even under repeated (cyclic) force application. Given a specific drug treatment and magnitude of applied force, the nucleus tended to exhibit the same degree of deformation for each cycle. Furthermore, it was shown to return to its original size after each force application, with all measurements of the change in normalized area or strain found to be independent of cycle number.

These results, taken together with the fact that no significant change in nuclear shape or size was observed throughout the duration of the cycling experiment (225 seconds = 3.75 minutes) in the absence of applied force would suggest a characteristic timescale of remodelling of the nuclear lamina that is significantly greater than this time period. Indeed, previous studies employing fluorescence recovery after photobleaching (FRAP) have confirmed this to be the case (Moir, Yoon et al. 2000; Goldman, Gruenbaum et al. 2002; Gilchrist, Gilbert et al. 2005). By photobleaching and then subsequently tracking the fluorescence emission of GFP-lamin A within the lamina of embryonic mouse epidermal cells, these studies showed that lamina fluorescence recovers on a timescale of about 90 minutes during the first period of interphase, with this timescale increasing for other stages of interphase (Moir, Yoon et al. 2000; Goldman, Gruenbaum et al. 2002). Similar results were also observed in human fibrosarcoma cells, with FRAP indicating immobile lamins at the nuclear periphery and slow-moving lamins within the lamina exhibiting a characteristic timescale of around 145 minutes (Gilchrist, Gilbert et al. 2005). This slow kinetics of A-type lamins suggests that the nuclear lamins form very stable structures, both in the periphery of the nucleus as well as throughout the nucleoplasm (Goldman, Gruenbaum et al. 2002).

Furthermore, while the intermediate filaments (IFs) seem to play no role in governing the deformation dynamics of the nucleus, there is reason to believe that they may be acting to maintain nuclear integrity. The observation of force-dependent nuclear deformation in CytD-

Noco treated cells confirms that the intermediate filament network alone is sufficient to transmit mechanical stress to the nucleus (Maniotis, Chen et al. 1997). The fact that this data is not significantly different from the CytD treatments suggests that IFs do not directly influence the magnitude of nuclear deformation under applied force. However, IFs exhibit unusual viscoelastic properties not shared by either actin or tubulin. In particular, vimentin networks, while less rigid at low strains, have been found to harden at high strains and resist breakage (Janmey, Euteneuer et al. 1991, Kreplak & Fudge 2007; Wang & Pelling 2011). This mechanical resilience makes the IF network an excellent candidate for maintaining cellular integrity (Ackbarow, Sen et al. 2009; Wang & Pelling 2011). Moreover, vimentin filament kinetics are dominated by the rate at which the longest filaments reorganize to relieve stress, thus exhibiting long characteristic timescales (around 166 minutes) similar to those of A-type lamins (Janmey, Euteneuer et al. 1991). This suggests that the nuclear lamins, as well as the cytoskeletal IF network, may be imparting a structural plasticity to the nucleus, which is evident in its mechanical response to external cyclic force.

Most studies exploring the response of cells and cellular components to external cyclic force observe results after very long durations, with typical cycling experiments lasting on the order of days. For example, cyclic tensional deformation applied to porcine smooth muscle cells (SMCs) resulted in enhanced collagen production, a change in preferential alignment, and an overall decrease in SMC proliferation that became significant after several days (Sumpio & Banes 1988; Sumpio, Banes et al. 1988). Decreased cell proliferation was also observed in osteoblast cells under cyclic pressure, but only under specific frequencies and durations (Nagatomi, Arulanandam et al. 2001). Still, the lack of a significant change in the mechanical response of the nucleus to cyclic force within 225 seconds does not seem to be entirely due to the timescale of the experiment. The response of the cell membrane to cyclic force on a similar timescale, for example, was investigated in a recent study (Watanabe-Nakayama, Machida et al. 2011) that employed AFM to apply a local cyclic stretching force onto the surface of single rat fibroblasts. The aforementioned study found that the strain magnitude tended to decrease significantly with increasing stretch cycles, concurrent with a local increase in membrane stiffness after every cycle (Watanabe-Nakayama, Machida et al. 2011). Moreover, in an earlier study, actin stress fibers in human endothelial cells subjected to cyclic strain were found to re-

align perpendicular to the force vector within minutes of initiation of cyclic strain (Iba & Sumpio, 1991). On the other hand, the findings in Chapter 6 indicate that the change in projected nuclear area (ΔArea), plateau strain along both axes of the nucleus ($\varepsilon_{p,major}$ and $\varepsilon_{p,minor}$) and the nuclear anisotropy α are all independent of the cycle number, for each treatment condition and magnitude of applied force. These results agree with those of the optical stretcher experiments in showing that, while they are not necessarily independent of each other, the mechanical response of the nucleus is distinct from that of the cell as a whole.

7.4 Implications and Future Work

The findings of this thesis have consistently shown that the nucleus expands anisotropically in response to an external force applied with the AFM. This anisotropy was observed regardless of the magnitude of applied force and, in the case of cycling experiments, regardless of the cycle number as well. Also, the degree of nuclear anisotropy did not vary significantly after depolymerizing specific components of the CSK, although this did have an effect on the magnitude of deformation.

Interestingly though, this nuclear anisotropy may be related to the CSK in another way. Each of the CSK filament systems is composed of an elaborate network of fibers distributed throughout the cell. Measurements made of the deformation of any particular component of the CSK tend to display more variance and heterogeneity than those of single, comparatively self-contained nuclei (Helmke & Davies, 2002; Hu, Chen et al. 2003; Walcott & Sun 2010; Hakari, Sekiguchi et al. 2011; Guolla, Bertrand et al. 2012; Wang & Pelling 2012). However, the CSK also exhibits complex remodelling and deformation behavior, as well as anisotropy in response to applied force (Hu, Chen et al. 2003; Hakari, Sekiguchi et al. 2011; Guolla, Bertrand et al. 2012; Wang & Pelling 2012). Actin stress fiber deformation occurs not in an isotropic fashion but rather in localized regions, with long-term forces causing actin filaments to aggregate and orient parallel to the direction of force application (Walcott & Sun 2010; Guolla, Bertrand et al. 2012). IFs, as well, tended to deform in regions focused away from the central longitudinal axis of the cell (Wang & Pelling 2012). Stiffness measurements performed on

adherent cells also showed that mechanical stiffness transverse to the long axis of those cells was less than half that parallel to the long axis (Hu, Eberhard et al. 2004). Taken together, these observations suggest that perhaps the nuclear deformation anisotropy established in this thesis is just one aspect of a more general mechanical anisotropy exhibited by the cell as a whole.

In order to investigate if the anisotropic deformation of the nucleus is conserved among diverse differentiated cell types, I also performed the experiments on several cell types that range in function (fibroblast, myoblast and epithelial) and species type (mouse, human, canine). Specifically, I cultured and prepared mouse C2C12 myoblast cells (Yaffe & Saxel 1977), human HeLa epithelial cells (Masters 2002) and canine MDCK epithelial cells (Gaush, Hard et al. 1966) under identical conditions as the NIH3T3 cells (discussed in Section 3.1). I then exposed cells of each type to a 10nN force under the AFM for 5 seconds, using imaging conditions identical to those employed for the cyclic and short-term static experiments. Although the average strain magnitudes varied between the cell types, the strain anisotropy between the major and minor axes was indeed conserved, as seen in Figure 7.1:

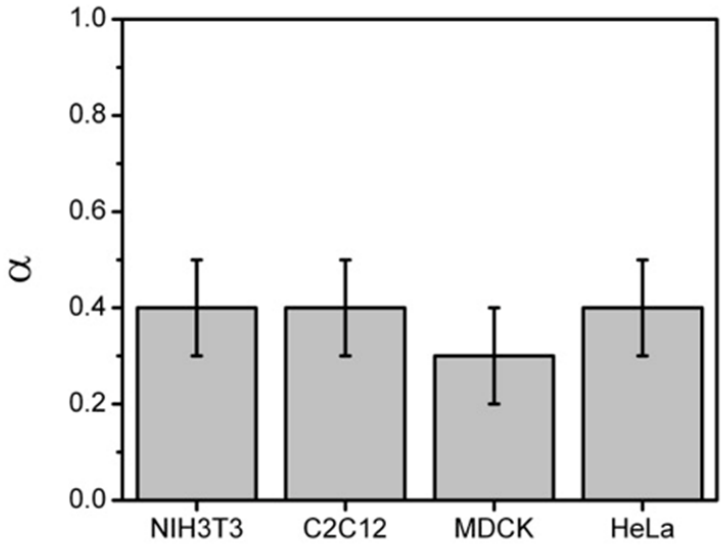

Figure 7.1. Deformation anisotropy (α) determined for different cell types. The experiment was repeated on a total of four cell types from different species in order to determine α under a 10nN load over 5 seconds: mouse NIH3T3 fibroblasts (α = 0.4 ± 0.1), mouse C2C12 muscle myoblasts (α = 0.4 ± 0.1), canine MDCK epithelial (α = 0.3 ± 0.1) and human HeLa epithelial cells (α = 0.4 ± 0.1). In all cases α is very similar, indicating that the mechanical anisotropy of the nucleus is conserved among mammalian cell and species types.

The plot of α values above confirms that while each of these cell types came from different species with vastly different functions, all of them have very similar nuclear properties, particularly nuclear anisotropy. Therefore, nuclear mechanical anisotropy appears to be highly conserved among differentiated cells, although the biological function of such anisotropy is not understood. While speculative, this anisotropy may play a significant role in chromatin organization and possibly force-induced chromatin remodelling, conformational changes and gene expression.

Future work will involve further investigations of the mechanical response of the nucleus to cyclic force. Cycling experiments involve several key parameters that can be set in a variety of ways; the most important of these are the force duration, the 'resting' period duration, and the length of the experiment itself. It would be interesting to see if the nucleus displays the same resilience even after a greatly increased number of cycles or longer force applications. Another aspect worth investigating is the effect of inhibiting vimentin expression on nuclear deformation, particularly under cyclic force. As previously stated, the deformation behavior of the nucleus observed in cycling experiments taken together with the known viscoelastic properties of vimentin filaments strongly suggests that the IF network imparts mechanical plasticity to the nucleus, shielding it from any significantly irreversible deformation on the timescale of the cycling experiments. A follow-up study employing RNA interference in order to inhibit vimentin expression (Tsuruta & Jones 2003) prior to force application is certainly worth undertaking.

The role of extracellular mechanical forces and the mechanical properties of the microenvironment are now recognized as critical regulators of many aspects of cell biology. Indeed, it is becoming clear that the physical properties of the nucleus are not simply a by-product of molecular biology, but are crucial to the normal functioning of the cell in many physiological processes. While the response of cell nuclei to external force is certainly complex, the results presented in this thesis have established that the nucleus exhibits a characteristic mechanical anisotropy that persists even after repeated loading. This thesis has also shown that nuclear anisotropy is conserved among cell types spanning a broad range of functions and species, and involves a clear interplay between nuclear and cytoskeletal prestress.

7.5 References

Ackbarow, T., D. Sen et al. (2009). "Alpha-helical protein networks are self-protective and flaw-tolerant." PLoS One **4**(6): Article ID e6015.

Dahl, K.N., A. Engler et al. (2005). "Power law rheology of isolated nuclei with deformation mapping of nuclear sub-structures." Biophys J **89**: 2855-2864.

Dahl, K.N., S. M. Kahn et al. (2004). "The nuclear envelope lamina network has elasticity and a compressibility limit suggestive of a molecular shock absorber." J Cell Sci **117**: 4779-4786.

Dahl, K.N. and A. Kalinowski (2011). "Nucleoskeleton mechanics at a glance." J Cell Sci **124**: 675-678.

Dahl, K.N., A.J.S. Ribeiro et al. (2008). "Nuclear Shape, Mechanics, and Mechanotransduction." Circ Res **102**: 1307-1318.

Gaush, C.R., W.L. Hard et al. (1966). "Characterization of an Established Line of Canine Kidney Cells (MDCK)." Exp Biol Med **122**(3): 931-935.

Gilchrist, S., N. GIlbert et al. (2005). "Altered protein dynamics of disease-associated lamin A mutants." BMC Cell Biology **5**: 46-54.

Goldman, R.D., Y. Gruenbaum et al. (2002). "Nuclear lamins: building blocks of nuclear architecture." Genes & Dev **16**: 533-547.

Guilak, F., J.R. Tedrow et al. (2000). "Viscoelastic Properties of the Cell Nucleus." Biochem Biophys Res Commun **269**(3), 781-786.

Guolla, Bertrand et al. (2012). "Force transduction and strain dynamics in actin stress fibres in response to nanonewton forces." J Cell Sci **125**: 603-613.

Hakari, T., H. Sekiguchi et al. (2011). "Nonlinear displacement of ventral stress fibers under externally applied lateral force by an atomic force microscope." Cytoskeleton **68**(11): 628-638.

Heggeness, M. H., K. Wang et al. (1977). "Intracellular distributions of mechanochemical proteins in cultured fibroblasts." Proc Natl Acad Sci USA **74**(9): 3883-3887.

Helmke, B.P. and P.F. Davies (2002). "The Cytoskeleton Under External Fluid Mechanical Forces: Hemodynamic Forces Acting on the Endothelium." Ann Biomed Eng **30**(3): 284-296.

Hu, S., J. Chen et al. (2003). "Intracellular stress tomography reveals stress focusing and structural anisotropy in cytoskeleton of living cells." Am J Physiol Cell Physiol **285**: C1082-C1090.

Hu, S., L. Eberhard et al. (2004). "Mechanical anisotropy of adherent cells probed by a three-dimensional magnetic twisting device." Am J Physiol Cell Physiol **287**: C1184-C1191.

Iba, T. and B.E. Sumpio (1991). "Morphological Response of Human Endothelial Cells Subjected to Cyclic Strain in Vitro." Microvascular Research **42**: 245-254.

Janmey, P.A., U. Euteneuer et al. (1991). "Viscoelastic Properties of Vimentin Compared with Other Filamentous Biopolymer Networks." J Cell Biol **113**: 155-160.

Kreplak, L. and D. Fudge. "Biomechanical properties of intermediate filaments: from tissues to single filaments and back." BioEssays **29**(1): 26-35.

Lammerding, J., K.N. Dahl et al. (2007). "Nuclear Mechanics and Methods." Method Cell Biol **83**: 269-294.

Maniotis, A.J., C.S. Chen et al. (1997). "Demonstration of mechanical connections between integrins, cytoskeletal filaments, and nucleoplasm that stabilize nuclear structure." Proc Natl Acad Sci USA **94**: 849-854.

Masters, J.R. (2002). "HeLa cells 50 years on: the good, the bad and the ugly." Nat Rev Cancer **2**(4): 315-319.

Mazumder, A. and G. Shivashankar (2010). "Emergence of a prestressed eukaryotic nucleus during cellular differentiation and development." J R Soc Interface **7**: S321-S330.

Moir, R.D., M. Yoon et al. (2000). "Nuclear Lamins A and B1. Different pathways of assembly during nuclear envelope formation in living cells." J Cell Biol **151**: 1155-1168.

Nagatomi, J., B.P. Arulanandam, et al. (2001). "Frequency- and Duration-Dependent Effects of Cyclic Pressure on Select Bone Cell Functions." Tissue Eng **7**(6): 717-728.

Pajerowski, J. D., K.N. Dahl et al. (2007). "Physical plasticity of the nucleus in stem cell differentiation." Proc Natl Acad Sci USA **104**: 15619-15624.

Stamenović, D. and N. Wang (2000). "Engineering approaches to cytoskeletal mechanics." J Appl Physiol **89**: 2085-2090.

Sumpio, B.E. and A.J. Banes (1988). "Response of porcine aortic smooth muscle cells to cyclic tensional deformation in culture." J Surg Res **44**(6): 696-701.

Sumpio, B.E., A.J. Banes et al. (1988). "Enhanced Collagen Production by Smooth Muscle Cells During Repetitive Mechanical Stretching." Arch Surg **123**(10): 1233-1236.

Tsuruta, D. and J.C.R. Jones (2003). "The vimentin cytoskeleton regulates focal contact size and adhesion of endothelial cells subjected to shear stress." J Cell Sci **116**: 4977-4984.

Vaziri, A., H. Lee et al. (2006). "Deformation of the cell nucleus under indentation: Mechanics and mechanisms." J Mater Res **21**(8), 2126-2135.

Walcott, S. and S.X. Sun (2010). "A mechanical model of actin stress fiber formation and substrate elasticity sensing in adherent cells." Proc Natl Acad Sci USA **107**(17): 7757-7762.

Wang, J. and A.E. Pelling (2012). "An Approach to Visualize the Deformation of the Intermediate Filament Cytoskeleton in Response to Locally Applied Forces." ISRN Cell Biology **2012**: Article ID 513546.

Watanabe-Nakayama, T., S. Machida et al. (2011). "Direct Detection of Cellular Adaptation to Local Cyclic Stretching at the Single Cell Level by Atomic Force Microscopy." Biophys J **100**: 564-572.

Wu, H.W., T. Kuhn et al. (1998). "Mechanical Properties of L929 Cells Measured by Atomic Force Microscopy: Effects of Anticytoskeletal Drugs and Membrane Crosslinking." Scanning **20**(5): 389-397.

Yaffe, D. and O. Saxel (1977). "Serial passaging and differentiation of myogenic cells isolated from dystrophic mouse muscle." Nature **270**(5639): 725-727.

Zhou, X.Z., H.Shen et al. (2011). "Bio-optimum prestress in actin filaments with a polygonal cytoskeleton model." Arch Appl Mech **81**: 1651-1658.

Appendix A:

ImageJ Macro for Nuclear Deformation Analysis

*/*This macro loads DAPI (blue) channel XY-T videos of nuclear deformation (XYZT hyperstacks must be Z-projected prior to running this macro). The image in each timeframe is thresholded as per user input entered in the "Find Maxima" dialog box. The edge of the nucleus is detected, and measurements are taken for each successive frame according to the parameters last defined in the "Set Measurements" command: at the very least, "Area" and "Fit Ellipse" must be included, although "Shape Descriptors" and "Centroid" also give useful information.*

*Written by Joan Karla Macadangdang, University of Ottawa */*

```
setSlice(1);

Dialog.create("Find Maxima");
Dialog.addNumber("Noise Tolerance:", 3500);
Dialog.addChoice("Output Type:", newArray("Maxima Within Tolerance", "Single Points",
"Segmented Particles", "Count"));
Dialog.addCheckbox("Exclude Edge Maxima", false);
Dialog.addCheckbox("Light Background", false);
Dialog.show();

tolerance = Dialog.getNumber();
type = Dialog.getChoice();
exclude = Dialog.getCheckbox();
light = Dialog.getCheckbox();
options = "";
if (exclude) options = options + " exclude";
if (light) options = options + " light";
```

*/*These values correspond to user input for thresholding. The important values to change are "Noise Tolerance" (will vary depending on the image) and "Light Background" (changing this is not as critical, but sometimes eases work with inverted image maxima without affecting results). For the purposes of this thesis, all other options are left to their default values.*/*

```
setBatchMode(true);
input = getImageID();
n = nSlices();

for (i=1; i<=n; i++)
{
        showProgress(i, n);
        selectImage(input);
```

```
	setSlice(i);
	run("Find Maxima...", "noise="+ tolerance +" output=["+type+"]"+options);

	if (i==1) output = getImageID();
	else if (type!="Count")
	{
		run("Select All");
		run("Copy");
		close();
		selectImage(output);
		run("Add Slice");
		run("Paste");

	}

}

run("Select None");
setBatchMode(false);

waitForUser("Click OK to continue");

/*This serves as a checkpoint to make sure that the resulting stack of maxima is satisfactory.
This becomes especially important for very large stacks (~3000 frames). Acknowledge to
proceed to measurements; otherwise, abort the macro.*/

var x=0; var y=0;
setSlice(1);

for (j=0; j<nSlices; j++)
{
	doWand(x, y);
	getStatistics(area);
	x=0; y=0;

	while (area>500 || area <20)
	//Projected nuclear areas usually range between 80-300 sq. um.
	{
		x=x+3;
		y=y+3;
		doWand(x, y);
		getStatistics(area);
	}

/*This takes the cursor from x=0, y=0 down a diagonal line, taking test area measurements
every 3 pixels until it makes a measurement in the desired range. Increments for x and y can be
adjusted for speed, or in the rare cases where the nucleus is severely off-center in the image.*/
```

```
run("Measure");
roiManager("Add");
setOption("Show All");
run("Next Slice [>]");
}
```

*/*User-defined measurements are taken of the selection defined upon exit of the previously nested "while" loop. This is done for every frame in the stack, with each row of measurements in the "Results" window corresponding to those taken for an individual frame.*/*

```
print("All done!");
run("Close");
```

Appendix B:

LabVIEW Block Diagram of Optical Stretching Program

Below is the block diagram representing the optical stretching program built in the National Instruments LabVIEW development environment. Note that this program requires the NI Image Acquisition Software (NI-IMAQ) module to be installed beforehand. Key structures and parameters are defined in the following page.

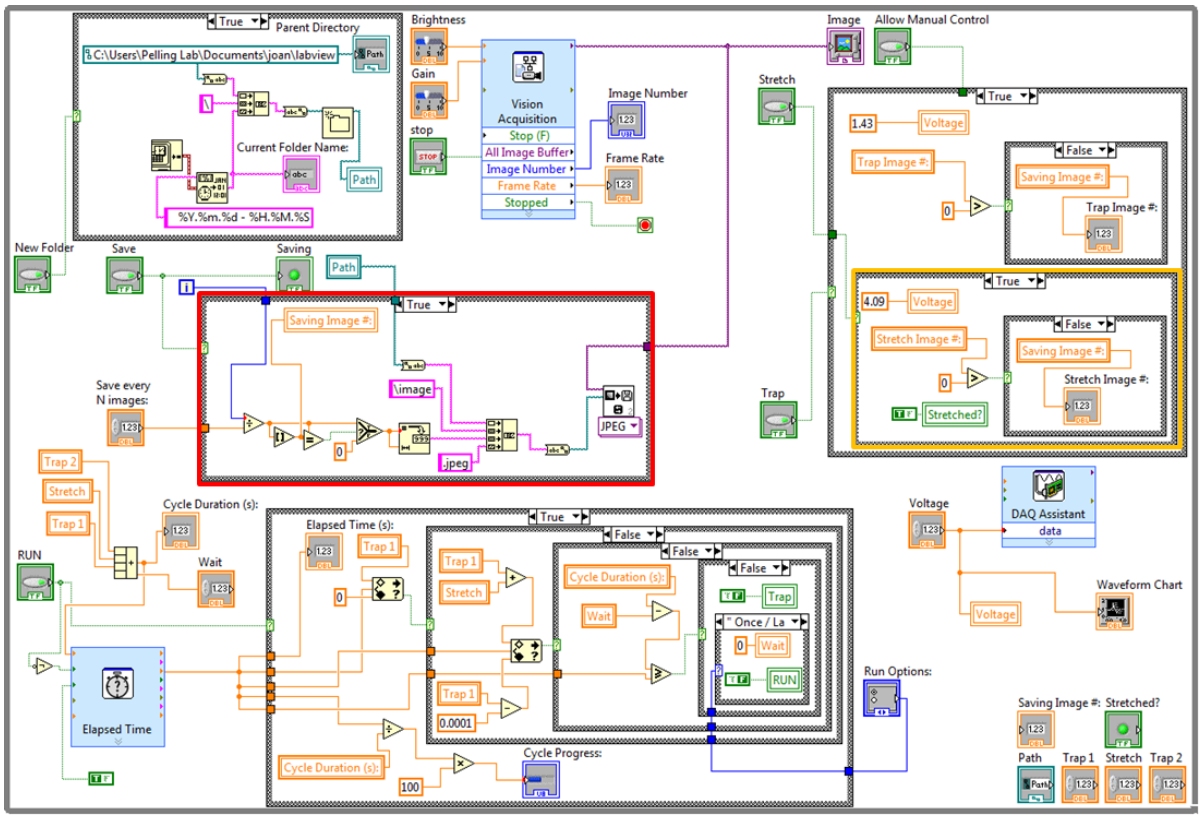

Alternative case structures (all other such structures within the block diagram are either empty or non-critical):

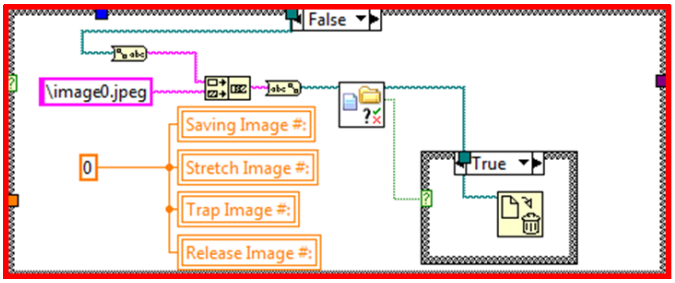

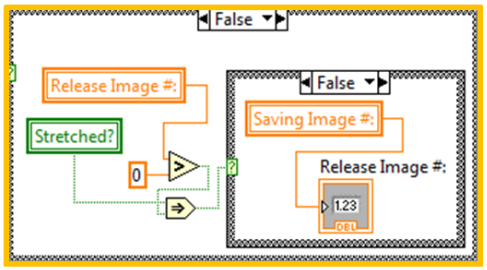

virtual instrument (VI): acquires the image stream from the camera. Frames are grabbed continuously at ~15 frames per second and updated on the display until the VI is stopped. Stopping image acquisition terminates the program.

virtual instrument (VI): enables control of the laser power by providing analog output signals that define the voltage of the laser (see: "Voltage").

boolean: initial value = **false**. When **true**, stops image acquisition.

boolean: initial value = **false**. When **true**, creates a new directory into which subsequent saved images are stored. "New Folder" reverts to **false** upon creation of the directory.

boolean: initial value = **false**. When **true**, saves all frames acquired through "Vision Acquisition" into the newest active directory until "Save" is set to **false**.

integer: initial value = 1. If set to a value > 1 and "Save" = **true**, the program saves only frames with "Image Number" that are a multiple of this value as distinct image files, with all others continuously overwritten and discarded.

double: initial value = 0.0. This represents the output voltage of the laser, which determines the output power as per laser calibration data in Fig. 3.4.

boolean: initial value = **false**. When **true**, sets the output power of the laser to the preset trapping power. This command overrides whatever previous value of the voltage was set even after toggling "Allow Manual Control".

boolean: initial value = **false**. When **true**, sets the output power of the laser to the preset stretching power. This command automatically sets "Trap" to **true** if initially **false**. This command also overrides whatever previous value of the voltage was set even after toggling "Allow Manual Control".

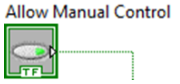

boolean: initial value = **false**. When **true**, permits the user to set the voltage to any value between 0.0 and 10.0. Otherwise, "Voltage" remains locked at 0.0 unless "Trap" or "Stretch" is **true**.

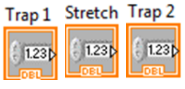

double: initial values = 0.0. Values are dependent on user input and correspond to initial trapping, stretching, and final trapping durations (in seconds) for automated stretching routines (see: "RUN").

boolean: initial value = **false**. When **true**, performs successive trapping, stretching, and trapping routines as defined by "Run Options" (either once, or continuously). Routines are performed precisely according to the lengths of time previously defined in "Trap 1", "Stretch" and "Trap 2".

Appendix C:

Permission to Use Figures

SPRINGER LICENSE
TERMS AND CONDITIONS

Mar 27, 2012

This is a License Agreement between Joan Karla Macadangdang ("You") and Springer ("Springer") provided by Copyright Clearance Center ("CCC"). The license consists of your order details, the terms and conditions provided by Springer, and the payment terms and conditions.

License Number	2877350086485
License date	Mar 27, 2012
Licensed content publisher	Springer
Licensed content publication	Pflügers Archiv
Licensed content title	Nuclear pore function viewed with atomic force microscopy
Licensed content author	T. Danker
Licensed content date	Mar 1, 2000
Volume number	439
Issue number	6
Type of Use	Thesis/Dissertation
Portion	Figures
Author of this Springer article	No
Order reference number	n/a
Title of your thesis / dissertation	Nuclear and Cytoskeletal Prestress Govern the Anisotropic Mechanical Properties of the Nucleus
Expected completion date	Apr 2012
Estimated size(pages)	130
Total	0.00 CAD

Terms and Conditions
Gratis licenses (referencing $0 in the Total field) are free. Please retain this printable license for your reference. No payment is required.

ELSEVIER LICENSE
TERMS AND CONDITIONS

Mar 30, 2012

This is a License Agreement between Joan Karla Macadangdang ("You") and Elsevier ("Elsevier") provided by Copyright Clearance Center ("CCC"). The license consists of your order details, the terms and conditions provided by Springer, and the payment terms and conditions.

Supplier	Elsevier Limited The Boulevard,Langford Lane Kidlington,Oxford,OX5 1GB,UK
Registered Company Number	1982084
Customer name	Joan Karla Macadangdang
Customer address	Room 338E Macdonald Hall Ottawa, ON K1N6N5
License Number	2878961219882
License date	Mar 30, 2012
Licensed content publisher	Elsevier
Licensed content publication	Biophysical Journal
Licensed content title	Power-Law Rheology of Isolated Nuclei with Deformation Mapping of Nuclear Substructures
Licensed content author	Kris Noel Dahl, Adam J. Engler, J. David Pajerowski, Dennis E. Discher
Licensed content date	October 2005
Licensed content volume number	89
Licensed content issue number	4
Number of Pages	10
Start Page	2855
End Page	2864
Type of Use	reuse in a thesis/dissertation
Intended publisher of new work	other
Portion	figures/tables/illustrations
# of figures/tables/illustrations	1
Format	both print and electronic
Author of this Elsevier article	No
Translating	No
Order reference number	n/a

Title of your thesis/dissertation	Nuclear and Cytoskeletal Prestress Govern the Anisotropic Mechanical Properties of the Nucleus
Expected completion date	Apr 2012
Estimated size(pages)	130
Elsevier VAT number	GB 494 6272 12
Total	0.00 USD

Terms and Conditions

Gratis licenses (referencing $0 in the Total field) are free. Please retain this printable license for your reference. No payment is required.

Appendix D:

Statistical Analysis

Given the nature of the experiments conducted for the purposes of this thesis, it was not possible to perform measurements on each member of the *population* (e.g. tracking the nuclear deformation in response to a particular force of all the cells under a particular drug treatment). Instead, I took representative *samples* (i.e. *n* = 12 cells for nuclei observed over 15 min, under 10nN of force from the AFM) and analyzed only the data produced from these samples. As is the case in general, employing proper statistical techniques enables us to use sample data in order to make broader conclusions that apply to the population about any trends observed.

Descriptive Statistics

Before we attempt to make any claims about the population, we first need to study our sample data and summarize it in such a way as to extract the most useful information it provides. The two main quantities of interest pertaining to descriptive statistics are the mean ($\bar{x}$) and the standard deviation (σ_x ; not to be confused with σ, which has been used to represent stress thus far).

The mean is simply the arithmetic average of a set of values, in this case obtained from the sample data:

$$\bar{x} = \frac{1}{n} \cdot \sum_{i=1}^{n} x_i \quad [43]$$

where each x_i corresponds to an observed value or measurement, and *n* is the total number of such measurements, also called the sample size. This formula holds for entire populations as well: if a population is composed of *n* members, then $\bar{x}$ becomes the population mean. The mean is a measure of central tendency: given a finite sample (or population) of size *n*, the quantitative data values tend to cluster around a certain value, and in either case that value is the mean (Dodge 2003).

The mean itself alone, however, tells us nothing about the statistical dispersion, or the 'spread' in the data. One can have one population with diverse data and another composed of

only identical values, but still have the same population means. The standard deviation is a useful measure of the statistical dispersion of a given population, and has the formula:

$$\sigma_x = \sqrt{\frac{\sum_{i=1}^{n}(x_i - \bar{x})^2}{n}} \quad [44]$$

In general, the standard deviation expresses how much variation there is from the mean. The lower the standard deviation, the closer individual data points will be to the mean in a given population. Conversely, the higher the standard deviation, the more these data points will tend to be spread out over a large range of values.

A subtle but important point to note is that the formula in Equation 44 yields the standard deviation of the *population*: σ_x becomes meaningful if we assume that $x_1, x_2, \ldots, x_n$ describe all *n* data values from the population. Moreover, this would require that we know the population mean $\bar{x}$, which we can only compute directly if every member of the population can be observed and measured. For all other cases, we examine a sample of the population and estimate σ_x using the *sample* standard deviation, *s*:

$$s = \sqrt{\frac{\sum_{i=1}^{n}(x_i - \bar{x})^2}{n-1}} \quad [45]$$

where the replacement of the denominator *n* by *n-1* is known as Bessel's correction. In simplest terms, this correction can be understood intuitively by taking n=1: for a sample containing only one data point, there would be no variation around the mean, and thus the standard deviation would be undefined.

As with σ_x, the sample standard deviation *s* gives an estimate of the typical difference between the data points and the sample mean. For a normal distribution, about 68% of the sample data points will lie within the region of $\bar{x} \pm s$, while around 95% of the data points will be within $\bar{x} \pm 2s$ (Cumming, Fidler et al. 2007).

The Standard Error of the Mean

So far, the mean and standard deviation give us useful information about our chosen sample of the population. The sample mean also provides us with an estimate of the population mean, given enough sample elements n. However, if we want to say anything about the

population, we need a measure of how good an estimate our calculated sample mean is of the actual population mean. This can be done by calculating the standard error of the mean (SEM): if we were to take multiple samples and repeat the same measurements each time, obtaining several sample mean values, the standard deviation about the mean of these sample means would be the SEM. It is thus the standard deviation of the sample mean's estimate of the population mean.

There is a way to estimate the SEM by taking the sample standard deviation and dividing it by the square root of the sample size:

$$SEM = \frac{s}{\sqrt{n}} \quad [46]$$

The standard error of the mean, therefore, allows us to make inferences from the sample data. By plotting the sample mean as a data point with the corresponding $\pm$SEM value as error bars, as I have done in this thesis, we are making an estimate of the mean of the whole possible set of results, instead of simply reporting variation in the sample data as with $\bar{x} \pm s$. The error bars set by the SEM define the interval containing values that are most plausible for this population mean (Cumming, Fidler et al. 2007).

Choosing the Sample Size

It is clear from Equation 46 that the sample size *n* affects the accuracy in estimating the population mean. As the sample size is increased, the SEM shrinks, and the sample mean will tend to get closer and closer to the true population mean. As $n \to \infty$, after all, the chosen sample will more and more closely approximate the entire population. At a first glance, then, it seems appropriate to simply have a sample that is as large as possible.

There is, however, an issue of practicality that needs to be addressed when choosing the sample size. Since the accuracy of the population mean estimate falls off as the square root of *n*, increasing the sample size has a diminishing effect the higher *n* already is. Furthermore, the underestimate of the SEM in the population standard error falls off rather quickly with an increase in *n*: a sample size of *n*=2 leads to an underestimate of 25%, but this drops to only 5% for *n*=6 (Gurland & Tripathi 1971).

In experimental biology, one often has to compare samples between two groups (i.e. nuclei that had been indented with 10nN of force, versus those with 20nN), to see if they are different (Cumming, Fidler et al. 2007). One can qualitatively compare two sets of results by plotting the mean $\pm$SEM values for both samples and looking at the overlap in the error bars: the smaller the overlap of these bars (or, the larger the gap between them), the more evidence there is that these two samples are truly different (Cumming & Finch 2005).

It stands to reason then that it is not so much a matter of *n* being as large as possible, but rather being large *enough*. In fact, having a sample size as small as *n*=3 is a convention in experimental biology research (Cumming, Fidler et al. 2007) as long as the results yield good statistics (Conlon, Dunn et al. 2001; Dahl, Engler et al. 2005; Thomas, Calaminus et al. 2007; Kretlow, Jin et al. 2008; Asumda & Chase 2011; Bouland, Kural et al. 2011). The sample sizes chosen for the experiments performed in this thesis (*n*=3 for control cells, and *n*=10-12 for all others) were more than sufficient for this purpose.

Statistical Significance Tests

Of course, a more rigorous method of analyzing data is needed before one can confidently say that any two samples are truly different. In order to quantify how meaningfully different two samples are, we perform statistical significance tests on the sample data sets. Formally, these tests aim to reveal whether or not we can reject the *null hypothesis*, a 'default' position that asserts an experimental variable has no effect (i.e. 'Treatment with nocodazole does not affect nuclear size.')

Carrying out such a test first requires a *test statistic*, a function of the sample that summarizes the data in such a way that it can be reduced into a single value (or set of values) that can be then used for statistical significance testing (Berger & Casella 2001). In this thesis, the test used to check for statistical significance was the paired Student's t-test, in which the test statistic is *t*:

$$t = \frac{\sum d}{\sqrt{\frac{n(\sum d^2) - (\sum d)^2}{n-1}}} \quad [47]$$

Here, d refers to the differences between the pairs of variables in the two samples. The resulting value, t, grows larger as the difference between the means of two samples grows larger.

A t-value can then be converted into a p-value, which is how I have chosen to quote the results of all statistical significance tests throughout this thesis. A p-value is the probability of observing a value for the test statistic (in this case, t) that is at least as large as the value we observed, assuming the null hypothesis is true (Duncan & Howitt, 2004). By convention, if $p < 0.05$ then we say that the result is statistically significant, and we reject the null hypothesis (i.e. 'Treatment with nocodazole does have a significant effect on nuclear size.') Getting a lower p-value means there is a higher degree of confidence that we have found a true difference between our samples. On the other hand, if $p > 0.05$, we cannot conclude that there is a statistically significant effect (Cumming, Fidler, et al. 2007).

References

Asumda, F.Z. and P.B. Chase (2011). "Age-related changes in rat bone-marrow mesenchymal stem cell plasticity." BMC Cell Biology **12**: 44.

Berger, R.L. and G. Casella (2001). Statistical Inference. Duxbury Press.

Boulant, S., C. Kural et al. (2011). "Actin dynamics counteract membrane tension during clathrin-mediated endocytosis." Nat Cell Biol **13**: 1124-1131.

Conlon, I.J., G.A. Dunn et al. (2001). "Extracellular control of cell size." Nat Cell Biol **3**: 918-921.

Cumming, G., F. Fidler et al. (2007). "Error bars in experimental biology." J Cell Biol **177**(1): 7-11.

Cumming, G. and S. Finch (2005). "Inference by eye: Confidence intervals, and how to read pictures of data." Am Psychol **60**: 170-180.

Dahl, K.N., A. Engler et al. (2005). "Power law rheology of isolated nuclei with deformation mapping of nuclear sub-structures." Biophys J **89**: 2855-2864.

Dodge, Y. (2003). The Oxford Dictionary of Statistical Terms. Oxford University Press.

Duncan, C. and D.L. Howitt (2004). The SAGE Dictionary of Statistics: A Practical Resource for Students in the Social Sciences. Sage Publications Ltd.

Gurland, J. and R.C. Tripathi (1971). "A simple approximation for unbiased estimation of the standard deviation." American Statistician **25**(4): 30-32.

Kretlow, J.D., Y. Jin et al. (2008). "Donor age and cell passage affects differentiation potential of murine bone marrow-derived stem cells." BMC Cell Biology **9**:60.

Thomas, S.G., S.D.J. Calaminus et al. (2007). "Studies on the actin-binding protein HS1 in platelets." BMC Cell Biology **8**: 46.